Experiments in the application of positrons to Medical Physics

David Bruce Stevens

July 2019

A thesis submitted for the degree of Master of Philosophy of The Australian National University

Declaration

This thesis is an account of research undertaken from July 2014 at The Australian National University in The Research School of Physics and Engineering and as well, in part, at The Canberra Hospital Department of Medical Physics and Radiation Engineering, Canberra, Australia. To the best of the author's knowledge and belief, this thesis contains no material which has been accepted for the award of any other degree or diploma at any university. It contains no material previously published or written by another person, except where due reference is given in the text.

David Bruce Stevens

July 2019

Acknowledgements

First and foremost, I would like to express my sincere thanks to Associate Professor James Sullivan, who provided me with the opportunity to pursue my ambition to undertake research in the field of medical physics after a long absence from university life. I would also like to thank him for his ongoing guidance and support throughout this degree which at times required his prowess in co-ordinating activities between the University and The Canberra Hospital.

I would like to thank Dr Joshua Machacek and Emeritus Professor Stephen Buckman for their advice, interest and encouragement over the duration of the research. Also, Professor Tim Senden engaged avidly with several aspects of the research described herein, and his contribution was highly valued.

The advice provided by, and the co-operation with Mr Farshid Salehzahi was vital to the successful conclusion of the aspect of the research conducted at The Canberra Hospital (TCH) and my heartfelt thanks go to him. Also thanks to the staff at the Medical Physics and Radiation Engineering Department at TCH, as well as the hospital administration who were instrumental in allowing access to the CT/PET machine.

Adjunct Professor Bob McEachran provided suitable guidance by way of examination of his thorough notes, and I must acknowledge the hours of enjoyment afforded by his equine partners. Thank you Bob, Dancer (dec), Davey (dec) and Prince (dec). It is my hope that the enjoyment was not simply a one-way street. Dr Dan Murtagh has always been a voice of support and encouragement in the laboratory for me, thank you Dan.

Thanks also go to Professor Ross Stephens of The Biomedical Radiochemistry Laboratory here at RSPE for our numerous interactions and his valued advice with respect to medical imaging and radiochemistry. Professor Vince Craig was generous in allowing the use of various facilities within the Department of Applied Mathematics, including but not limited to, the Contact angle goniometer and the Chemical preparation Laboratory. Vince also provided needed advice regarding colloid chemistry and plasma cleaning of silicon substrates. Many thanks, Vince.

Associate Professor Lan Fu provided essential advice and Dr Ziyuan Li assisted with access to facilities regarding the design and fabrication of micro-structures. The staff at the Australian National Fabrication Facility ACT Node (ANFF), including Dr Fouad Karouta, Dr Mark Lockrey, Dr Naeem Shahid and Dr Kaushal Vora have provided professional advice and training in the use of the various equipment which were necessary for the fabrication and analysis of several materials produced during the course of this research.

My thanks go to Dr Gustavo Garcia of the Spanish National Research Council and Professor Ron White of James Cook University who provided advice and data regarding the modeling of positron scattering. Thanks also go to Dr Jimena Gorfinkiel of The Open University in the United Kingdom for her advice and guidance regarding R-matrix modeling.

I would like to acknowledge the technical support willingly provided by Mr Stephen Battisson, Mr Ross Tranter and Mr Colin Dedman. Penultimately, I wish to thank the cohort of graduate students surrounding me during the research. Jacob, Tamara, Roisin, and Colin each contributed to a valuable learning environment and I hope that they too felt that my contribution has been worthwhile.

Finally, I would like to thank my daughters, Rosanna, Amelia and Arabella, and my wife, Marites, for their continual encouragement, and for being the reason that this research was undertaken by me at all.

Abstract

Three aspects of the use of positrons in relation to medical science are investigated.

In order to gain a better, more complete understanding of the interaction of positrons and electrons with biological systems, a series of scattering experiments has been undertaken at the Australian National University. The current research extends the existing knowledge base by scattering positrons and electrons from thymine, which is a DNA nucleobase, and pyridine, which is a root molecule for a number of biologically relevant molecules. Cross-sections thus obtained contribute further to the development of a model for positron transport within the human body.

Liquid water forms approximately 70 percent of the human body by mass. Being able to make measurements of positron interactions with liquid water also contributes to a more accurate model of positron transport in the human body. Until recently, positron beams were limited to high vacuum environments, however it is now possible to extract positrons into air and hence a liquid water target has become a viable option. The current investigation proposes and demonstrates the possible construction for such a target.

One of the limiting factors which contributes to the relatively low resolution of Positron Emission Tomography (PET) images is the distance from the source isotope that a positron travels prior to annihilating with an electron. The current research investigates the possibility of reducing this distance by using heavy metals surrounding the positron source. Initial experiments relied on a positron producer being sandwiched between layers of platinum. This configuration did not result in a significant change in annihilation distance. Subsequent experiments were conducted using a colloid where the positron producer is bound in a lead compound. Analysis of the images thus obtained appeared to show a small reduction in apparent target size, however the factor which limited the observable improvement was the PET machine camera resolution. Further research is warranted, however possibly using a small animal PET scanner.

Contents

List of Figures

Chapter 1

Introduction

Over the past several decades, significant advances in the use of anti-matter (positrons, the anti-matter particle corresponding to an electron) in health science have been made. However, knowledge surrounding any detrimental effects of the application of antimatter in this field remains incomplete. The purpose of the research described herein is to break new ground and unearth new knowledge regarding the way in which positrons, at various energies, interact with human biology. Thereby informing modeling techniques for such interactions.

More recently, there has been an increasing reliance upon medical imaging systems to provide detailed information regarding the size, location and changes in anatomical abnormalities such as tumors. Accurate, high resolution images are vital in allowing physicians to make informed decisions concerning the determination of the most appropriate method of treatment of life threatening cell malignancies, and to be able to assess changes in them, no matter how minor.

Whilst X-rays were the original medical imaging technique, first used in the late 1800's, other techniques such as ultrasound, CT/CAT (Computed Tomography / Computer Assisted Tomography), MRI (Magnetic Resonance Imaging), SPECT (Single-Photon Emission Computed Tomography) and PET (Positron Emission Tomography) have evolved during the mid-to-late 20th century and beyond.

The advantages of imaging internal structures appear to have largely outweighed the disadvantages even though, historically speaking, the disadvantages have not been thoroughly understood. There are cases throughout history where the use of medical imaging has caused a substantial degradation in personal health and even induced cancer, as reported by de Gonzalez et al. [3]. A result of which has been the development of national and international ionising radiation dosage guidelines.

For example see https://www.epa.gov/radiation/radiation-health-effects or scan the adjacent QRcode. Post implementation of these guidelines, improvements in patient prognosis and the associated improvement in life expectancy and quality of life have been attributed to the successful use of medical imaging systems. This is particularly evident with respect to screening for lung cancer and breast cancer, as seen in papers by Pyenson [4] and Marmot et al. [5] respectively. It should be noted that any harm from such screening, attributable to mis-diagnosis, is outside the scope of the work presented in that research. For much of the 20th century, little was understood about the fundamental mechanisms by which ionising radiation causes damage to living cells. It had been observed that damage to DNA (DeoxyriboNucleic Acid) is the microscopic mechanism by which ionising radiation could be used to treat cancer, however such damage was not restricted to the DNA of cancer cells, but also affected normal living cells in the vicinity of the cancer in the same manner, as reported by Brenner et al. [6].

USA EPA

Studies by Boudaıffa et al. [7] during the first decade of the 21st century have revealed that medical imaging can induce more damage to DNA than previously expected. This damage has been found to be caused not so much by the primary radiation used, but rather by the scattered secondary electrons which are released as a result of ionisation, and are of a significantly lower energy than the primary radiation. It is important to understand the mechanisms by which the primary radiation produces these secondary electrons, as well as the mechanism by which the secondary electrons cause damage to the DNA. These studies addressed the capacity of primary radiation, other than positrons, to result in secondary electrons and the subsequent damage these electrons caused, through dissociative electron attachment. On the other hand, positrons are the primary radiation source in the case of PET imaging and positherapy [8]. High energy positrons also result in the release of low energy secondary electrons, and low energy positrons themselves may also cause DNA damage during thermalisation in a manner similar to low energy electrons. Damage to DNA may also result from the gamma-ray radiation produced during their ultimate annihilation with electrons.

In view of the preceding introduction, the current research focuses on two aspects which contribute to a better understanding of the interaction between human tissue and positrons as well as one possible technique which may provide a pathway to obtaining

more exact information from PET scans.

Firstly, a question arises as to the manner in which positrons scatter from the constituents of DNA. In order to expand the body of knowledge concerning the positron scattering cross-sections of human biological molecules in a laboratory situation, thymine and pyridine were separately used as the target molecules. Investigation of these biomolecules forms part of a series of investigations undertaken by the laboratory at ANU. Other biomolecules which had been measured previosly included uracil, pyrimidine, water (vapour phase) and THF (tetrahydrofuran) [9–12]. The benefits of being able to determine the manner in which positrons scatter from the constituents of DNA are relatively obvious, as it is ultimately necessary to know the positron scattering cross-sections of biomolecules in order to model positron scattering in-vivo which will help to inform radiologists when determining correct patient dosimetry.

Next, a question has arisen as to the manner in which positrons interact with liquid phase water. Liquid phase water is the largest constituent (by mass) of the human body. It plays a significant role in the structure, and therefore function of DNA. Radiation damage to DNA during medical imaging and radiation therapy is partially dependent upon the scattering of ionizing radiation by water in the vicinity of DNA chains. Although measurement of the positron scattering cross-sections of vapourised water has been made via positron scattering, it has been difficult to design and develop an apparatus to measure the interaction between positrons and liquid phase water due primarily to the incompatibility of liquid water with the vacuum technology required to sustain a positron beam. Recent developments by Oshima et al. [13] in Japan have allowed a horizontal, moderate energy, positron beam to be extracted into air for a short distance. The present investigation aims to address the challenge of developing a mechanism for holding a liquid water target for use with the Japanese apparatus such that current models of positron transport in liquid water may be tested.

The final assignment is an investigation into the possibility of improving the resolution of PET images by incorporating highly electron dense atoms into a PET contrast medium, thereby reducing the positron path length to annihilation. The annihilation of positrons with electrons at a region of interest (ROI) is the fundamental physical mechanism behind PET being able to produce a meaningful image of biologically active sites within the human

body. Uncertainty in the image thus produced is in part attributable to the distance the positron travels prior to annihilation. By decreasing the positron mean free path prior to annihilation, improvements in image resolution may be achieved. The current study investigates the effect on the resolution of a PET image by co-locating heavy metal atoms and a positron source.

These are the challenges that the current research attempts to either address directly, or to at least facilitate future research into. Taken together, they have the potential to expand the knowledge in this fascinating and critical field.

This thesis is comprised of five chapters, including this introduction as the first.

Chapter 2 reports the theory, experimental activities and results related to positron and electron scattering from thymine and pyridine.

Chapter 3 begins with the theory of positron transport in liquid water and then focuses on the design, practical fabrication and demonstration of a liquid water carrier for use in future positron measurements.

Chapter 4 reports the activities undertaken in pursuit of the validation of a reduction in pre-annihilation positron path length, and resultant improvements in PET image resolution.

Chapter 5 draws the three aspects of the current research together and sets possible directions for future activities in each aspect of the research.

Chapter 2

Positron and electron scattering from Biomolecules

2.1 Introduction

The fundamental physical processes which take place during a PET scan, at the atomic and molecular level, can be better understood by gathering experimental data in a laboratory environment and comparing it with existing and developing models.

2.2 Experimental Setup

While this section focuses primarily on the physical setup, some reference will be made to the mechanisms of certain processes along the apparatus.

The apparatus used during the current investigation is the Atomic and Molecular positron beam-line at the Australian National University. While this apparatus has been described elsewhere in detail by Sullivan et al. [14], this work will include sufficient detail, together with additional details of any specific modifications which were required for undertaking the cross-section measurements carried out during the current research. Figure 2.1 shows a schematic of the apparatus.

As indicated in figure 2.1, the entire apparatus is held under vacuum using a system of roughing pumps and turbo-molecular pumps to a vacuum level of approximately 10^{-7} Torr. Potentials on active elements throughout the beamline are controlled via Labview routines. Data acquisition is also achieved using Labview software. Labview is a commercially available suite of software tools and hardware devices.

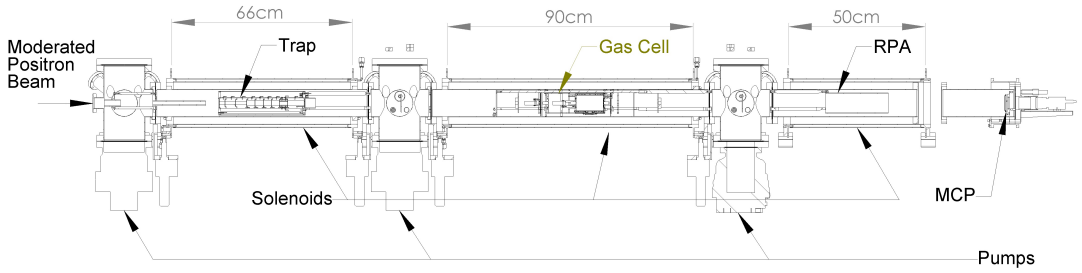

Figure 2.1: Atomic and Molecular Positron Beamline schematic. Moderated positrons enter from the source to the left, are accumulated in the trap section, from where they are ejected towards the target chamber (gas cell) where scattering takes place, then to the analysis stage (RPA - see text) and on to the MCP detector. Solenoidal coils surround each section of the apparatus with molecular turbo pumps providing the high vacuum.

2.2.1 Source stage

The beam-line source of positrons is ^{22}Na with an originally installed activity of approximately 2 GBq, however the activity during the present measurements was approximately 900 MBq due to the age of the source and its half-life of approximately 2.6 years. The emitted positrons have a spread of energies, ranging from zero to around 540 keV which are then moderated using solid neon within the source stage, as shown schematically in Figure 2.2. When electrons are required as the projectile, it is the secondary electrons produced during the positron moderation process that are extracted by the establishment of a negative voltage on the source relative to the remainder of the apparatus. References to magnetic confinement and to movement along the beamline by the projectiles is equally valid for electrons as positrons in the following explanations.

Moderation involves the thermalisation of the portion of positrons emitted from a source that have not been lost to the formation of positronium[1]. Historically, a thin film of crystalline tungsten has been used as the moderating material, since tungsten exhibits a negative work function for positrons. More recently, techniques to improve the growth of solid neon moderators has meant an increased efficiency in useable positron production from around 10^{-3} to 10^{-2} at the expense of the energy resolution of the moderated beam [15]. The typical effect of positron moderation can be seen in figure 2.3

[1]Positronium is the short-lived exotic atom formed by a positron binding with an electron.

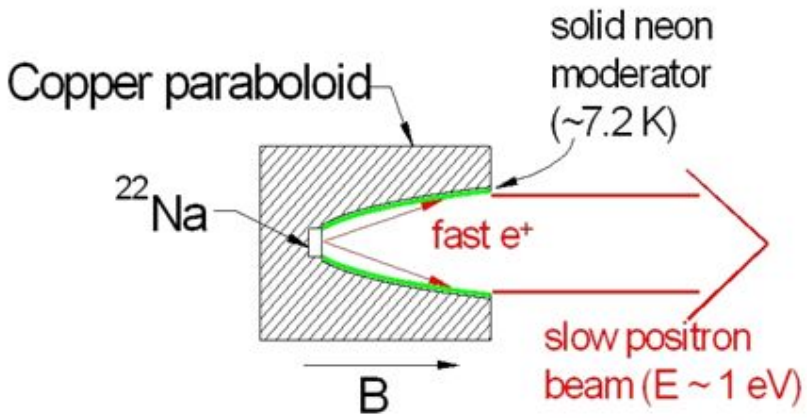

Figure 2.2: The source stage showing the positioning of the ^{22}Na source and solid neon moderator.

which is taken from Schultz and Lynn [16]. The moderated beam produced here has an energy resolution of around 1.5 eV with about 3 million positrons per second.

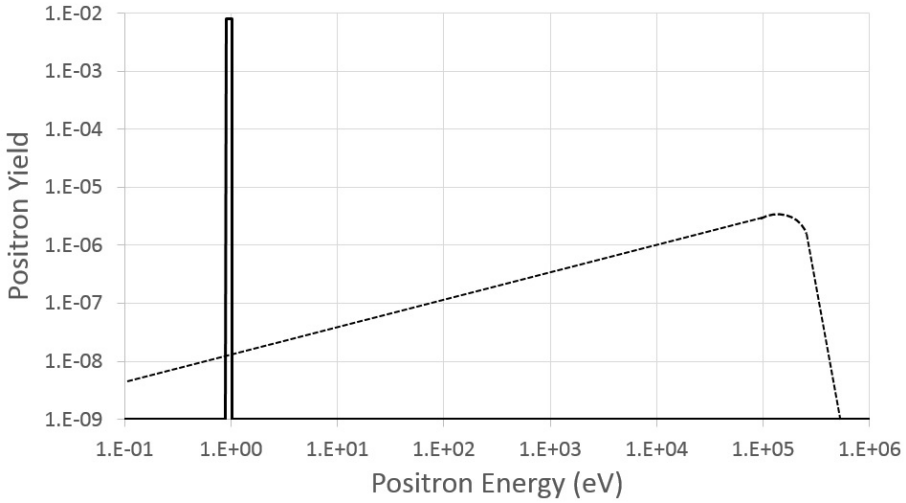

Figure 2.3: Comparison of the energy spectra of positrons emitted from a source (dashed line) and moderated positrons (solid line).

Within the source stage, the positrons are magnetically confined using a set of Helmholtz coils and are then accelerated towards the trap stage by an electrostatic potential applied to the moderator of typically 30 V. The positrons are magnetically confined to the centre of the vacuum system by a set of solenoidal coils surrounding the vacuum system. The magnetic fields at the various stages of the apparatus are typically 500 gauss at the trap stage, the target stage and analyser stage, although for inelastic cross-section measurements, the field at the analyser stage is set to around 20 gauss. The solenoidal magnetic

field strength at the detector is approximately 150 gauss.

2.2.2 Trap stage

The trap stage is supplied with trap gasses (N_2 and CF_4) to initially trap the electrons/positrons through inelastic collisions via electronic excitation and subsequently cools them by exciting vibrational and rotational modes in the trap gases. Hence the cooled electrons/positrons are confined to a potential well in a thermalised state in order to accumulate sufficient positrons to ultimately produce a electron/positron pulse. This pulse is achieved by raising the potential well to above the target-facing end potential of the trap, but below the source-facing end of the trap as shown in 2.4. This design is based upon work carried out by Murphy and Surko [17] and refined by Gilbert et al. [18] and Sullivan et al. [14].

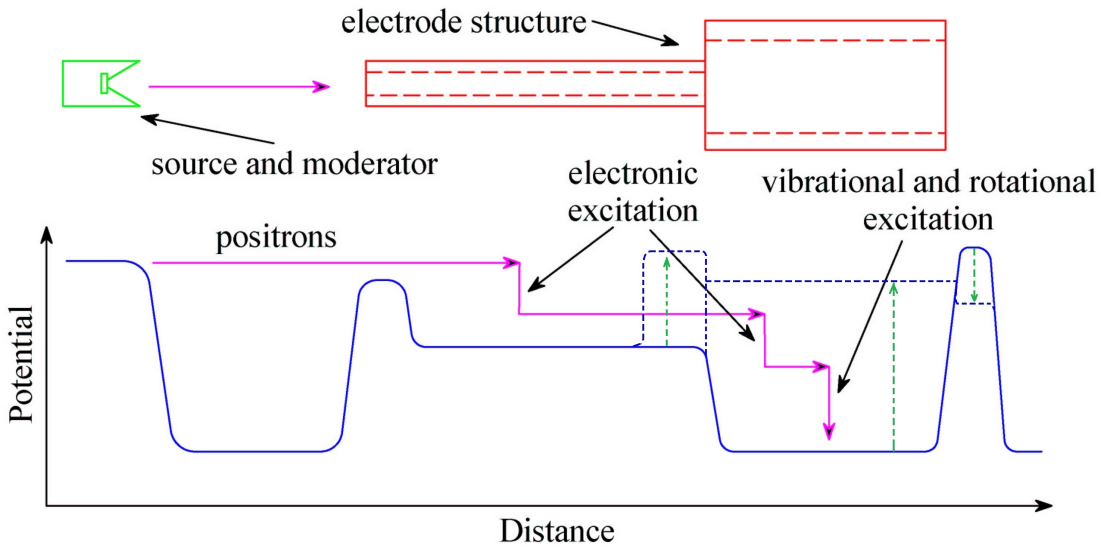

Figure 2.4: Trap potential configuration. Dashed green arrows indicate the pulse release condition.

The electron/positron pulse travels towards the target stage at an energy determined by the potential of the final electrode in the trap. The potential difference between the target stage and the final stage of the trap therefore determines the electron/positron energy, or scattering energy inside the target cell. Electrons/positrons are then scattered by the target gas molecules within the target cell. The target cells used for thymine and

pyridine are discussed now.

2.2.3 Target stage

For liquid targets, a gas cell is installed in the target stage whereas for solid targets an oven is installed into the target stage.

Gas cell

The target stage for pyridine consists of a gas cell into which the pyridine vapour is delivered via teflon tubing from a pyridine reservoir. The feed from the reservoir is controlled by a needle valve, with the pressure being monitored throughout the measurements using an MKS Instruments Inc. Model 690A Absolute Baratron pressure transducer accurate to a few parts in 10^{-6} Torr, which allowed the determination of the pyridine number density. Figure 2.5 below shows the gas cell installed prior to closing the beamline. Three freeze-pump-thaw cycles were performed on the pyridine reservoir to ensure that any contaminants in the pyridine were removed.

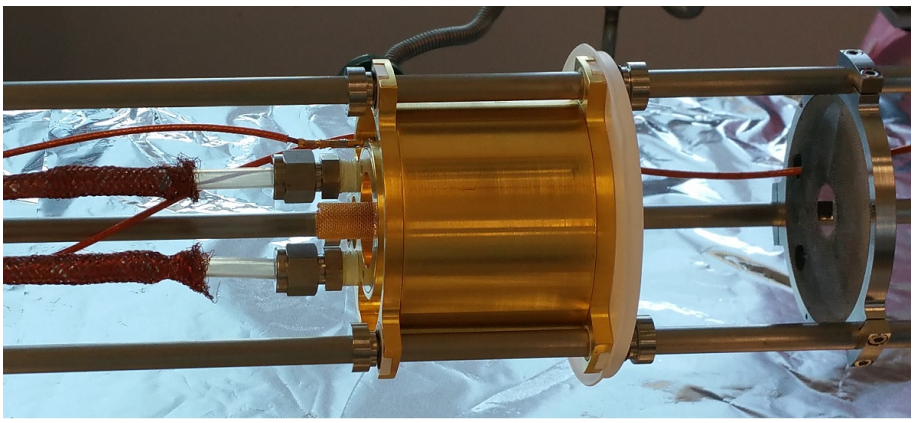

Figure 2.5: Gas cell prior to closing up.

The gas cell is constructed of gold plated copper with an internal length of 50 mm ±0.3 mm with axially located apertures of 5 mm diameter to allow entry and exit of the electron/positron beam. Immediately preceding the target stage there is a retarding potential analyser (RPA1) consisting of an open ended mesh cylinder, the purpose of which is to remove projectiles with a reduced energy caused by scattering from trap gases at the exit of the trap.

Oven

The target stage for thymine incorporates an oven so that sublimation of thymine from solid phase to vapour phase can be achieved. The oven is a copper cylindrical chamber of internal diameter 60 mm and internal length 100 mm ±0.3 mm with entry and exit apertures of approximately 5 mm diameter, axially located, with a copper mesh "neck" of 10 mm dia. at each entry and exit aperture in order to minimise electrostatic fringe field effects. At the base of the oven chamber is a detachable crucible into which a solid sample of target material (thymine in this case) can be loaded prior to closing and pumping down the beamline. Figure 2.6 shows the oven assembly in cross-section.

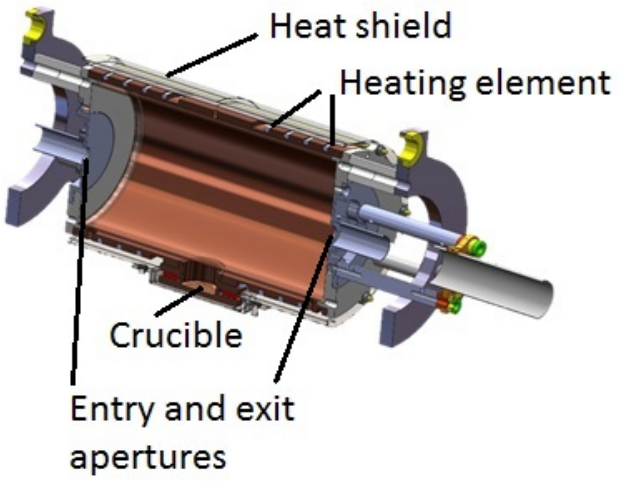

Figure 2.6: Oven cross-section schematic showing heating elements, heat shield and positioning of the sample crucible.

A heater element is wound around the body of the oven and then the oven is surrounded by a non-magnetic heat-shield for greater efficiency. The crucible also has a heater element built into it to allow the sample to be heated independently of the oven itself. To avoid multiple scattering events, the number density of the target molecule should be such as to allow a maximum of 10% of the positrons or electrons in the beam to be scattered. The temperature of the oven is controlled by setting the current in the heating elements.

Adequate control of the thymine number density required a maximum uncertainty in the temperature measurement of ±2° C. Several strategies for measuring the temperature inside the oven were considered including thermocouples, thermistors and platinum resistive thermal devices (PRTDs). It was determined that PRTDs provided the temperature

range necessary and would not contaminate the vacuum in the beamline, nor interfere with the magnetic confinement strategies internal to the beamline.

Since vaporised thymine condenses on any cold surface within the vacuum chamber, it is necessary to include cold bars adjacent to each end of the oven so that the thymine vapour is restricted from passing into the trap stage or the detector stage. An insulating layer of thymine on either of those surfaces would adversely affect the trapping of positrons and electrons, and their detection, respectively. The cold bars were maintained at temperatures of approximately 263 K using Peltier cells and monitored using PRTDs during the experiment. Two 10 W halogen bulbs were installed in the chamber to aid in baking the chamber to remove any contaminants that may have been adsorbed prior to closing it and pumping down. Figure 2.7 shows the internal configuration of the target chamber prior to closing up and baking out. One of the cold bars can be seen in this figure.

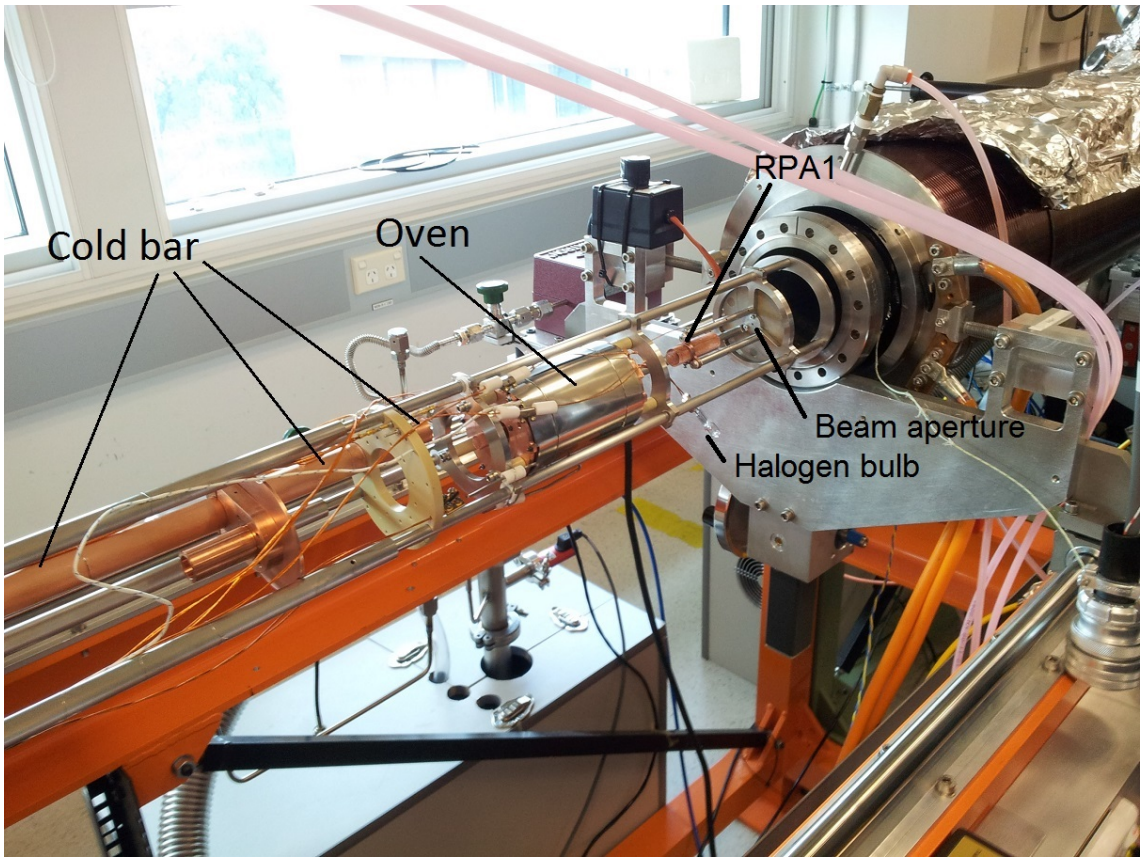

Figure 2.7: Target chamber with oven installed. One cold bar can be seen as well as the pre-oven retarding potential analyser (RPA1) and one of the halogen bulbs used to assist in baking.

2.2.4 Analysis stage

The analysis of the positron energy after passing through the target cell is performed by a retarding potential analyser (RPA) (see figure 2.8) which lies between the target stage and the detector stage as indicated in figure 2.1, and consists of an open-ended cylindrical, gold plated element of diameter 70 mm and length 300 mm. Applying controlled potentials to this element while detecting the intensity of the transmitted beam allows the determination of the spread in energy induced in passing through the target cell. It is the measurement of this parallel component of energy that is necessary in the determination of the target cross-section. The analysis stage is confined within a solenoidal magnetic field, the strength of which can be controlled independently so as to allow separation of the elastic and inelastic cross-section as will be discussed later in section 2.3.4.

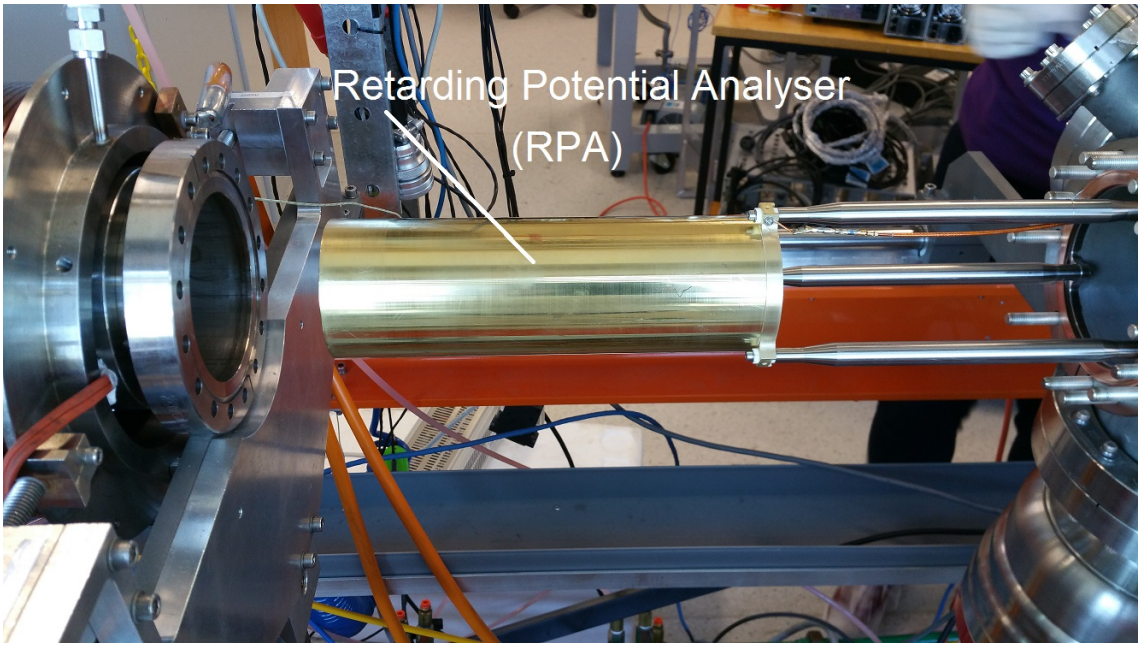

Figure 2.8: Retarding potential analyser mounted prior to closing.

2.2.5 Detector stage

The detector stage, also with a confining magnetic field, is comprised of a micro-channel plate (MCP) (see figure 2.9), used to detect the positrons or electrons which have been able to traverse the entire apparatus. The operating principle of the MCP is that an energetic particle impinging on the front plate of the MCP will generate a cascade of electrons, amplified through multiple ionising collisions down the length of the channels

and accelerated by a fixed potential difference onto a back-plate and thus result in a current at the MCP output which is proportional to the number of impinging particles. This current signal from the MCP is then converted to a voltage via a trans-impedance amplifier and recorded by the computer as a function of retarding voltage.

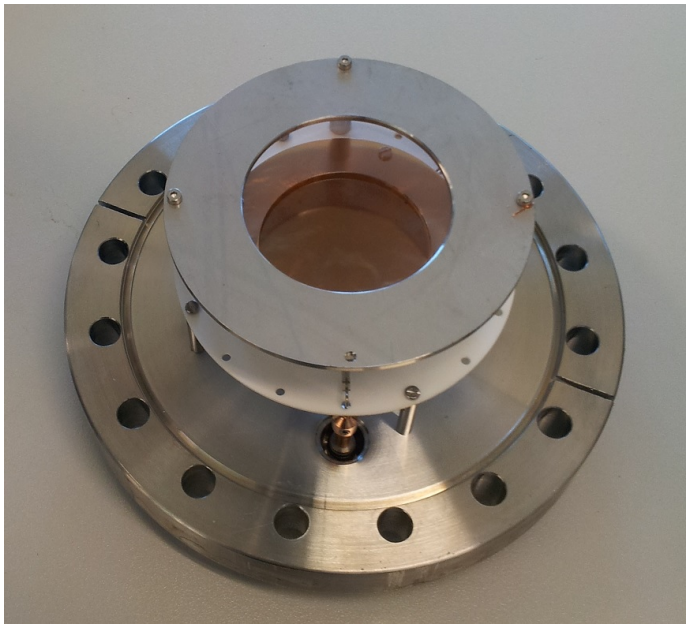

Figure 2.9: Micro-channel plate mounted on the beamline endplate.

2.3 Scattering Theory

The term "cross-section" is used to characterise the interaction between two particles. The notion of taking a bio-molecule and slicing through it in order to measure its cross-sectional area is both impractical and also misleading. It is, however valid to consider a molecular (or indeed atomic) cross-section by measuring the effective collision interaction area when a projectile particle scatters from the molecule (or atom). The projectile particles used during the current research are separately positrons and electrons.

The interaction between two species of particle where one, more massive species, can be considered to be the target and the other, less massive species, can be considered as the projectile (in the laboratory reference frame), can be described from first principles in the classical regime, however the systems investigated in this chapter require a quantum mechanical treatment. Since the experiments described here use positrons or electrons as the projectile (i.e. moving particles) and biomolecules as the target (i.e. stationary

particles), the laboratory frame and centre of mass frame are identical within the limits of measurement due to the substantial difference in mass of the two particles.

There are a number of possible interactions that can take place between electrons or positrons and molecules during the scattering process. These can be referred to as scattering channels. They include:

A. Elastic scattering, where there is no transfer of energy to the target states and the projectile particle simply deflects from the molecule and is thus scattered through various angles, with no energy being given up to exciting internal modes of the molecule. Such an interaction can be described algebraically as follows:

$$e^{+/-} + AB \quad \rightarrow \quad e^{+/-} + AB$$

B. Inelastic scattering, where some kinetic energy is lost by the electron/positron and transferred to the molecule (in a form other than kinetic energy), with a number of possible outcomes as follows:

$e^{+/-} + AB \quad \rightarrow \quad e^{+/-} + AB^*$ (molecular excitation)

$e^{+/-} + AB \quad \rightarrow \quad e^{+/-} + A + B$ (molecular dissociation)

$e^{+/-} + AB \quad \rightarrow \quad e^{+/-} + A + B^*$ (molecular dissociation with excitation)

$e^{-} + AB \quad \rightarrow \quad 2e^{-} + AB^{+}$ (molecular ionisation)

$e^{-} + AB \quad \rightarrow \quad 2e^{-} + A + B^{+}$ (molecular dissociation with ionisation)

$e^{+} + AB \quad \rightarrow \quad AB^{+} + 2\gamma$ (molecular ionisation by direct annihilation)

$e^{+} + AB \quad \rightarrow \quad AB^{+} + e^{-} + e^{+}$ (molecular ionisation by electron stripping)

$e^{+} + AB \quad \rightarrow \quad AB^{+} + Ps$ (molecular ionisation by positronium formation)

Note that "molecular excitation" includes vibrational and rotational excitation, however the available beam energy resolution of our apparatus is insufficient to be able to resolve these processes. It must be remembered, however that these do contribute to the total cross-section.

2.3.1 Cross-section sub-types

The theory presented in this section invokes a spherically symmetric scheme initially, and subsequently describes the modifications necessary to adapt to the cylindrical symmetry used in the experiment, incorporating uniform magnetic confinement of the scattered particles. References to "parallel" and "perpendicular" are with respect to the magnetic field, which is co-linear with the cylindrical axis of symmetry. Also, there is an underlying assumption that any scattered projectile undergoes only one scattering event. This is achieved by limiting the vapour pressure and hence number density such that only 10% of the incident beam scatters within the target cell.

2.3.2 Differential cross-section (DCS)

Consider the spherically symmetric experimental configuration shown in figure 2.10. Here a mono-energetic beam of incident electrons/positrons is directed with an energy E towards a target molecule with some incident particles being scattered through an angle, θ, which allows them to reach the detector.

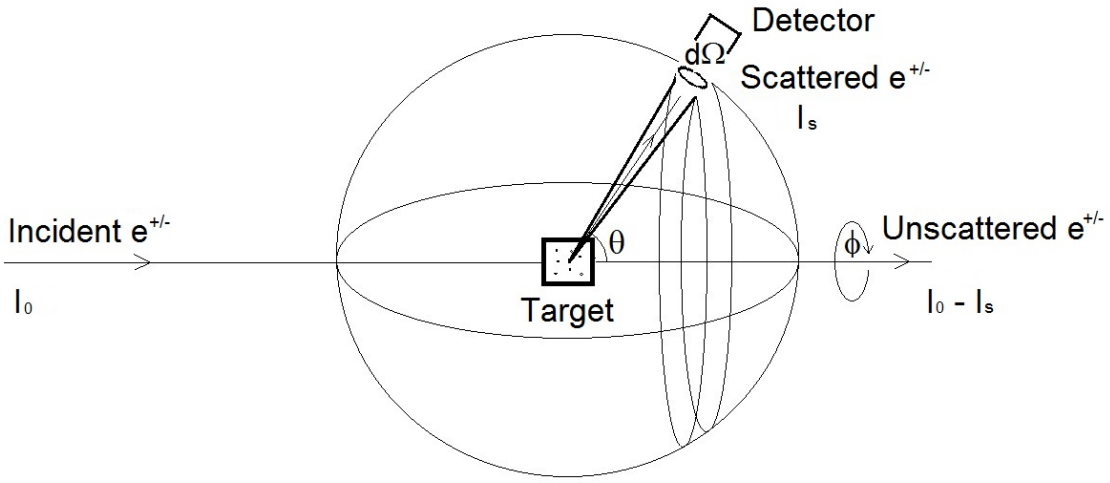

Figure 2.10: Electron/positron scattering from a target. I_0 is the incident beam intensity and I_s is the scattered beam intensity.

The differential cross-section is an angular discrimination of the electron/positron molecular cross-section for a particular energy, E, of incident projectile. It is measured as the probability that a electron/positron will scatter into a particular solid angle, $d\Omega$. Thus it is represented as area per steradian as a function of scattering angle, θ. From

figure 2.10 this can be seen to be given by equation 2.1:

$$\frac{d\sigma}{d\Omega}(E,\theta) = \frac{1}{nl}\frac{I_s}{I_0} \tag{2.1}$$

where $d\sigma/d\Omega$ is the differential cross-section as a function of both energy and scatter angle, n is the target number density, l is the length of the target, I_0 is the incident projectile intensity and I_s is the scattered intensity.

As seen in section 2.2, a cylindrically symmetric scattering apparatus is used in the current research, largely due to the positron beam production requiring a uniform axial magnetic field. The remainder of the description of the differential cross-section will relate to the cylindrical configuration.

To extract information regarding the scattering angle and intensity from a magnetically confined system, it is necessary to consider geometry. Scattered positrons or electrons will transfer some of their energy from the forward direction to the direction perpendicular to the magnetic field. The fraction of energy which is transferred can be determined through the use of trigonometry and energy analysis. Figure 2.11 shows the scattering of a electron/positron from a target within a uniform magnetic field.

The small radius cyclotron motion of the projectile prior to a collision is a result of the residual thermal energy that the projectiles have after the trapping process. This is expected to result in a cyclotron radius of around 5 μm as described by Gilbert et al. [18] and although it contributes marginally to the overall systematic error, will be neglected in this analysis.

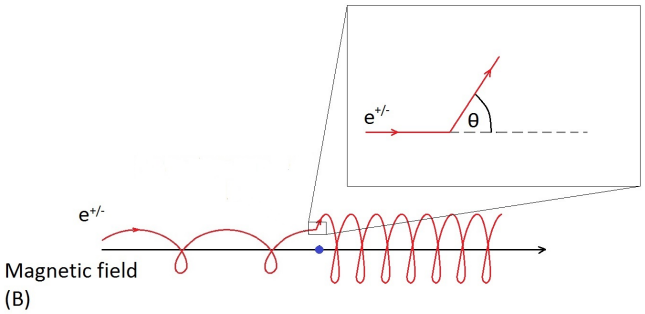

Figure 2.11: Electron/positron scattering from a target.

Kinetic energy components in the axial and perpendicular directions can be determined by examining the particle velocity components parallel and perpendicular to the incident

beam respectively. Figure 2.12 is drawn in velocity space.

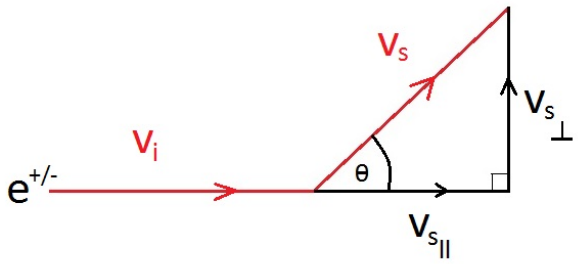

Figure 2.12: Velocity space scattering from a target.

Once scattered, assuming elastic scattering where a negligible amount of energy is transferred to the target, the projectile will instantly travel at an angle θ from the target, with a velocity v_s equal in magnitude to v_i. The scattered velocity vector, v_s can be resolved into components parallel to ($v_{s\parallel}$) and perpendicular to ($v_{s\perp}$) the initial velocity (v_i). The relationship between θ, v_i, and $v_{s\parallel}$ is given by equation 2.2.

$$cos\theta = \frac{v_{s_\parallel}}{v_i} \tag{2.2}$$

Now, due to the presence of the uniform magnetic field, kinetic energy can be associated with each velocity component. For example,

$$E_\parallel = \frac{1}{2} m v_{s_\parallel}^2 \tag{2.3}$$

Therefore, by measuring the parallel energy, based on the parallel velocity component, we can determine the angle θ by which projectiles have been scattered.

$$\theta = cos^{-1}\left(\sqrt{\frac{E_\parallel}{E}}\right) \tag{2.4}$$

Where the subscripts to indicate incident (i) and scattered (s) have been dropped. So, by measuring the energy of the scattered projectile parallel to the magnetic field, and by knowing the initial energy of the projectile prior to scattering, it is possible to determine the angle through which the projectile has been scattered by the target and this is necessary to determine the differential cross-section of the target.

Now, apart from determining the angle through which a projectile is deflected, we also need to know the probability of such a deflection. If we start with a beam of projectiles of known intensity and energy, and measure the number of projectiles scattered through each angle, then by normalising the scattered projectile intensity to the incident projectile intensity, we can determine the scattering probability at each angle. Since we are unable to isolate a particular scattering angle, but rather only select a maximum scattering angle through the setting of the retarding potential analyser (RPA, see Figure 2.1 and subsequent description), the differential cross-section can be represented by equation 2.5 as derived in Sullivan et al. [19].

$$\frac{d\sigma}{d\Omega} = C\left(\frac{dE_{\parallel}}{d\Omega}\right)\left(\frac{dI(E_{\parallel})}{dE_{\parallel}}\right) \tag{2.5}$$

where C is the constant of proportionality relating the scattering cross-section to the scattering probability, $dE_{\parallel}/d\Omega$ is the derivative of the parallel energy component with respect to the effective solid angle sampled and finally, $dI(E_{\parallel})/dE_{\parallel}$ is the probability that a projectile will be scattered with a resultant energy in the range $dE_{\parallel}$.

C is given by equation 2.6

$$C = \frac{1}{nl} \tag{2.6}$$

Now,

$dE_{\parallel}/d\Omega$ in equation 2.5 can be derived as follows:

Since, from equation 2.4

$$E_{\parallel} = E\cos^2\theta \tag{2.7}$$

then

$$\frac{dE_{\parallel}}{d\theta} = -E\sin 2\theta \tag{2.8}$$

and

$$\frac{dE_{\parallel}}{d\Omega} = \left(\frac{dE_{\parallel}}{d\theta}\right)\left(\frac{d\theta}{d\Omega}\right) \tag{2.9}$$

From geometry,

$$\frac{d\theta}{d\Omega} = \frac{1}{2\pi \sin\theta} \tag{2.10}$$

By combining equations 2.7, 2.8, 2.9 and 2.10,

$$\begin{aligned}
\frac{dE_{\parallel}}{d\Omega} &= -\frac{E \sin 2\theta}{2\pi \sin\theta} \\
&= -\frac{1}{\pi}\frac{E \sin 2\theta}{2 \sin\theta} \\
&= -\frac{1}{\pi}\sqrt{\left(\frac{E^2 4 \sin^2\theta \cos^2\theta}{4 \sin^2\theta}\right)} \\
&= -\frac{1}{\pi}\sqrt{\left(E^2 \cos^2\theta\right)} \\
&= -\frac{1}{\pi}\sqrt{EE_{\parallel}}
\end{aligned} \tag{2.11}$$

By substituting equation 2.11 into equation 2.5 we arrive at the relationship between the DCS and the measured intensity $I(E_{\parallel})$ for the case of elastic scattering.

$$\frac{d\sigma}{d\Omega} = -\frac{C}{\pi}\sqrt{EE_{\parallel}}\left(\frac{dI(E_{\parallel})}{dE_{\parallel}}\right) \tag{2.12}$$

Of course $-C/\pi$ is still a constant term and can be replaced with C_{π} so that equation 2.12 finally becomes

$$\frac{d\sigma}{d\Omega} = C_{\pi}\sqrt{EE_{\parallel}}\left(\frac{dI(E_{\parallel})}{dE_{\parallel}}\right) \tag{2.13}$$

Therefore, as long as we can determine the projectile kinetic energy prior to scattering, E, the projectile kinetic energy along the axis of the apparatus post scattering, $E_{\parallel}$, and can determine the intensity change with change in $E_{\parallel}$, equation 2.13 allows us to determine the DCS.

2.3.3 Grand Total cross-section (GTCS)

The Grand Total cross-section is effectively a measurement of the probability of any scattering event occurring at all at a given energy. Typically, the projectile energy can most easily be controlled through a simple conversion of electrical potential energy to particle kinetic energy. Only elastic interactions between the projectile and target are possible up until the threshold energy for inelastic events is reached. Apart from rotational and vibrational excitation of the target molecule, (which is indistinguishable from elastic scattering in the current experiments) the first significant inelastic interaction for an incident beam of positrons is positronium formation. For a beam of incident electrons, it will be electronic excitation followed by the first ionisation energy of the molecule.

The GTCS can be obtained by integrating the elastic differential cross-section (equation 2.1) over the entire sphere, a solid angle of 4π steradians, shown in figure 2.10,

$$\int_0^{4\pi} \frac{d\sigma}{d\Omega} d\Omega = \int_0^{4\pi} \frac{1}{nl} \frac{I_s}{I_0} d\Omega \tag{2.14}$$

giving equation 2.15.

$$\sigma = \frac{1}{nl} \int \frac{I_s}{I_0} d\Omega \tag{2.15}$$

Equation 2.16 is derived from the Beer-Lambert Law and provides a method for measuring the GTCS based upon experimentally measurable data. It makes the assumption that scattered projectiles are removed from the beam, which may not always be true, particularly where forward directed elastic scattering is a feature, such as for polar molecules. This would manifest as a reduced cross-section at low scattering energies.

$$\sigma = \frac{-1}{nl} . ln\Big(\frac{I_u}{I_0}\Big) \tag{2.16}$$

where n is the number density of the target in m^{-3}, l is the distance over which scattering can occur in *metres*, I_u is the intensity of unscattered projectiles and I_0 is the incoming projectile intensity.

2.3.4 Total inelastic cross-section (TICS)

During an inelastic scattering process, some of the projectile's energy is lost to the target hence either exciting the target vibrationally, rotationally, electronically or through ionisation or dissociation. In this case, the parallel energy of the projectile will similarly be reduced, although not entirely through migration to the perpendicular energy. Therefore the question arises as to how to distinguish between electrons/positrons that have scattered elastically and those which have scattered inelastically, by only being able to measure the parallel energy. The answer lies in the adiabatic invariant, $E_\perp/B$ for a charged particle in a slowly varying magnetic field of strength B. Hence, by using a higher field strength B_s in the scattering region, where there is a transfer to $E_\perp$ through angular scattering, and a lower field strength B_a in the analysis region, $E_\perp$ will decrease proportionately with B_s/B_a, whereas the total energy will be maintained, meaning that $E_\perp$ is transferred back to $E_\parallel$. Total energy loss is then measurable by the RPA, as described by Gilbert et al. [18] and the TICS can be measured.

2.3.5 Positronium (Ps) formation cross-section

As mentioned in section 2.2.1, positronium (Ps) is a bound state of an electron - positron pair. When using positrons as the projectile, positronium formation is always an open scattering channel. Both electrons and positrons are characterised by a spin quantum number of either $+\frac{1}{2}$ or $-\frac{1}{2}$, leading to the possibility of two forms of positronium. One with anti-parallel spins, called para-positronium (p-Ps), and the other type with parallel spins, called ortho-positronium (o-Ps). Both forms of positronium in the ground state annihilate with a mean lifetime of 0.125 ns for p-Ps, typically producing two gamma-ray photons in diametrically opposed directions, and a mean lifetime of 142 ns for o-Ps, typically producing three gamma-ray photons. Owing to the necessity to conserve energy and momentum throughout the annihilation process, the sum of the gamma-ray photon energies must be equal to the sum of the mass equivalent energies of the positron and electron plus any pre-existing Ps kinetic energy.

Positronium formation is only possible if an electron is available for binding to a positron. This requires the molecule to be ionised. The only energy available for the ionisation process is the energy of an incident positron. As a positron ionises the molecule

and binds with an electron, the positronium binding energy is recovered. The binding energy of positronium is described by 2.17.

$$E_n = \frac{6.8eV}{n^2} \tag{2.17}$$

Where n is the primary quantum number of the bound state. The energy required for this scattering channel to be available assumes the ground state of positronium and therefore the positronium formation threshold equals the first molecular ionisation energy minus the ground state positronium binding energy of 6.84 eV. Positronium formation is a destructive process as far as the positron beam is concerned, since it removes positrons from the incident positron beam. By measuring the loss in beam intensity at scattering energies above the positronium formation threshold, it is possible to determine the positronium formation cross-section. Soon after formation, the positronium will annihilate as explained above.

2.3.6 Models of atomic and molecular cross-sections

There are currently several models in use for molecules which can be used to predict scattering behaviour of positrons and electrons. Some of these models which will be used in the comparison to experimental data, will now be discussed.

2.3.7 Independent Atom Model (IAM)

The Independent Atom Model (IAM) is a molecular modeling technique which considers that the cross-section for a complex molecule is compiled from a combination of the cross-sections for each atom comprising the molecule in their relative positions, and integrating over all possible molecular orientations. This modeling method has been found to be accurate at projectile energies greater than about 100 eV. Below this energy, there is considerable deviation from experimental evidence [20]. The deviations from experiment at moderate to low energies can at least in part, be attributed to multiple scattering between atoms within the molecule. The IAM approximation can be expressed as:

$$\sigma^{total}_{molecule} = \sum_{atoms} \sigma^{total}_{atom\,i} \tag{2.18}$$

2.3.8 The Independent Atom Model with a Screening Corrected Additivity Rule (IAM SCAR)

This model builds upon the IAM. For energies in the range from 10 eV - 100 eV, atomic cross-sections are a similar order of magnitude to inter-atomic distances. This results in the IAM failing, since the atoms can no longer be considered as independent centres for scattering purposes. In this energy range multiple scattering within the molecule cannot be neglected. IAM SCAR introduces a rule which attempts to correct for the contributions caused by scattering between atoms within the molecule and the revised approximation can be simplified and expressed as

$$\sigma_{molecule}^{total} = \sum_{atoms} s_i \sigma_{atom\,i}^{total} \tag{2.19}$$

Where s_i, the screening coefficients, reduce the contribution of each atom to the total molecular cross-section and are in the range $0 \leq s_i \leq 1$

2.3.9 IAM SCAR + I

Despite the improvement in agreement with experiment down to 10 eV, IAM SCAR remains in disagreement with experiment below about 10 eV. A further improvement at lower energies is achieved by including an interference contribution factor $\sigma^{interference}$ as shown in equation 2.20

$$\sigma_{molecule}^{total} = \sum_{atoms} s_i \sigma_{atom\,i}^{total} + \sigma^{interference} \tag{2.20}$$

where s_i is the screening coefficient for atom i

It can be shown that $\sigma^{interference}$ is given by

$$\sigma^{interference} = \int \left(\sum_{i \neq j} \nu_{ij} s_i s_j f_i(\theta) f_j^*(\theta) \frac{\sin qr_{ij}}{qr_{ij}} \right) \mathrm{d}\Omega \tag{2.21}$$

where ν_{ij} is a smoothing attenuation factor, $f_i(\theta)$ and $f_j^*(\theta)$ are the respective scattering amplitudes for atoms i and j, and qr_{ij} is the product of momentum transfer and the distance between atoms i and j.

For further details, the reader is referred to Blanco et al. [21]

2.3.10 R-matrix

R-matrix is a scattering theory and modeling technique which relies upon a partial wave expansion within the fixed nuclei approximation and is well suited to the modeling of electron and positron scattering at energies in the electron-volt (eV) range as described by Tennyson [22] [23]. For simplicity, we shall consider a diatomic molecule, where the molecule is rigidly attached to the frame of reference as illustrated in figure 2.13. The same analysis can be extended to polyatomic molecules. The fundamental idea of the **R**-matrix method relies upon the division of the electron configuration space into two regions. There is a spherical inner region, of radius typically $10 - 20\ a_0$ (where a_0 is the Bohr radius) centered upon the molecular centre of gravity. This sphere is assumed to contain the entirety of the wave-functions of the N molecular electrons.

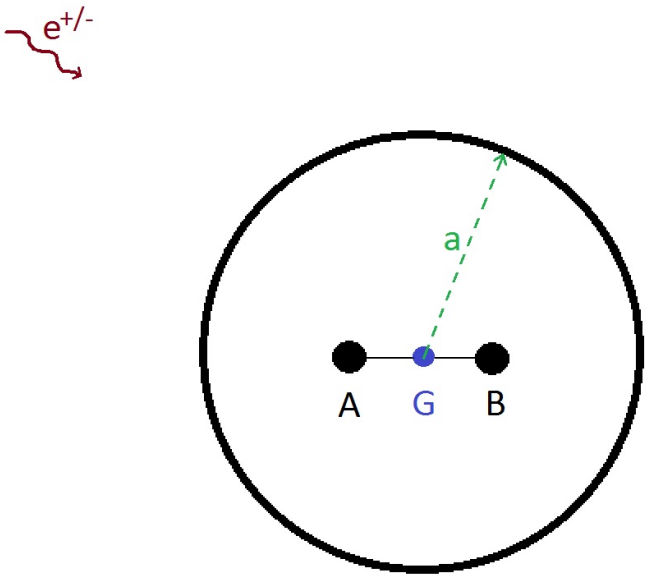

Figure 2.13: **R**-matrix considers the vicinity of a molecule in two regions. An inner region of radius a containing the wave function of the molecule shown here as AB, and an outer region. The boundary between the two regions is centred on the molecular centre of gravity, G. Only the scattering particle (electron or positron) is present in the outer region.

Now, we will consider a radial scattering wave function $F_i(r)$ where i indicates the scattering channel or quantum states of the colliding entities before or after a collision. Simplistically, the **R**-matrix relates the radial wave function to its derivative. When $r =$

a, we can write

$$F_i(a) = \sum_j R_{ij}(a,E) a \frac{\mathrm{d}F_j}{\mathrm{d}r}\bigg|_{r=a} \tag{2.22}$$

indicating that the **R**-matrix is dependent on both distance and energy. In matrix notation, this becomes

$$\mathbf{F}(a) = \mathbf{R}(a,E) a \frac{\mathrm{d}\mathbf{F}}{\mathrm{d}r}\bigg|_{r=a} \tag{2.23}$$

Thus for any radial distance,r

$$\mathbf{R}(r,E) = \frac{\mathbf{F}(r)}{r\mathbf{F}'(r)} \tag{2.24}$$

The relevant wave function for electron scattering in the inner region is typically written

$$\psi_k^{N+1} = \mathcal{A} \sum_{ij} a_{ijk} \Phi_i^N(\mathbf{x}_1 ... \mathbf{x}_N) u_{ij}(\mathbf{x}_{N+1}) + \sum_i b_{jk} \chi_i^{N+1}(\mathbf{x}_1 ... \mathbf{x}_{N+1}) \tag{2.25}$$

where Φ_i^N is the wave function of the i^{th} target state. u_{ij} are the additional orbitals representing the scattering electron. $\mathbf{x}_i$ are the space-spin co-ordinates of the orbital and scattering electron which must obey the Pauli exclusion principle and thus operator $\mathcal{A}$ has been introduced to anti-symmetrise the electrons. The a_{ijk} term is the coefficient of the i^{th} target times the j^{th} continuum orbital in the k^{th} inner region wave function. b_{jk} is the coefficient of the $i^{th} L^2$ configuration in the k^{th} inner region wave function and χ_i^{N+1} is the $N+1$ electron L^2 configuration state function.

For positron scattering, equation 2.25 is adapted to become

$$\psi_k^{N+1} = \sum_{ij} a_{ijk} \Phi_i^N(\mathbf{x}_1 ... \mathbf{x}_N) \bar{u}_{ij}(\mathbf{x}_{N+1}) + \sum_i b_{jk} \chi_i^N(\mathbf{x}_1 ... \mathbf{x}_N) \bar{\chi}_i^1(\mathbf{x}_{N+1}) \tag{2.26}$$

This adaption accounts for several differences between scattering electrons and positrons. There is no longer a requirement for the anti-symmetrising operator $\mathcal{A}$ and the "-" superscript over the χ has been used to indicate the orbital occupied by the positron. Finally, it is necessary to include a spin coupling constraint on the electron part of the L^2 term,

χ_i^N to disallow contamination of the wave function with spin changing transitions.

Some terminology that is encountered involving **R**-matrix modeling is: SE, Static Exchange approximation, where the target wave function is not permitted to relax or polarise after the electron/positron interaction; SEP, Static Exchange plus Polarisation approximation, where target polarisation effects are incorporated into the model; SMC, the Schwinger Multichannel method, where matrix elements are independent of long-range behaviour; Contracted and uncontracted, refers to the orbitals which are included in the calculation. These terms will be referenced in the data analysis.

The reader is directed to Tennyson, [22], Lima et al. [24] and Germano et al. [25] for a more complete description.

Experimental results obtained during the current research are compared with these models as appropriate.

2.4 Data analysis

As mentioned in section 2.2, the scattering energy is determined by the potential difference between the final element in the trap and the target cell. By varying this potential under software control, it is possible to scan across a range of positron or electron energies to determine the total scattering cross-section of the target molecule. The energy of the scattering particle must be both well known and invariant within the uncertainties of the experiment. To measure the uncertainly in the particle energy, the target cell may be used as a blocking element, and by ramping the target cell potential from zero, up to and beyond the anticipated particle energy, the point at which the projectiles no longer reach the detector will represent the beam energy in electron-volts (eV), since the projectiles are electrons or positrons. Figure 2.14 shows an example of a "cut-off" curve, where the beam energy is nominally 20 eV. In this example, the beam is made of positrons. During the formation of the beam, the positrons become thermalised, with a residual energy in the vicinity of several tens of meV. As they are ejected down the beam-line, this residual energy is preserved and contributes to the slope of the cut-off curve.

In the above example, the full-width-half maximum (FWHM) is 90 meV and this is used to characterise the energy resolution of the beam. It should be noted that the beam energy width achieved during the subsequent experiments is reported below and is 60

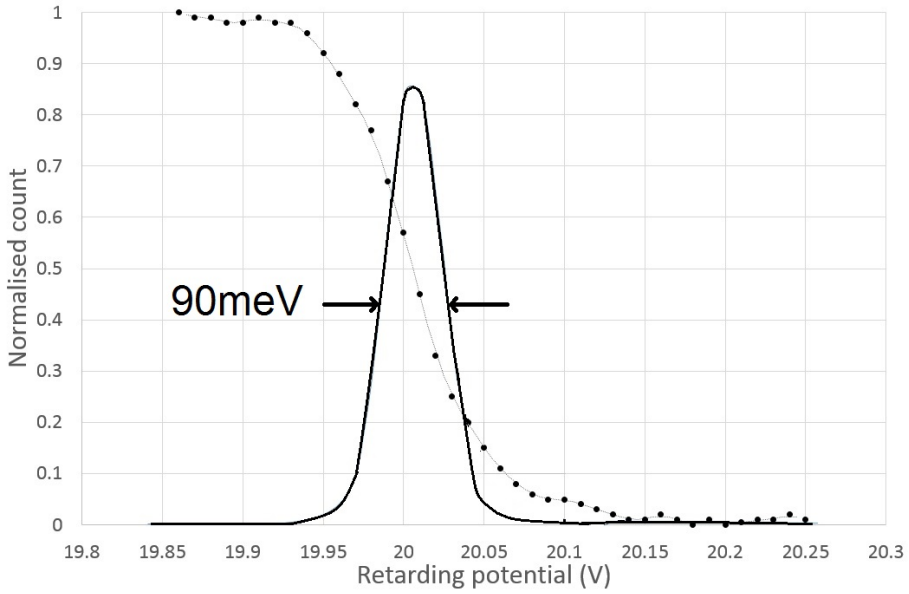

Figure 2.14: Target cell cut-off curve.

meV.

As mentioned in section 2.3.1, the measurement of cross-sections requires a knowledge of the incident beam intensity as well as the unscattered beam intensity, each of which is determined through the potential setting of the RPA. To measure the incident beam intensity, a beam energy below positronium formation or ionisation is required. At this incident energy, the RPA potential is set to zero to allow all incident positrons or electrons to pass through to the detector, regardless of whether they have been scattered. Subsequently, by setting the RPA to a voltage which blocks any scattered positrons or electrons it was possible to measure only the unscattered portion of the beam. Similarly, measurements of the differential cross-section were achieved at each scattering energy, by scanning the potential of the RPA which is located between the scattering cell and the detector, thus measuring the energy necessary to block the scattered positrons or electrons and thence determining a relationship between the scattering energy and the angle through which scattering has taken place per equation 2.4. Positronium formation results in a loss from the incident beam for positrons only. Positronium formation can only occur once the positron beam has sufficient energy, which is equal to the positronium binding energy (6.8 eV) below the first ionisation energy of the target molecule. By measuring the loss from the incident beam at energies above the positronium formation energy, it is possible

to determine the positronium formation cross-section. In the case of electron scattering energies above the first ionisation energy, contamination by freed electrons affects the measurements, limiting the energy range possible for electron scattering measurements. At energies below the ionisation energy, this will not be a factor. Experimentally, it is difficult to distinguish between un-scattered electrons/positrons and those which are scattered by a small angle, given the energy resolution of our beam, which was 60 meV. Thus, to make a fair comparison between calculations and the experimental data, compensation needs to be applied to account for the "missing angle" contribution. Values for percentage loss due to missing angles for the IAM SCAR calculations are given in the results section. Also, electrons/positrons which are scattered by 90 deg may not be measured by the RPA nor captured by the detector, since they can remain trapped in a circular path, orthogonal to the beam-line axis inside the target cell within the measurement cycle. There is no doubt that it is possible that such projectiles may re-scatter and exit the target cell, influencing the measurement of the DCS but not the GTCS.

Figure 2.15 represents a typical analysis curve, showing the normalised projectile count for various retarding potentials with a target in the apparatus. The RPA is only capable of measuring the parallel component of energy, and as discussed previously, parallel energies below the cut-off energy can be associated with angles of deflection.

It should be noted that due to the cylindrical geometry of the apparatus used, back scattering (through angles from 90 deg to 180 deg) is inherently folded onto the forward angular range from 90 deg to 0 deg. This is due to electrons/positrons which are scattered through angles greater than 90 deg being reflected from the first RPA and passing through the target cell a second time as if scattered by the corresponding angle less than 90 deg. Theoretical scattering calculations typically provide the DCS in the range from 0 deg to 180 deg since this is the range through which electrons/positrons can be scattered. Thus for comparison with scattering calculations, the calculated component in the back-scatter region is folded into the forward scattered component with the axis of symmetry being 90 deg.

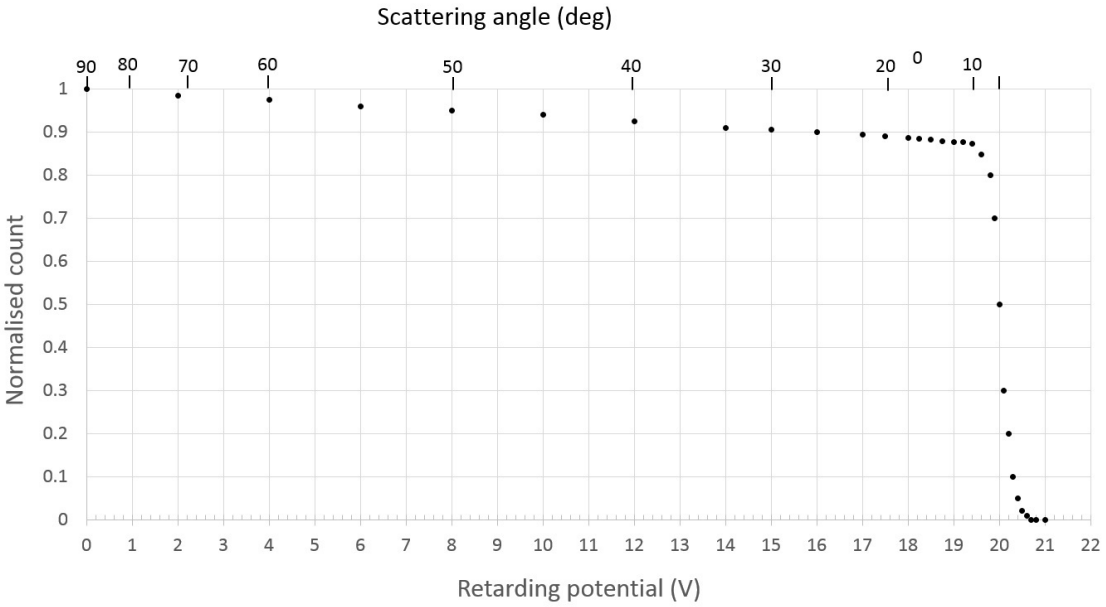

Figure 2.15: RPA2 analysis data. Each data point is a measure of the mean intensity of the positron pulse with a parallel energy component greater than that corresponding to the retarding potential applied to the RPA, with a target gas in the system.

2.5 Results and Discussion

Grand total electron and positron scattering cross-sections as well as the positronium formation cross-sections for thymine are presented and compared with available calculations. For pyridine, grand total electron and positron scattering cross-sections, the positronium formation cross-section and several differential electron and positron scattering cross-sections were obtained and compared with the available theory.

2.5.1 Thymine

Thymine is one of the four nucleobases found in the nucleic acid of DNA. Thymine is also known as 5-methyluracil since it can be derived by the methylation of uracil at the fifth carbon site. The other three nucleobases found in DNA are adenine, guanine and cytosine. Uracil replaces thymine in RNA (RiboNucleic Acid).

From the work carried out by Ferro et al. [26] the equation for the vapor pressure of thymine is given by

$$LogP(kPa) = 12.79 \pm 0.11 - (7016 \pm 51)/T \tag{2.27}$$

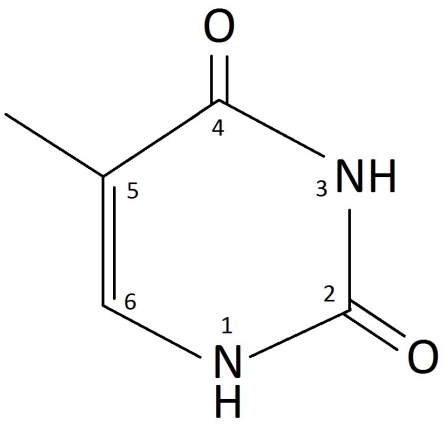

Figure 2.16: Thymine.

The relationship between the cross-section, target gas number density, target cell length and scattered fraction has been seen previously in equation 2.16.

Now, from the ideal gas law, the number density, n is given by

$$n = \frac{N}{V} = \frac{P}{kT} \tag{2.28}$$

where k is Boltzmann's constant and T is the temperature in Kelvin, then we arrive at the equation for the total cross-section for thymine of

$$\sigma = \frac{-k.T.10^{\frac{7016\pm51}{T}} ln\left(\frac{I_u}{I_0}\right)}{l.10^{15.79\pm0.11}} \tag{2.29}$$

Thymine in vapour phase cannot be considered to be an ideal gas due to its size, shape and dipole moment, however within the experimental uncertainties and in the absence of a more complete model, the ideal gas law is considered to be adequate. Multiple scattering events need to be avoided if possible, since such events would adversely influence the results, so around 10% scattering is the aim, giving I_u/I_0 as 0.9. As noted previously, the oven length is 100 mm. From Mozejko and Sanche [1], the total electron cross-section for thymine was calculated as 47.43x10^{-20} m^2. By substituting this estimate into equation 2.29 we arrive at an oven temperature of around 396 K, 123° C.

To address the large uncertainty (almost 50%) attributable to the pressure vapour equation for thymine per equation 2.27, it was decided to use a method described in a paper by Anderson et al. [9] for reporting scattering from uracil, another vapourised

solid target. Since model calculations and experimental measurements converge at higher scattering energies, by normalising the experimental results to the calculations at higher energies, it is expected that the shape and magnitude of the resulting curve will be a reasonable representation of reality.

Energy (eV)	Minimum angle (deg)	Missing (%) IAM SCAR+I	Missing (%) IAM SCAR+I+Born
1	13	16.4	88.4
1.5	10.5	18.6	79.1
2	9	19.4	74.8
3	7.3	19.7	74.6
4	6.3	19.6	66.2
5	5.6	19.7	66.1
7	4.8	19.9	62.0
10	4.0	19.8	64.3
15	3.2	17.8	63.9
20	2.8	16.2	59.7
30	2.3	14.9	52.9
40	2.0	14.3	48.1
50	1.8	14.4	44.3
70	1.5	14.4	40.3
100	1.2	14.7	36.7

Table 2.1: Missing angle and percentage of partial cross-section for thymine.

Table 2.1 gives the missing angle information for the IAM SCAR+I model which was used to generate the adjusted IAM SCAR+I curves in figures in this section. Missing angle information was not available for other models and so those model curves are expected to be above the experimental data by an amount attributable to the missing angle contribution.

2.5.2 Electron scattering

As explained earlier (see section 2.2), electrons are selected as the projectile particle by negatively biasing the source stage relative to the trap stage and by setting the other voltages along the apparatus negative relative to the apparatus ground, including the target cell and RPA.

Grand total electron scattering cross-section

The grand total electron scattering cross-section of thymine was measured in the ranges from 0.5 eV to 1.5 eV and 20 eV to 180 eV. Measurements of electron scattering between 1.5 eV and 20 eV were unsuccessful, primarily due to the contamination of some electrostatic elements at times within the apparatus, as discussed later in section 2.6.

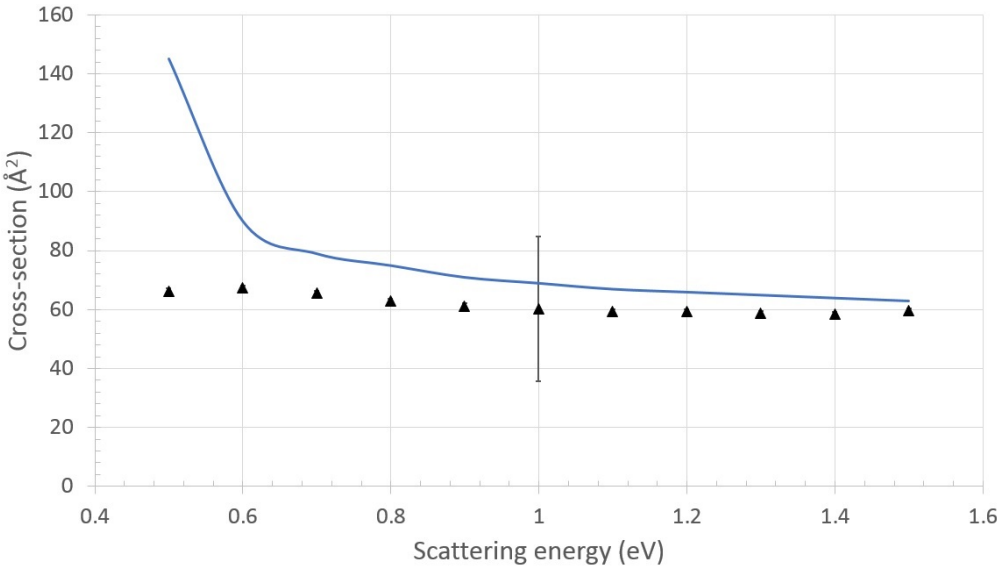

Figure 2.17: Grand total electron scattering cross-section for thymine to 1.5 eV normalised to IAM SCAR theory at 160 eV (triangles - see text). R-matrix uncontracted close-coupling (blue solid line). Statistical errors are smaller than the size of the markers, with the uncertainty due to the error in the vapour pressure curve being indicated only for the data point at 1 eV.

The data obtained and shown in figure 2.17 is in general agreement with the R-matrix uncontracted close-coupling model. There appears to be considerable disagreement with calculations at energies below around 0.7 eV. From previous measurements of polar molecules, there is a large contribution from missing angles, up to 100% of the measured total. Thymine, with a dipole moment of approximately $4 Debye$ [27], falls into such a category, and this effect is likely to be the cause of the apparent disagreement here.

Figure 2.18 shows the experimental data obtained from 20 eV to 180 eV to be in quite good agreement with the IAM SCAR model as well as the model developed by Mozejko and Sanche [1] based on the IAM but augmented with the Binary-encounter-Bethe (BEB) method for electron impact ionisation cross-sections. As mentioned in section 2.4, above the first ionisation energy, the electron scattering cross-section is likely to be contaminated

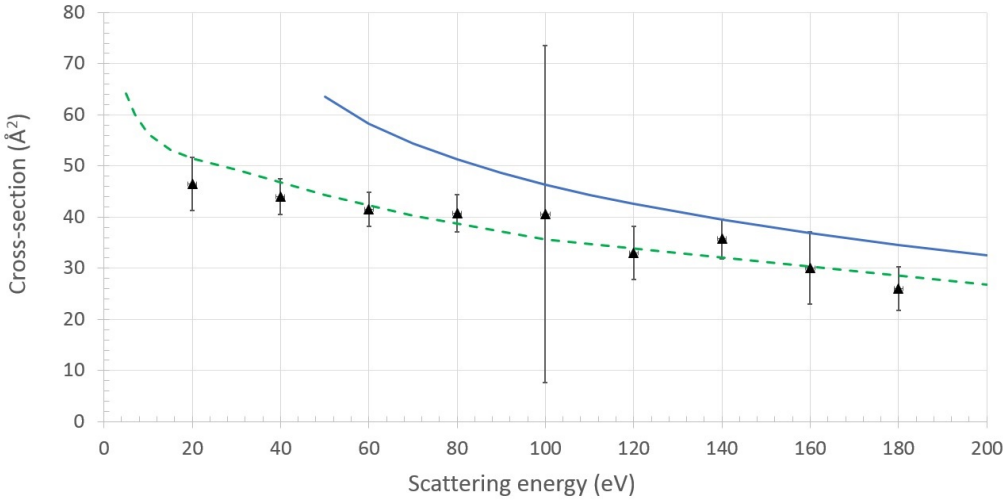

Figure 2.18: Grand total electron scattering cross-section for thymine from 20 eV to 180 eV normalised to IAM SCAR theory at 160 eV (triangles - see text). Model from Mozejko and Sanche [1] (blue solid line). IAM SCAR (dashed green line). Uncertainties are primarily statistical with the error bar for the point at100 eV representing the uncertainty including the uncertainty in the thymine vapor pressure curve.

by electrons freed during the ionisation process. This is expected to reduce the apparent cross-section, although there is little evidence of this.

2.5.3 Positron scattering

Grand total positron scattering cross-section

The grand total positron cross-section was measured over the range from 1 eV to 180 eV. The solid line in figure 2.19 represents the IAM SCAR+I+Born grand total cross-section while the dashed lines represent the IAM SCAR+I over the experimental angular acceptance range, thus excluding the missing angles at the various scattering energies. There is reasonably good agreement at energies above 50 eV with the latter.

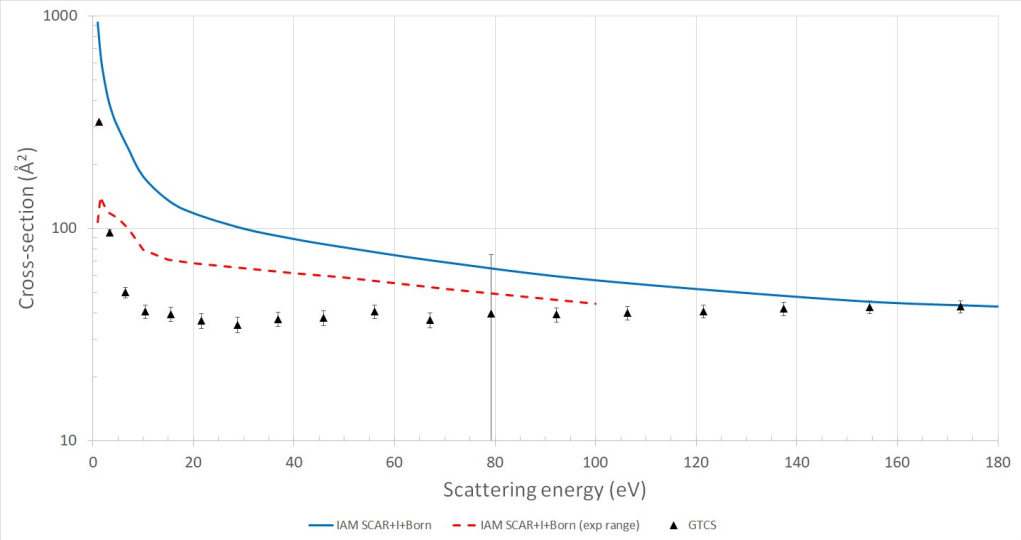

Figure 2.19: Grand total positron scattering cross-section for thymine to 180 eV normalised to the IAM SCAR+I+Born at 170 eV (black triangles). IAM SCAR+I+Born (blue solid line). IAM SCAR+I over the experimental range (red dashed line). Uncertainties are primarily statistical with the error bar for the point at79 eV representing the uncertainty including uncertainty in the thymine vapor pressure curve.

There is, however, significant disagreement between the experimental data and the IAM SCAR+I calculations below about 50 eV. One possible explanation may be increased forward angle scattering. Despite improvements in the IAM modeling, complete accounting for molecular structure remains a challenge, and the discrepancies in the low energy range may indicate an opportunity for further refinement in the IAM SCAR+I model. Additional measurements on thymine in the future should provide further insight into this phenomenon.

Positronium formation cross-section

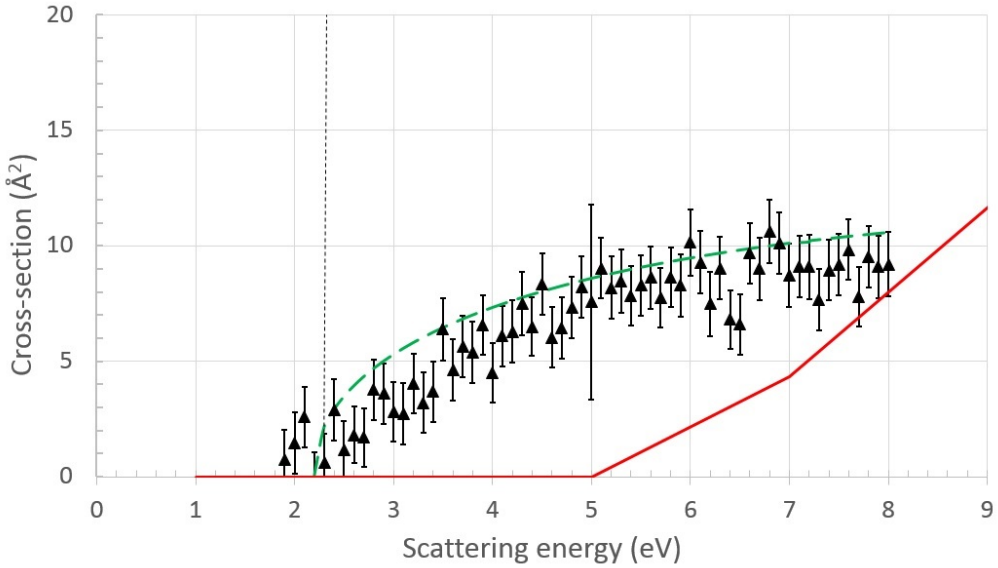

Figure 2.20: Positronium formation cross-section for thymine. Empirical model (green dashed line). IAM SCAR (red solid line). Statistical uncertainties are shown for all data points, with the point at 5 eV showing the typical contribution to uncertainty by the thymine vapour pressure curve. The vertical dashed line indicates the positronium formation threshold.

Positronium formation was measured over the energy range from 1.8 eV to 8 eV due to the threshold being anticipated to be around 2.2 eV, which is 6.8 eV below the ionisation energy of 9.0 eV as reported by the USA National Institute of Standards and Technology (NIST) `https://webbook.nist.gov/cgi/cbook.cgi?Name=Thymine&Units=SI&cTG=on&cIE=on`. As seen in figure 2.20, the positronium formation channel becomes available at the anticipated positron energy. The empirical model cross-section obtained using the method of Mahacek et al. [28], derived from the dipole polarisability parameters, is in good agreement with the experimental data. The IAM SCAR model uses an empirical approach to create a positronium formation cross-section based upon the ionisation energies of the individual constituent atoms and is therefore not expected to be in agreement with the experimental data. This is indeed the case, as can be seen in the figure.

Energy (eV)	Minimum angle (deg)	Missing (%) IAM SCAR+I	Missing (%) IAM SCAR+I+Born
1	17.5	8.1	44.1
2	12.2	8.9	33.5
3	10	7.8	25.9
5	7.7	8.0	19.2
10	5.4	5.9	14.8
15	4.4	3.7	10.7
20	3.8	2.7	7.7

Table 2.2: Missing angle and percentage of partial cross-section for pyridine.

2.5.4 Pyridine

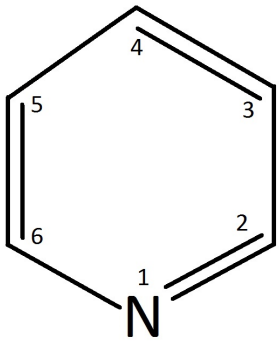

Figure 2.21: Pyridine.

Pyridine is a derivative of the benzene molecule, where the methine group at position 1 is replaced by a nitrogen atom. Pyridine is the root molecule for vitamins such as B_3 and B_6 as well as other biologically relevant molecules. Similarities with pyrimidine, which as been studied previously by Palihawadana et al. [10], where nitrogen replaces methine groups at positions 1 and 3 are observed. Pyridine has an electric dipole moment of 2.2 Debye.

Table 2.2 gives the missing angle information for the IAM SCAR+I and IAM SCAR+I+Born calculations which were used to generate the adjusted IAM SCAR+I curves in figures in this section. Missing angle information was not available for other theories and so those curves are expected to be above the experimental data by an amount corresponding to the missing angle contribution.

2.5.5 Electron scattering

Grand total electron scattering cross-section

Models used to predict electron scattering cross-sections for pyridine are discussed in the paper by Sieradzka et al. [29].

The grand total cross-section for pyridine was measured in the range from 0.5 eV to 2 eV and in the range from 1 eV to 9 eV.

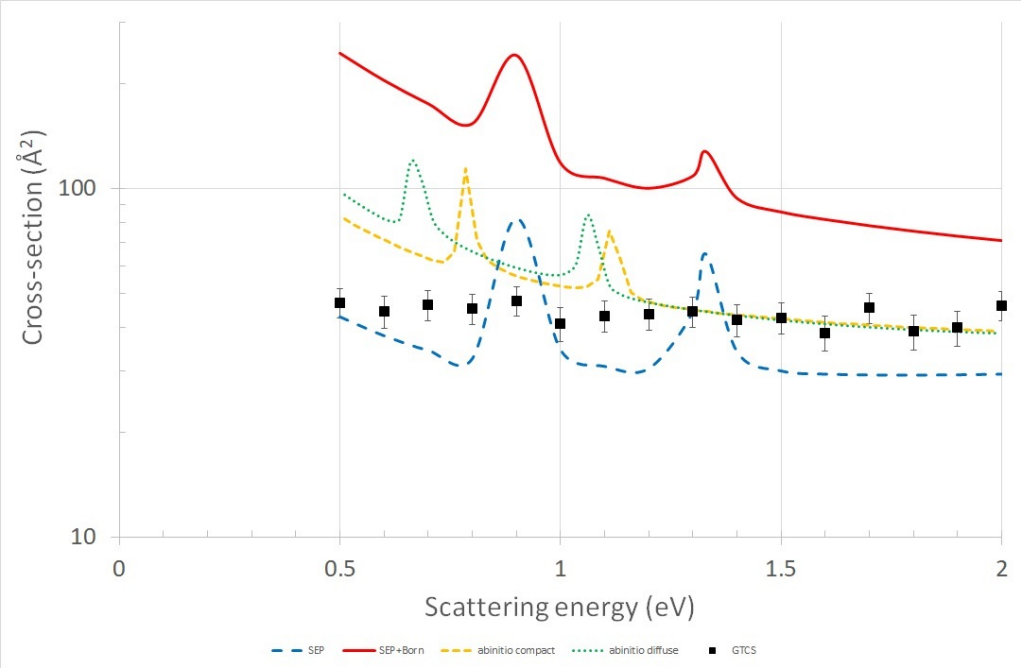

Figure 2.22: Grand total electron scattering cross-section for pyridine to 2 eV. **R**-matrix models using SEP+Born (red solid line), SEP (blue long-dash line), abinitio compact (yellow short-dash line) and abinitio diffuse (green dotted line).

In figure 2.22, the best agreement is seen with the **R**-matrix SEP model excluding Born corrections. Resonance features seen within the calculations are not seen in the experimental results. This may be due to them being artifacts in the calculations, or perhaps due to the experimental energy width of the electron beam of circa 92 meV. Further investigation is warranted using smaller energy increments with a narrower energy beam.

In figure 2.23, a generally monotonic increase in cross-section is observed as would be expected due to larger missing angle contributions at lower energies. The best agreement at the higher energies is again with the SEP + Born calculations. Once the calculations are corrected for the missing angle contribution, the measured data would suggest an

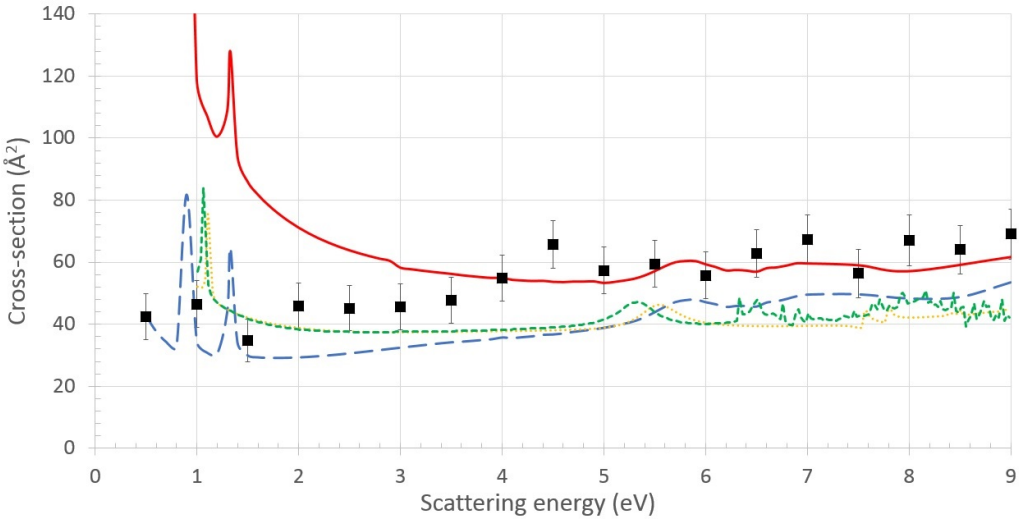

Figure 2.23: Grand total electron scattering cross-section for pyridine to 9 eV. **R**-matrix models using SEP+Born (red solid line), SEP (blue long-dash line), abinitio compact (yellow dotted line) and abinitio diffuse (green dashed line).

underestimation of GTCS by the theories.

Differential electron scattering cross-sections

Differential electron scattering cross-sections for pyridine were measured at 1.2 eV, 2 eV and 3 eV.

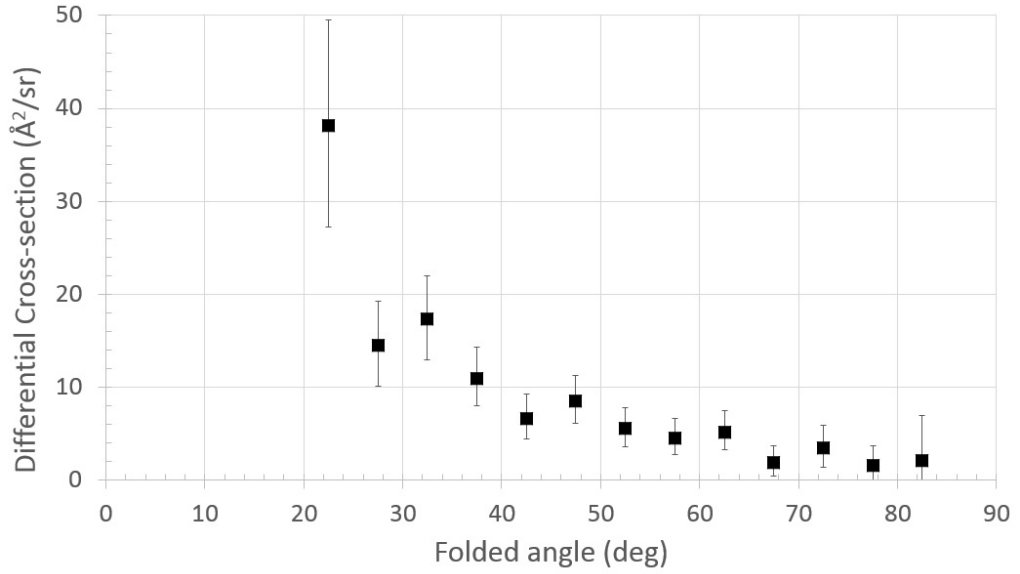

Figure 2.24: Differential electron scattering cross-section for pyridine at 1.2 eV.

Calculations for an electron DCS at 1.2 eV were not available at the time of writing this thesis, however the shape seen in figure 2.24 appears to be consistent with the 2 eV

measurement data in figure 2.25 and is strongly forward-peaked as expected.

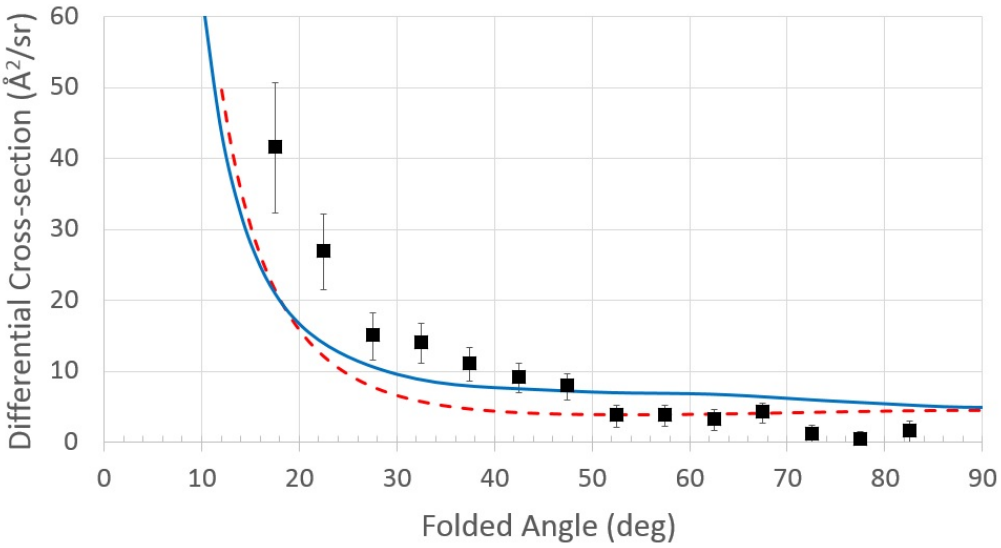

Figure 2.25: Differential electron scattering cross-section for pyridine at 2 eV. **R**-matrix compact (blue solid line) and SMC (red dashed line) models.

Figure 2.25 shows a comparison between the measured data and two folded **R**-matrix models at 2 eV. The experimental data sits above the calculations at less than about 50 deg and then the data sits on or below the SMC calculations beyond $50deg$. The dipole nature of pyridine will result in increased forward angle scattering, but discrepancies remain in terms of the magnitude of this scattering in the comparison between experiment and theory, consistent with the previous conclusions drawn, although agreement at 3 eV is much better.

Figure 2.26 compares measured data at 3 eV with three folded **R**-matrix models. For both 2 eV and 3 eV, the data suggests stronger forward peaking than predicted by theory, which would indicate that the GTCS is underestimated by theory. The fact that the Born correction shows the important role played by rotational excitation is also supported by the measurement of larger than predicted forward scattering.

2.5.6 Positron scattering

Grand total positron scattering cross-section

The GTCS for positron scattering from pyridine was measured in the ranges up to 18 eV as well as the TECS to 8 eV. Review and analysis of the data in this section appears in the paper by Stevens et al. [30].

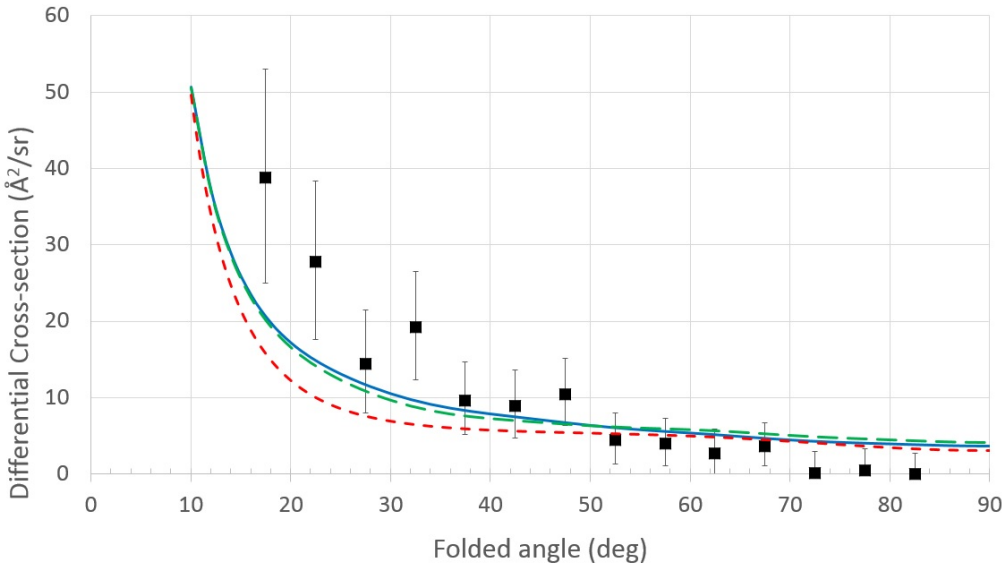

Figure 2.26: Differential electron scattering cross-section for pyridine at 3 eV. Comparison is made with the **R**-matrix compact (blue solid line), diffuse (green long-dash line), and SMC (red short-dash line) models.

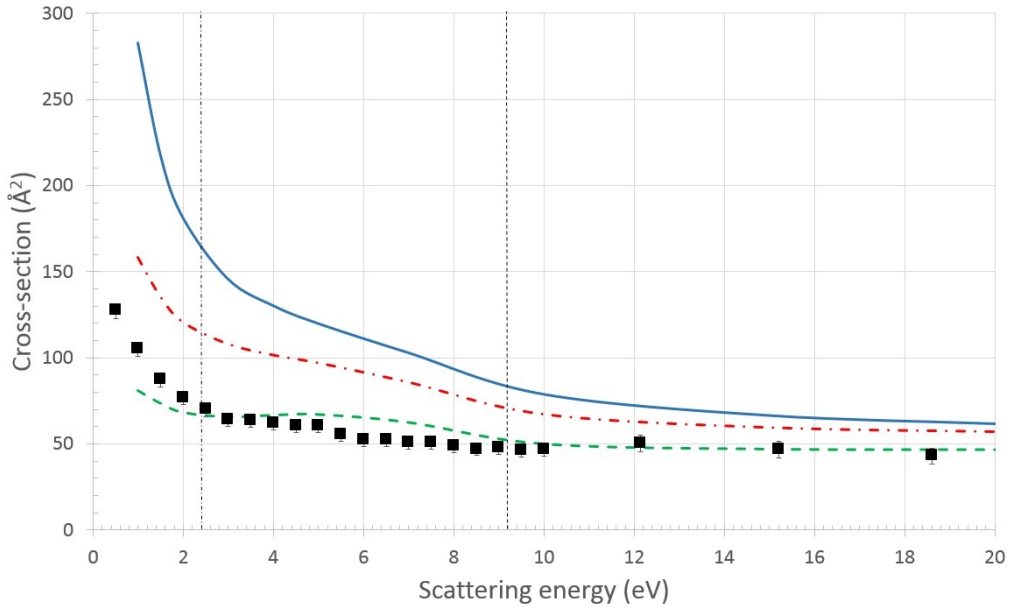

Figure 2.27: Grand total positron scattering cross-section for pyridine to 18 eV (black squares). IAM SCAR+I+Born (blue solid line), IAM SCAR+I+Born for the limited experimental angular range (red dot-dash line) and IAM SCAR+I for the limited experimental angular range (green dash line). A black dot-dash line shows the positronium formation threshold and a black dotted line shows the first ionisation threshold.

In figure 2.27 it can be seen that there is better agreement of the experimental data with IAM SCAR+I than with the Born corrected version. This may mean that the Born correction overestimates the contribution of rotational excitation to the GTCS. Further investigation may be useful in evaluating this. It can be observed that positronium formation only has a small influence on the GTCS, which is consistent with other polar molecules as discussed by Makochekanawa et al. for example [31].

Total positron elastic scattering cross-section

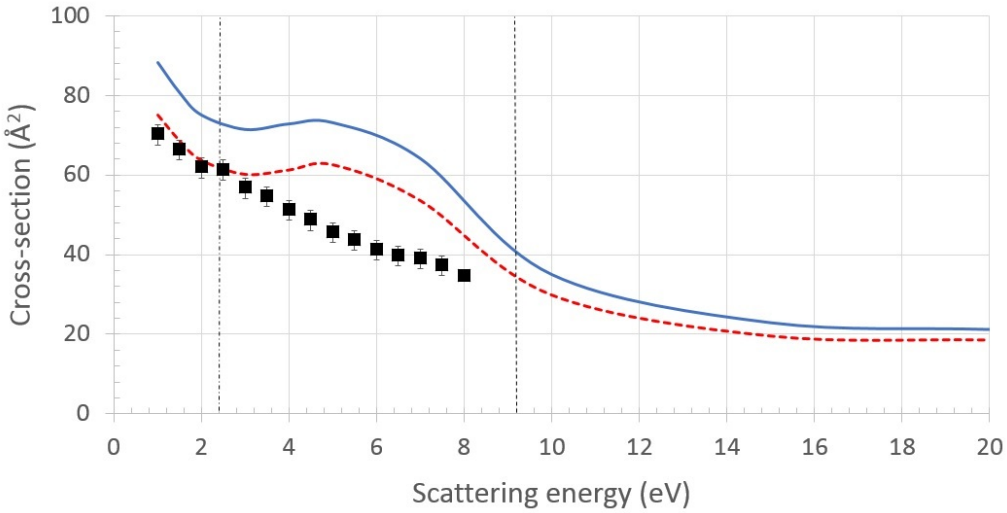

Figure 2.28: Total elastic positron scattering cross-section for Pyridine up to 8 eV. IAM SCAR+I TECS for the full angular range (solid blue line). IAM SCAR+I TECS for the experimental angular range (red dashed line). Again dot-dash and dashed lines show where the positronium channel turns on and the first ionisation energy respectively.

Figure 2.28 shows the experimental data for total elastic (including rotational and vibrational excitations) scattering compared with the IAM SCAR+I model, both for the entire angular range and adjusted for the experimental range of angles. There is close agreement between the data and the adjusted theory for energies up to where the positronium formation threshold, and then re-converges as the first ionisation energy channel is approached. The discrepancy within that region is explained by the inability of the model to adequately account for the positronium channel, similar to the case for uracil. This will be explained further when figure 2.31 is discussed below.

Differential positron scattering cross-sections

Differential elastic scattering cross-sections were also measured at 2 eV and 3 eV.

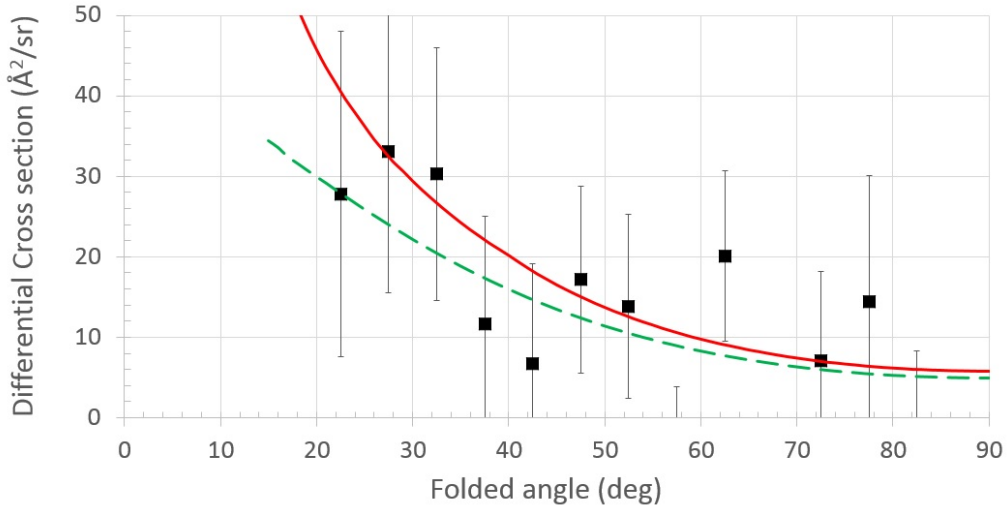

Figure 2.29: Differential positron scattering cross-section for pyridine at 2 eV. Folded IAM SCAR+I+Born (red solid line). Folded IAM SCAR+I (green dashed line).

In figure 2.29 we can see a comparison of the 2 eV experimental data with the two IAM-based models. While there is a quite large statistical uncertainty associated with the experimental data, there is reasonable agreement with the general shape of the models. Together with the GTCS and TECS experimental results, the IAM SCAR+I model appears to be more realistic.

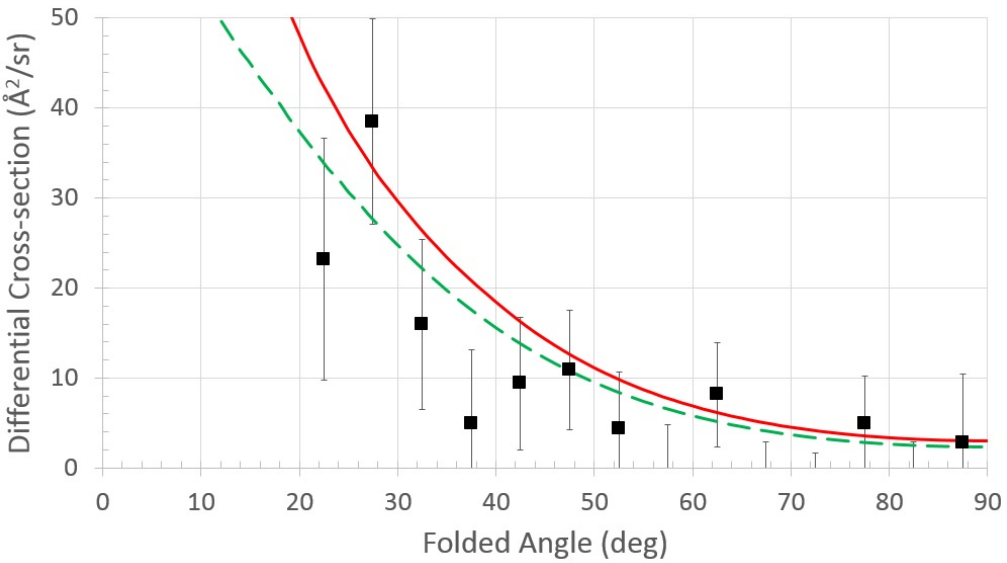

Figure 2.30: Differential positron scattering cross-section for pyridine at 3 eV. Folded IAM SCAR+I+Born (red solid line). Folded IAM SCAR+I (green dashed line).

In figure 2.30 we see the elastic scattering DCS for an incident energy of 3 eV. There is a rather large statistical uncertainty associated with the experimental data, but despite this, it is in broad agreement with the calculations, which are close to each other in the range of the experimental data. We can see that the theories diverge as the angle moves towards zero degrees, with the Born model much larger at the forward scattering angles. Once again, together with the observations in the TECS and GTCS data, it is likely that the calculation which omits the Born approximation is a better description of the scattering process.

Positronium formation cross-section

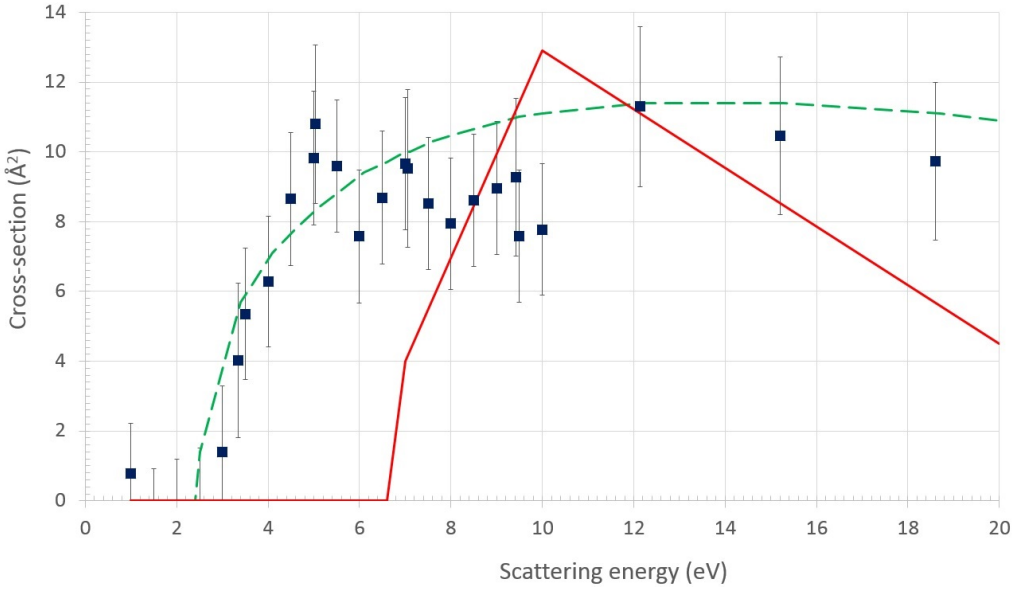

Figure 2.31: Positronium formation cross-section for pyridine up to 19 eV. Imperical model (green dashed line). IAM SCAR+I (red solid line) The black dot-dash line shows the positronium formation threshold. The black dashed line shows the first ionisation energy.

The positronium formation cross-section is shown in figure 2.31. The experimental data is again largely in agreement with the empirical model of Machacek et al. [28] as discussed previously in section 2.5.3. The IAM SCAR model uses an empirical approach to incorporate positronium formation into the calculation, with the threshold calculated from the lowest ionisation potential of the constituent atoms. It can be seen that the empirical model presented by Machacek et al. gives a much better fit to the experimental data, although the IAM model approach gives a peak cross-section that is at least somewhat

consistent with the measurements.

2.6 Conclusion

Various scattering cross-sections for positron and electron scattering from thymine and pyridine were measured. Thymine proved to be more difficult to measure with the available apparatus primarily due to the need to vapourise the solid sample, with the resultant number densities having a quite broad uncertainty when using vapour pressure curve data combined with the uncertainty in the temperature measurement. It has been shown that normalisation to high energy scattering calculations are a much more accurate way to calibrate the cross-sections, at least when measurements are made at the relatively low pressures required by the current apparatus (Anderson et al. [9]). While steps were taken to avoid thymine deposits on critical electrostatic elements, upon opening up the vacuum chamber after the experiment, deposits were found in locations that may have adversely affected measurements. The crucible was filled / refilled a total of three times during the course of the experiment, and electrodes cleaned of any deposits at those times. It was always found that immediately after cleaning, the operation of the experiment was relatively stable for a period of around three weeks, which was seemingly enough time for further deposits of thymine to accumulate. The results presented here for thymine were gathered during the initial post-refill and cleaning process. None-the-less the data obtained is in broad agreement with the theoretical models considered. Pyridine proved to be more straightforward to measure thanks to the relative ease of extracting a gaseous sample from the vapour pressure above a liquid reservoir. A number of elastic differential cross-sections were measured for both electron and positron scattering as well as total cross-sections and the positronium formation cross-section. Again, there was quite good agreement with the calculationss under consideration, although some questions remain regarding the effect of forward angle scattering which is not included in the experimental measurements.

2.7 Proposed future work

As mentioned in the previous section, and based upon the implementation of lessons learned during the thymine measurements, it would certainly be worthwhile examining thymine again using the apparatus. Indeed, differential scattering cross-sections and total

elastic and total inelastic scattering cross-sections for positron scattering from thymine are achievable and ought to be measured in the future. Although a considerable number of biomolecules have now been examined, as discussed by Brunger et al. [32], there remain a number of biologically relevant molecules that still need experimental data for comparison with existing and evolving models. This will aid a more complete understanding of the interaction of positrons, and electrons with human biology. Additional bio-molecules including guanine, adenine and cytosine would be worthwhile targets for future studies. In general, recent models seem to be in good agreement with experimental results for the biomolecules already investigated. Models do struggle to accurately predict positronium formation cross-sections, and thus experimental measurements are essential to describe this process, although it can be seen that the empirical model of Machacek et al. seems to do a reasonable job in most cases. Additionally, the apparatus would be well suited to making measurements of low energy interactions of positrons with matter to form short-lived positride molecules such as hydrogen positride as discussed by Usukuri et al. [33] with annihilation occurring within the volume of the positride molecules and the effects thereof as reported by Danielson et al. [34].

Chapter 3

Liquid target holder

3.1 Introduction

Water, in its liquid state, is vital for sustainable life as we know it. This is evidenced, in part, by the focus of inter-planetary missions, searching for evidence of water in the solar system as a signature for the possibility of life, and more certainly by the effects of drought and climate change on life.

On a more human scale, without the consumption of water, the human condition will soon deteriorate, leading ultimately to death. Therefore the question arises as to what role water plays in sustaining life. One important role that water molecules play is in physically supporting the structure of DNA, without which support, the vital functions of DNA cannot be sustained as discussed by Khesbak et al. [35]. Figure3.1 shows schematically how this is achieved. Water is rather tightly packed around the minor groove in B-DNA and more loosely packed around the major groove. The different grooves are highlighted by the use of different colours in the figure.

Although discussed more fully in Chapter 4, it is worthwhile to now introduce one of the medical imaging techniques used in the assessment of biological tumors, Positron Emission Tomography (PET). It is important to understand the role that condensed state water plays during a PET scan and/or a positherapy procedure where positrons are used as a treatment tool. This leads us to consider the interactions of positrons with condensed state water. Since experimental positron apparatus in the main rely upon a positron beam in a vacuum chamber, experiments with any liquid phase targets are problematic due to the immediate target vaporisation under vacuum. The alternative of implanting a positron emitter within a liquid sample, suffers from a lack of control of positron energy. In the preceding five years or so, a technique has been developed which allows a moderate energy

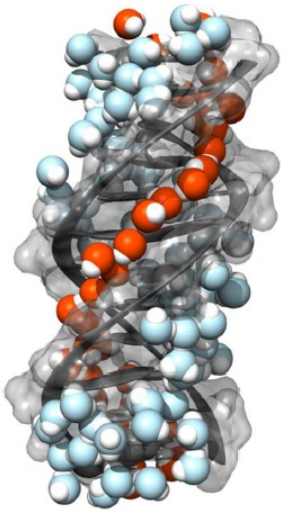

Figure 3.1: Water surrounding B-DNA. [2]
Water is Orange/White in the minor groove and Pale Blue/White in the major groove in the colour version.

(approximately 1 keV to 25 keV) positron beam of 100 μ m diameter to be brought into atmosphere through a thin (30 nm to 200 nm) Silicon Nitride (SiN) window as described by Oshima et al. [13]. Although previously used for solid targets, such an apparatus could be adapted to provide a means for measuring positron interaction with liquid water as the target. In order to achieve this, a liquid water target holder needs to be designed, developed and fabricated. Such a target holder must necessarily carry a known and controllable depth of liquid water. It may also be suited to holding other liquid targets, however water is the liquid of initial interest.

3.2 Theory

Water is the name given to the liquid phase of H_2O, a molecule comprised of a single oxygen atom, covalently bonded to two hydrogen atoms with a bond angle of 104.45°, a permanent dipole moment of 1.8546 D and average bond lengths of 95.84 pm. As one of the more abundant compounds here on Earth, considerable research has been carried out into its behaviour and characteristics under various conditions, however still more can be unearthed regarding this vital molecule.

3.2.1 Modeling expectations

To date, models of positron scattering by water molecules have assumed water to be in vapour phase or soft condensed systems as explained by White et al. [36], Tattersal et al. [11], Zhang et al. [37] and Blanco et al. [38]. Such modeling is largely based upon an extrapolation from the gas phase scattering behaviour and does not take into consideration all of the properties of bulk water, many of which are still the subject of worldwide research. For example, in vapour phase, molecular dipoles will not be aligned unless subjected to an electrostatic field, however with the close molecular proximity in liquid phase, dipole alignment is expected to result in a substantial effect on positron scattering behaviour. Modeling the behaviour of positrons in liquid water is far in advance of experimental results however, and will benefit greatly from experimental data to either substantiate assumptions or provide guidance in amending them.

3.3 Experimental design

Historically, positron and electron scattering experiments, where water is the target molecule, have largely been carried out under high vacuum conditions. Consequently the water has been in the vapour phase. There are experiments where water has been studied in liquid phase using a positron source, such as discussed by Kotera et al. in [39], however none that are targeted at investigating positron penetration depth profiling, which the current research is working towards. Alternative experimental designs have attempted to demonstrate electron scattering from solvated molecules as reviewed by Gorfinkel et al. [40]. The current research investigates the design and fabrication of a structure which will allow a known depth of liquid water to be targeted by a variable energy (1 keV - 25 keV) positron beam. The fabrication technique may lend itself to further development of a liquid water target which could be placed inside a high vacuum chamber as discussed in section 3.4 below, with the intention of additional testing and/or verifying existing models.

3.3.1 Initial design parameters

From the outset, the ambition of this part of the project was to develop a mechanism by which a determinable and known depth of liquid water could be presented to a horizontal,

physically narrow beam of moderate energy positrons in air. By conducting a battery of such experiments with various depths of liquid water, it is suggested that knowledge could be gained regarding the behaviour of positrons in liquid water. Lifetimes in water and lifetimes in a silica substrate ought to be separable, so determining the number of positrons that completely penetrate certain depths of liquid water should allow extraction of data useful for comparison with existing condensed water models. Water sample holders would need to be of uniform depth in the range from 1 μ m to 10 μ m with a uniformity of better than a 100 nm, as advised by Professor Ron White [41].

An initial concept for a vertically aligned water sample was based around using capillary action to stabilise the water sample. By plasma etching a valley between an array of silica posts on a silica substrate, liquid water may adhere to the valleys and posts in the substrate whilst mounted vertically, without the water sample flowing away. The posts are needed to provide a framework to support a thin film of water, by acting hydrophilically. An initial design was undertaken by considering a suitable post diameter and separation. Using a triangular array of posts of diameter w, which are located on the circumference of an imaginary tube of diameter $2a$ (see Figure 3.2), it is possible to formulate a crude approximation to liquid water being drawn up a glass tube via capillary action. Of course, the fraction of such a tube that is provided by the posts for surface tension is reduced by a factor of $3w/2a$. The aim is to achieve a uniform depth of liquid water in a vertical ori-

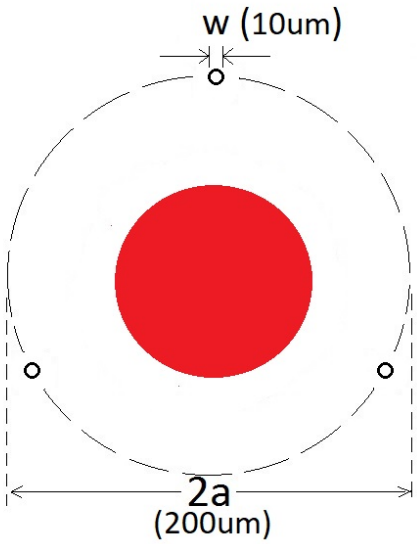

Figure 3.2: Initial sample mask design. The red spot in the centre indicates the anticipated positron beam size.

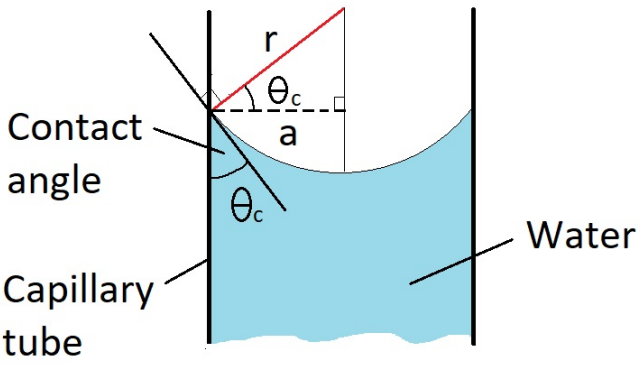

Figure 3.3: Water in a vertical capillary tube showing the contact angle and meniscus.

entation. Now, from Figure 3.3 it can be seen that the radius of curvature of the meniscus (r) of a vertical capillary tube is given by equation 3.1

$$r = \frac{a}{cos(\theta_c)} \tag{3.1}$$

where θ_c is the contact angle between the water and glass. A uniform water depth across an entire surface implies an infinite radius of curvature. To maximise the meniscus radius, one either needs to increase a and/or increase θ_c. The limits on a are introduced by the geometry of the positron beam, and the ability to align the beam spot away from the posts. Whilst the contact angle can be modified through silanation of the surface, one must be mindful that the imaginary capillary tube will ultimately be orientated horizontally. The contact angle is reliant upon not only the magnitude of the acceleration due to gravity but also its direction as described by Finn et al. in [42], so artificially increasing the contact angle will only work against our aim of retaining water at the vertical substrate surface. Similarly, if the contact angle is too small, the water will not be sufficiently supported by the posts. Now, owing to the horizontal orientation of our imaginary capillary tube (i.e vertical orientation of the substrate), caution is required if hoping to invoke Jurin's Law per Barozzi et al.'s explanation in [43] since there is evidence that an almost horizontal orientation has no visible effect on the shape of the meniscus in a capillary tube of small diameter.

While first principles have been used when designing the initial target holder herein,

the author is aware that much more investigation is required before retention of water in an array of posts can be completely and accurately modeled. Using the established hydrostatic equations derived by Young and Laplace as a basis for design, one can envisage that it is sufficient to provide a water - silica interface length such that the capillary force counters the weight of the water held within the region of interest. From the Young relationship [42], the height of a liquid column in a capillary is given by equation 3.2.

$$u_0 = \frac{2cos(\theta_c)}{\kappa a} \tag{3.2}$$

where u_0 is the height of the liquid column and κ is given by equation 3.3

$$\kappa = \frac{\rho g}{\sigma} \tag{3.3}$$

where ρ is the density of water, g is the magnitude of gravitational acceleration, σ is surface tension and a is the radius of the capillary tube. A rearrangement shows us that the force due to gravity on the column of water is exactly opposed by the capillary force, and that the capillary force is thus given by equation 3.4

$$F_c = mg = 2\pi a\sigma cos(\theta_c) \tag{3.4}$$

where m is the mass of water in the column.

Since the cross-section of the capillary tube is circular, it can be seen that the capillary force F_c is the product of the contact line length $2\pi a$, the surface tension σ and the cosine of the contact angle $cos(\theta_c)$. As a first approximation, therefore, the capillary force required to suspend a given mass of water can be considered to be proportional to the contact length, assuming the contact angle and surface tension remain unchanged. The mass of water to be suspended on the holder can be approximated by a layer up to 10 μm deep over a 1 cm^2 surface, giving a volume of up to 10^{-9} m^3. Now, assuming a density of 0.997 gm^{-3} [44] this gives a mass of 9.97x10^{-7} kg and thus a weight of 9.77x10^{-6} N. For a value of σ equal to 0.072 Nm^{-1} (see [45]) and a contact angle of 70 deg (3.7), this gives a minimum required contact length of almost 0.4 mm (0.397 mm). Due to the many assumptions and approximations used to achieve this contact length, it is considered reasonable to increase this by two orders of magnitude in the final design. Hence, a contact length of 40 mm

was the aim. Only half of the circular circumference of each post will be able to oppose the force of gravity, and the posts should be distributed geometrically so as to allow for sufficiently large areas on the target holder to be post-free such that the positron beam may not interact with the silica. Allowing for a contact angle of around 70 deg and a $a : w$ ratio of 10 : 1, a value for a of 100 μm, and w of 10 μm gives a geometry which is compatible with the AIST positron beam diameter. Figure 3.2 shows the triangular arrangement of posts along with a region in red indicating the AIST beam area.

Implementation of this arrangement would have required fabrication of a dedicated lithographic mask. As a matter of convenience and to demonstrate a proof of principle, and since a somewhat similar mask already existed within the Electronics Materials Engineering department at ANU, it was decided to proceed using the existing mask to fabricate samples, despite knowing that the considerably smaller post separation may be problematic. It is still expected that this mask will produce a sample which will be indicative in terms of water retention to the vertical surface. The existing mask incorporated a square array with a post diameter of $10\mu m$ and a post separation of 60 μm. See Figure3.4 for a schematic of the sample design when using the available mask.

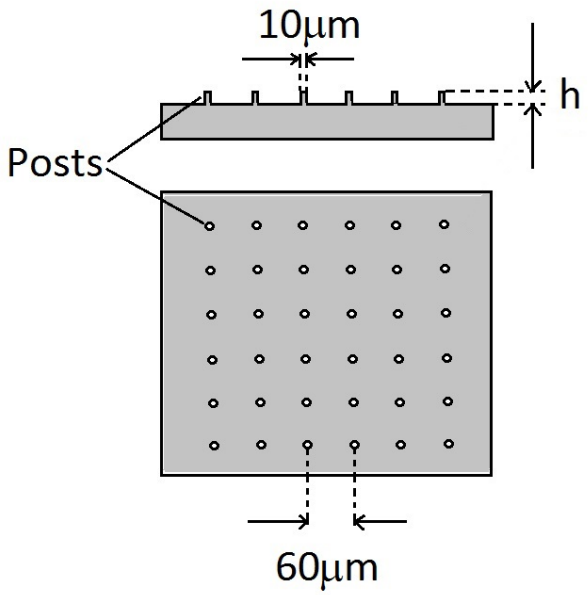

Figure 3.4: Schematic of a possible sample using the existing mask.

3.3.2 Fabrication

With guidance from the Electronic Materials Engineering department, and using the Inductively Coupled Plasma (ICP) Versaline LL equipment within Australian National Fabrication Facility (ANFF), several liquid target holder samples were produced by taking a 1 cm^2 fused silica wafer and using photo lithography to apply photo-resist in the positions of the posts. Exposed silica was then etched away with a mixture of Sulfur Hexafluoride (SF_6) at a flow rate of 25 standard cubic centimetres per minute ($sccm$) and Fluoroform (CHF_3) at a flow rate of 25$sccm$, to a depth of around 10 μ m. Verification of the post height, relative to the etched base, was carried out using the FEI Verios scanning electron microscope at ANFF. Measured depths were 9.9 μ m and 11.2 μ m. The 9.9 μm sample was then mounted on the sample platform of a Goniometer as shown in Figure3.5. Figure3.6 shows an image of the sample made using the mask, taken with the Goniometer camera.

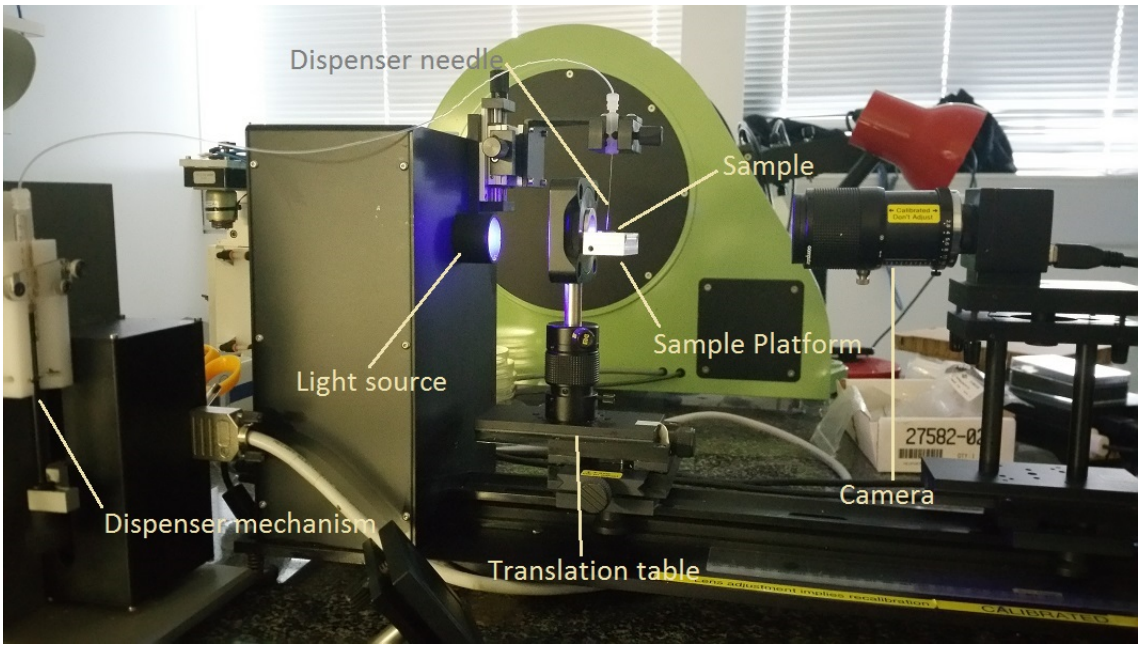

Figure 3.5: Goniometer apparatus showing the positioning of light source, camera and water dispenser.

Deionised water was then dispensed onto the sample and the contact angle was measured. Figure 3.7 shows that a contact angle of around 70 deg was measured. The platform was then rotated slightly to gauge the effectiveness of the posts in retaining the film of water. With a layer of water the same depth as the posts remaining on the sample holder,

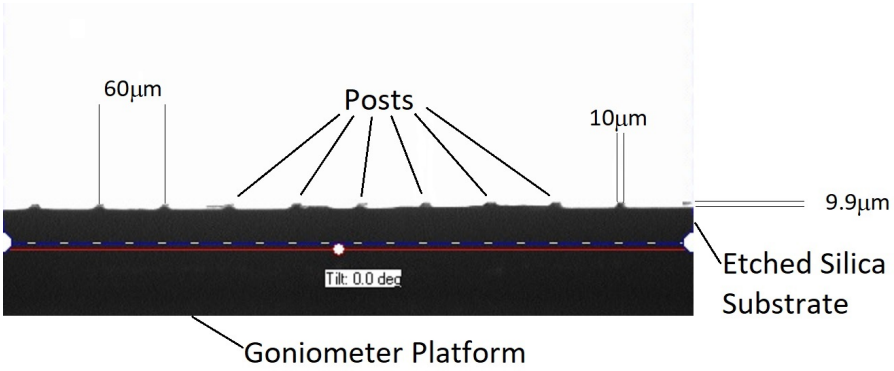

Figure 3.6: Initial sample profile view.

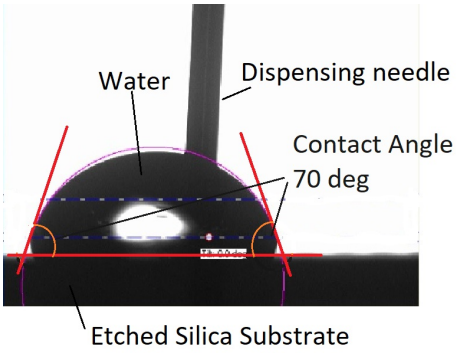

Figure 3.7: Contact angle measurement.

it was only a matter seconds before the water evaporated completely from the surface. The laboratory housing the goniometer had a relative humidity of around 60%, and an ambient temperature around 24 deg C. Birdi et al. [46] experimentally showed a linear relationship between the radius of a spherical segment water drop on glass and the rate of evaporation, with a slope of 9.2119 x 10^{-5} g/min/mm. By extrapolation, an order of magnitude approximation could be made for the present glass - water interface surface area of 1 cm^2, corresponding to an equivalent circular radius of 5.7 mm. The evaporation rate should be approximately 5.2 x 10^{-4} g/min, or 9 x 10^{-6} g/s. Now, the volume of water held on a square cm of silica to a depth of 10 μ m is 1 x 10^{-4} ml, and the observed evaporation is entirely consistent with this. At AIST, assuming similar conditions with such an evaporation rate, the water depth would be varying continually, whereas for positron interaction measurements, the water depth needs to be maintained to within a matter of a few tens of nanometres. This behaviour was not anticipated and was only observed during the measurement of contact angle over a matter of less than a minute. This represented

a stumbling-block in the original design. In order to maintain a constant depth of water, either the experiment would need to be conducted in an environment with precisely controlled humidity such that equilibrium could be achieved, or water would need to be constantly supplied to the target holder at the same rate as it was evaporating. Either of these options may be achievable, however the degree of complexity in implementation would be increased substantially and it was decided to pursue an alternative approach. Not withstanding the evaporation of the thin film of water applied to the silica substrate, during the rotation of the sample, retention by the post structure was evident in the seconds before the water had evaporated. The conclusion drawn from this target holder design was that although in principle the post concept provided the necessary support for the water sample, evaporation meant that an alternative design was required in order to advance the proposal.

3.3.3 Re-design and fabrication

Based upon the knowledge that a thin film (as thin as 30 nm) of SiN had been used successfully as the aperture window on the AIST experimental apparatus, [13] it was proposed that a similar window could be used as a lid over a target water well, thereby allowing the water sample to be contained within a small volume and presented as a vertically oriented target without the liquid being exposed to the atmosphere and hence evaporating away. The addition of another layer of silicon nitride would need to be taken into account when analysing depth penetration data. A simple check was undertaken using the already fabricated valley and post sample, by placing a thin film of SiN over the top and applying water to the interface between the SiN film and the silica wafer. It was evident that capillary action allowed the water to enter the spaces between the SiN and gaps between the silica substrate posts.

Figure 3.8 shows water being dispensed onto the substrate such that it flowed between the (green framed) SiN film and the substrate.

Figure 3.9 shows a profile view of the SiN frame lying atop the silica substrate prior to water flowing into the gaps. Air gaps can be seen between the two surfaces and the posts can also be seen.

Figure 3.10 shows a profile view of the SiN frame atop the silica wafer after water has

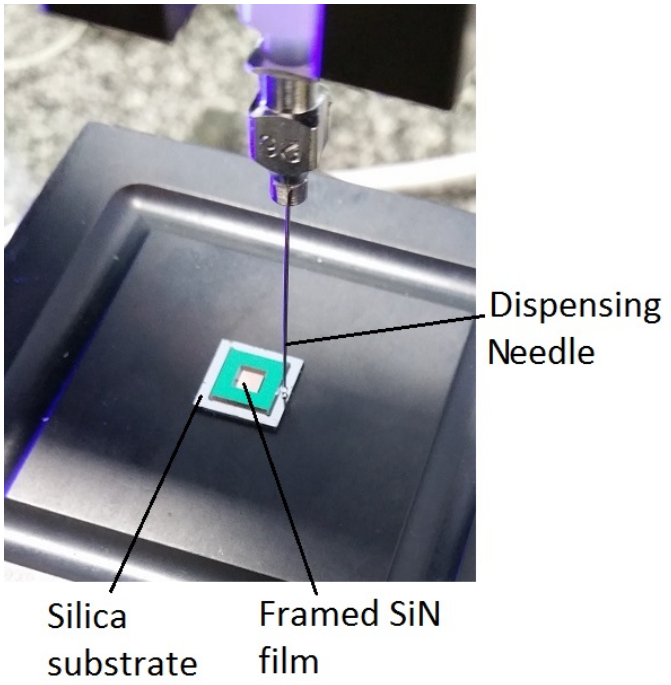

Figure 3.8: SiN on silica wafer - Top view.

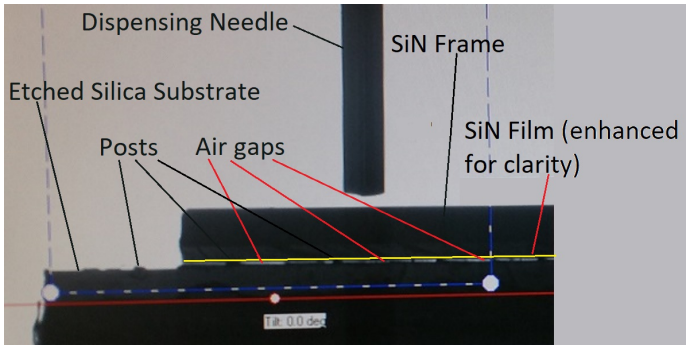

Figure 3.9: SiN on wafer - Side view with air gaps visible.

filled the gap between the two surfaces.

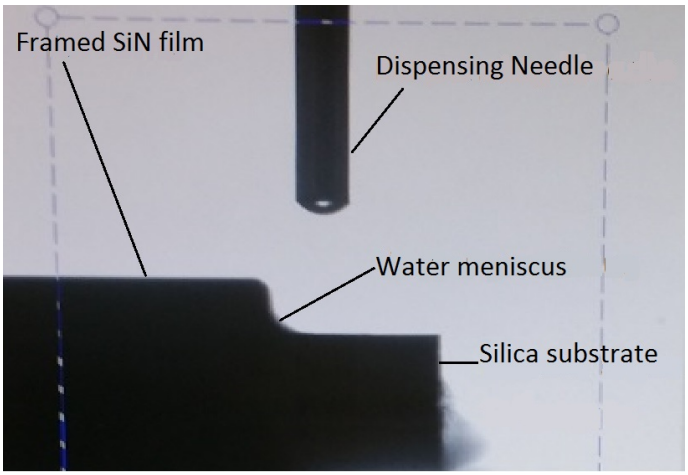

Figure 3.10: SiN on wafer - Side view with water - no longer any air gaps.

It was evident that if a SiN film was to be used to cover the silica substrate, there would be no need to include posts in the redesign. Indeed, the inclusion of posts in the original design had posed a further difficulty in that the target would need to be positioned precisely in the positron beam so as the positron beam would only interact with the water in the target, and not the silica posts (see Figure 3.2). Hence, a re-design was undertaken. The new design required a means by which liquid water could enter the well, as illustrated in Figure 3.11

The substrate was a 1 cm square piece of silica wafer with a central region etched to a pre-determined depth (i.e. the well depth). Samples with well depths of approximately 1 μm, 2.5 μm and 5 μm were fabricated. As mentioned above, a thin SiN film was then placed over the top of the substrate, thereby forming a cavity of known depth. The only available SiN films for this part of the design testing were 500 nm in thickness. While these were suitable for design test purposes, in the final implementation, considerably thinner films would be required as discussed below. This construction was then lowered into a liquid water bath until the inlet hole was immersed. Capillary action, resulting from the inter-molecular cohesive and adhesive forces, provided the mechanism by which the water was lifted vertically into the cavity and up to near the breathing hole at the top.

The assembly is then removed from the water bath and the water remains trapped inside the well. Due to the small size of the interface between the water and atmosphere of approximately 0.2 μm^2, evaporation is minimal, and certainly insufficient to complete

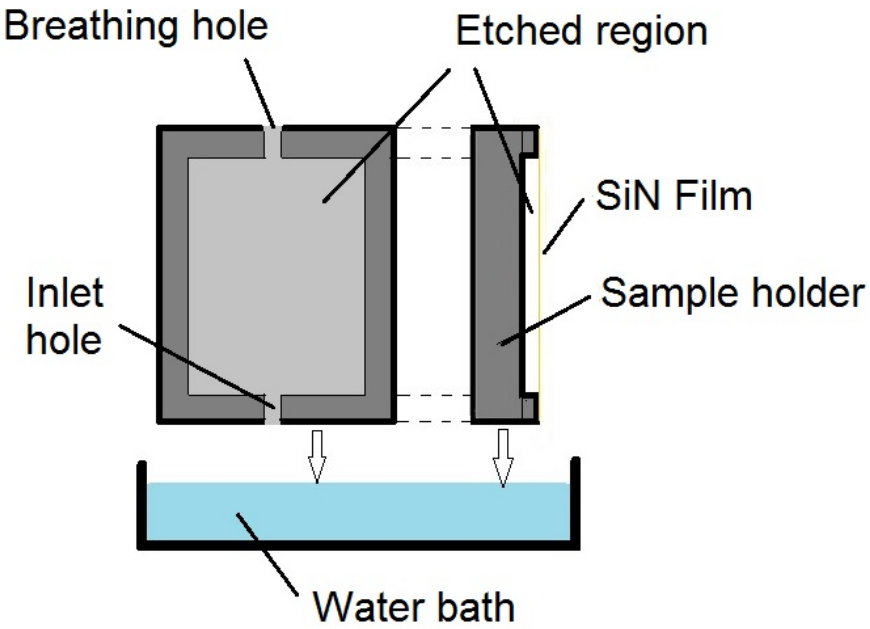

Figure 3.11: Schematic of silica sample holder with SiN cap showing inlet and breathing holes.

an experiment which is expected to be completed in under an hour. In a manner similar to the previous method, samples were produced with depths of 0.8 μm, 2.3 μm and 4.7 μm with a uniformity of better than $\pm$50 nm. These depths and uniformities were verified using the Dektak Surface Profiler at the ANFF lab.

3.3.4 Sample testing

It was then demonstrated that deionised water was indeed wicked up into the well. Figure 3.12 shows the progression of the meniscus for the 4.7 μm sample, and the following URLs and QR codes in the margin currently link to the videos of the demonstrations.

1 μm Well

`https://www.youtube.com/watch?v=txEO8KHa-b0&feature=em-upload_owner`

5um Well

`https://www.youtube.com/watch?v=y3iBNdcU5eQ&feature=em-upload_owner`

Note that the SiN film which was used in this trial was 500 nm thick, considerably thicker than that proposed for the application experiment. Further tests using thinner SiN films will be necessary to determine whether they can withstand the tension and stress created by the capillary action of the water. Since a 30 nm, square mm film has been shown to withstand pressure differences of one atmosphere, it is expected that the small volume of water involved in the structure of the target will not pose any difficulty.

The thinnest possible SiN film is expected to provide the opportunity to collect the most significant positron interaction data. As mentioned previously, while a 30 nm film of SiN has already been successfully used as the beamline exit window at AIST, the additional SiN lid over the liquid target will need to be accounted for in data analysis. Consideration will need to be given to reducing the thickness of the beamline exit window to below 30 nm if possible.

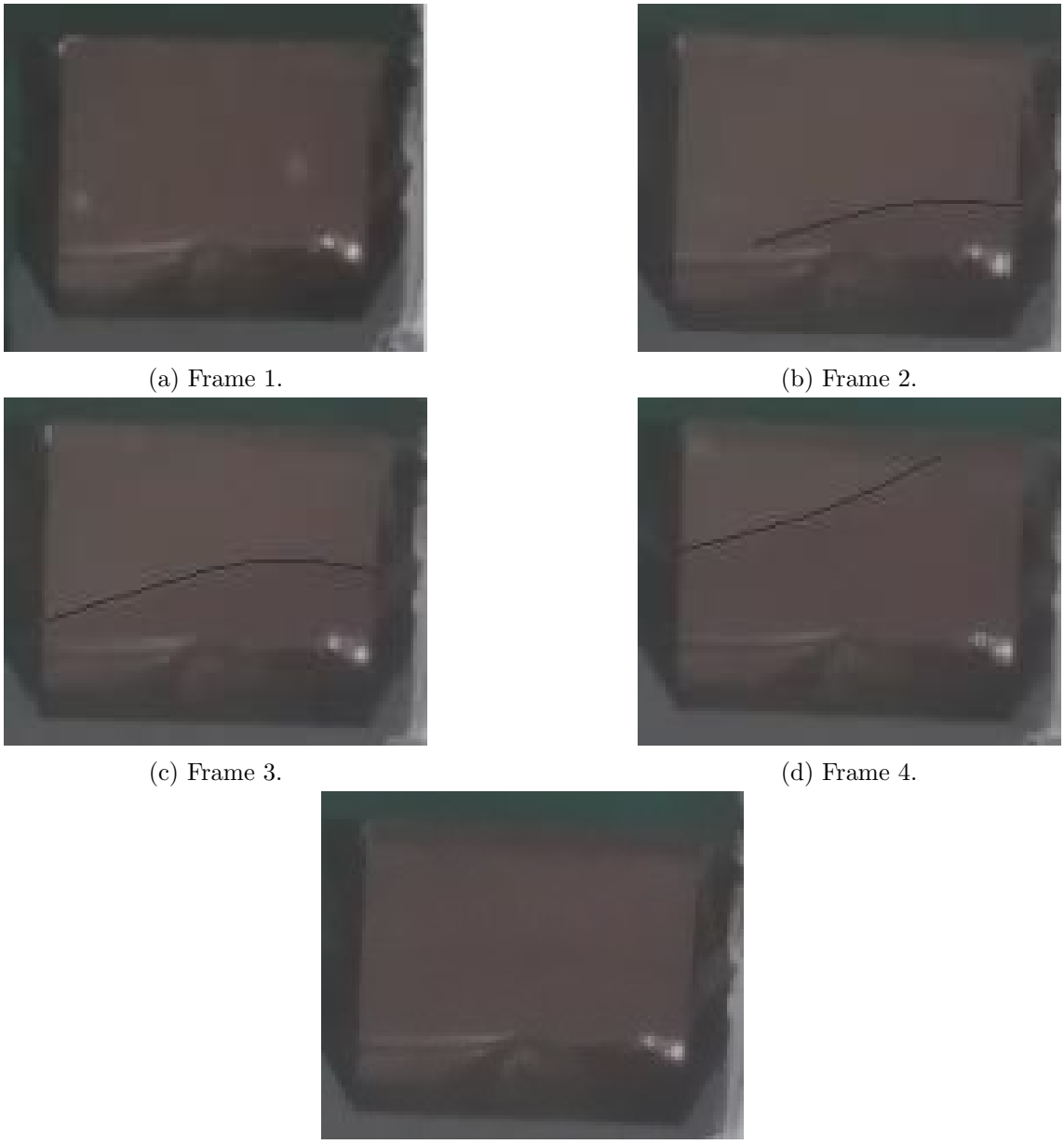

(a) Frame 1.

(b) Frame 2.

(c) Frame 3.

(d) Frame 4.

(e) Frame 5.

Figure 3.12: Progressive time-lapse images of water filling the gap between the SiN window and the Silica Substrate. In Frame 1, there is no evidence of water ingress. In Frame 2, there are signs of water near the base of the Frame. In Frame 3, water can be seen to have progressed up the well. In Frame 4, the water is nearing the top of the well and in Frame 5, the entire well is filled with water. Note that in Frames 2,3 and 4, a line has been added to guide the eye regarding the water level.

3.4 Future work

Figure 3.13 schematically represents the proposed experimental arrangement at AIST. However, as mentioned, before it can be trialled, tests need to be conducted to verify the ability of thinner films of SiN to withstand the stress of the water. Initial experiments using this configuration will aim to test simulations of positron penetration depths as a function of energy with the intention to evolve both the experiment and theory to allow much more detailed information to be gleaned in the future. It is proposed that further

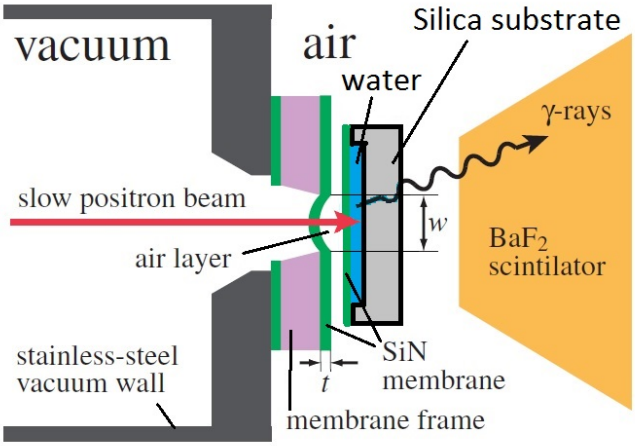

Figure 3.13: Proposed AIST configuration.

evolution of the target holder be undertaken with a view not only to the option of mounting it as a target for the AIST in-air beam, but also as a target in the ANU Materials beamline configuration, where DBS (Doppler Broadening Spectroscopy) and PALS (Positron Annihilation Lifetime Spectroscopy) measurements could be made for various depths of liquid water. It is believed that such fabrication would be feasible using the facilities at the ANFF ACT node at ANU. Investigation of an integrated fabrication process is suggested, where the SiN film is deposited onto a silica wafer substrate and then the substrate is etched away from beneath. Adaptation for use with other liquid targets is also a worthwhile future aim. Finally, it may be worth investigating the development of a target holder with front and back SiN windows for mounting within the ANU atomic and molecular positron beamline and attempt to make transmission scattering measurements.

Chapter 4

Positron Emission Tomography (PET) image enhancement

4.1 Introduction

PET is a medical imaging technique which takes advantage of the interaction between matter and anti-matter to produce gamma-ray photons of a particular energy ($511keV$), which are then detected and used to construct a three-dimensional image of structures internal to the body. PET imaging provides benefits in identifying abnormal biological activity, such as tumors, as well as in assisting medical practitioners in the prescription of suitable treatment options and thence the assessment of tumor progress or regress. The procedure involves the intravenous injection of a positron emitting isotope, such as ^{18}F, attached to a biologically relevant molecule such as glucose, whereby the molecule accumulates at the region of interest (ROI). The isotope then decays via the emission of positrons which then thermalise and either form positronium which then annihilates or they directly annihilate with atomic or molecular electrons. Theoretical models of the positron path to thermalisation, which are ever evolving, rely upon experimental results from the laboratory scattering of positrons from various atoms and molecules, including biomolecules and water, which were the subject of previous chapters in this work. A database of experimental positron scattering cross-sections is useful and necessary to ensure that the models are consistent with reality as closely as possible. Any unexplained behavior (experimental and/or theoretical) therefore becomes the subject of more intense investigation so that any anomalies can be reasonably explained and accounted for.

The primary factors contributing to the resolution, and hence interpret-ability and

thus usefulness of PET images include:

i. PET scanner detector size

This is set by the system manufacturer and is typically in the region of 4 mm to 6 mm for whole (human) body PET systems. Small animal PET systems use detectors in the vicinity of 1 mm to 3 mm. The contribution to overall spatial resolution will be denoted R_d.

ii. Typical positron range in-vivo

This is a characteristic of the mean positron energy as it is emitted from the radionuclide and can range from 2.6 mm for ^{82}Rb to 0.2 mm for ^{18}F. There is also some tissue-type dependence. The selection of radionuclide is primarily made on the basis of the biology and chemistry required in targeting a specific physiological uptake of the radio-nuclide, to allow accumulation of activity at the ROI. Hence, the positron range is partly determined by the physiology of interest. Reduction in the positron range is the subject of the current research. The contribution to overall spatial resolution will be denoted R_r.

iii. Non-colinearity of 511keV gamma-ray photons and detector distance from from the annihilation site

This is determined largely by the separation distance between the opposed gamma-ray detectors, although the momentum at annihilation also plays a role. The contribution from this aspect to overall resolution will be denoted R_{nc}.

There are a variety of accounts which explain and describe the various contributions to overall PET image resolution [47–50]. They each describe the contribution to overall spatial resolution by the above factors as adding in quadrature.

$$R_{Tot} = \sqrt{R_d^2 + R_r^2 + R_{nc}^2} \tag{4.1}$$

Although detector size R_d represents the largest factor contributing to overall system resolution for whole body PET systems, a substantial reduction in positron range R_r is expected to improve image resolution at least for small animal PET systems, and may be

observable for whole body PET systems. It is the aim of the present study to test this hypothesis by using the Canberra Hospital-based whole body *Philips Gemini Gen* − 3 *PET/CT* scanner, since a small animal PET system was not immediately available. The *Gen* − 3 machine is a combined PET and CT (Computed Tomography) machine. This machine is an evolution of the *Gemini TF PET/CT* scanner, evaluated by Surti et al. [51]. Image resolution is typically indicated by the full width half maximum (FWHM) intensity and the full width tenth maximum (FWTM) intensity. These are used as the criteria to determine whether any resolution improvement has been achieved in the current study [52]. The current research investigates two approaches to attempt to decrease the positron range. Initially layers of platinum are used to sandwich the positron emitter during a scan, and subsequently a heavy metal colloid is formed with the positron emitter in vitro.

4.2 Previous work

Historically, attempts to reduce the mean range to annihilation (R_r) of positrons in PET have primarily centered around the use of strong magnetic fields in order to confine the positrons to a reduced region nearby the source [53]. In that paper, Wirrwar et al. employed magnetic fields of up to 7 Tesla in the region of the source and concluded that a field strength of 5 Tesla was enough to reduce the positron range to approximately the inherent system resolution for both sources trialled (^{68}Ga, and ^{18}F). Noticeably, however, the experimentally measured range (FWHM) for ^{18}F was significantly larger than the simulated range at all magnetic field strengths, and did not show a trend towards a reduction in range with increased magnetic field strength.

4.3 Theory

Since production of the useful pair of 511 keV photons only occurs upon the annihilation of a positron with an electron, it is important to understand that the distance traveled by a positron from production to annihilation is dependent upon energy loss via inelastic collisions resulting in ultimate thermalisation, which is a condition necessary for positronium formation or direct annihilation. In order to increase the rate at which each positron

can lose energy, there needs to be more opportunities for the positron to interact with electrons and/or nuclei per unit distance. By immediately passing through a higher density material, the distance to thermalisation will be reduced. Such a process is effectively equivalent to implanting positrons directly from a source into a layer of material which has been adequately described by Brandt and Paulin [54] in equations 4.2 and 4.3.

$$P(x) = e^{(-\alpha x)} \tag{4.2}$$

$$\alpha \approx 17 \frac{\rho}{E_{max}^{1.4}} cm^{-1} \tag{4.3}$$

Where P is the probability of annihilation at a depth x , ρ is the material density in gcm^{-3} and E_{max} is the maximum positron energy in MeV.

Note that $1/\alpha$ represents the implantation range, which is effectively what we are trying to reduce in human tissue.

The two high density materials that were considered in this work were platinum and lead fluoride. The density of platinum is 21.45 gcm^{-3}, which, for ^{18}F means a positron implantation depth of approximately 14 μm.

However the density of Lead (II) Fluoride is $8.445 gcm^{-3}$, giving a positron implant range of approximately 37 μm. These values for platinum and lead fluoride are important for experimental design and analysis purposes.

For a positron emitter in water, Levin et al [52] suggests the use of an equation derived by Derenzo [55] as 4.4

$$P(x) = Ce^{(-k_1 x)} + (1 - C)e^{(-k_2 x)} x \geq 0 \tag{4.4}$$

Where values for $C = 0.516$ and $k_1 = 0.379 mm^{-1}$ and $k_2 = 0.031 mm^{-1}$ are appropriate for ^{18}F. This results in a $FWHM$ of 0.102 mm. It should be noted that the probability distribution function is a cusp, rather than a gaussian, and therefore $FWHM$ may not be an appropriate measure, whereas the "root mean square (rms) effective range" is often used instead. The typical rms effective range of ^{18}F in water is of the order of 0.5 mm as described in Chapter 18 of [50].

4.4 Experimental design - Platinum sandwiches

The overall objective of this initial research was to determine experimentally whether a positron emitter, sandwiched between layers of platinum of various thicknesses would result in a sharper PET image.

To that end, it was necessary to devise a method by which a positron emitter (^{18}F) could be deposited between two films of platinum coated mylar, and surrounded by a medium which could simulate human tissue.

Prior to the current research, samples of mylar had been prepared with coatings of platinum of various thickness, ranging from 0 nm (un-coated), 100 nm, 200 nm, 500 nm and 1000 nm (1 μm). The various coating thicknesses were not verified prior to experimentation. It was found by visual inspection that the coating on the 100nm sample was not particularly uniform. However the pliability and graduated opacity between the various samples indicated that the Pt thickness did increase between the samples.

Five sets (pairs) of Agarose gel slabs, moulded in petri dishes, were used as the tissue emulating medium. The agarose gel slabs were made so as to have a density similar to human muscle tissue ($1.09 gcm^{-3}$ [56]) and also provided a sufficiently firm base on which to mount the Pt coated mylar samples.

Fluorodeoxyglucose (FDG) a common radionuclide for use in PET scans since it is a glucose analogue with a bound ^{18}F atom. Since FDG is a liquid, it would spread uncontrollably if sandwiched between mylar within pads of agarose gel, so it is necessary to evaporate the solvent from the FDG prior to sandwiching, such that the solute which contains the ^{18}FDG would occupy a known limited region on the mylar. This evaporation was carried out using a heat gun. Evaporation tests were conducted using a completely decayed sample of ^{18}FDG dispensed onto mylar with no Pt coating as shown in 4.1. During this procedure the decayed ^{18}FDG was dispensed using a syringe and needle which was obtained from the hospital and would be the same needle diameter to be used during the hospital trial. This allowed for the volumetric measurement of drop size which would be important in determining the amount and hence activity to be dispensed onto the platinum coated mylar films during the hospital trial.

The final construction of each sample is shown schematically in Figure 4.2.

The planning for the experiment was undertaken using the four M plus P philosophy.

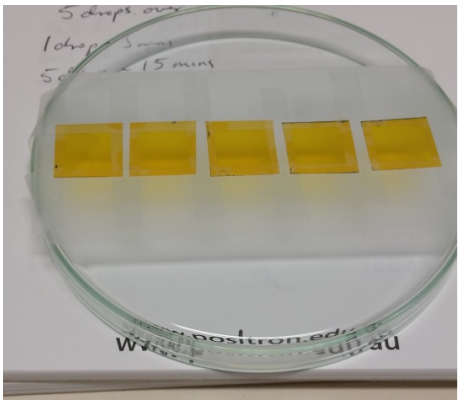

Figure 4.1: Uncoated mylar samples positioned for FDG evaporation trialling.

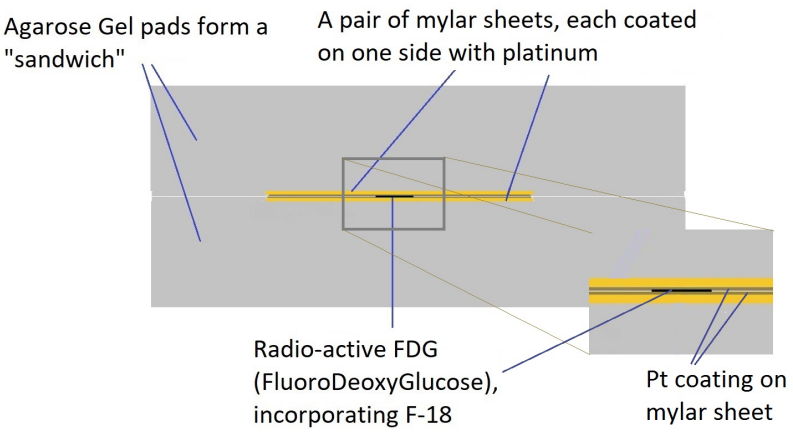

Figure 4.2: Sandwich construction showing the agarose gel pads, platinum coated mylar sheets and the positioning of the FDG in the middle.

This is a process by which the requirements are classified into one of five categories. These are: Personnel, Methods, Materials, Machinery and Measurements.

4.4.1 Personnel

These are the requirements linked to the personnel necessary to undertake the experiment. In the present case the requirement is for one person with all of the necessary skills, or two people with the skill-set divided between them. Owing to a specialised skill-set required to operate the PET scanner, two people were necessary to perform the overall experiment. While the author was primarily responsible for the sample preparation and supervision of the experiment, a qualified hospital staff member operated the PET scanner for the measurements presented in this thesis.

4.4.2 Methods

Here, the sample preparation protocol and experimental protocol are described. Since the operation of the PET scanner was performed by a qualified hospital staff member, only the sample preparation and positioning protocols are discussed here. Three drops of FDG were dispensed onto each sample (0 nm, 100 nm, 200 nm, 500 nm and 1 μ m) of metalised mylar using a shielded syringe by the hospital physicist. The determination of the activity of the deposited FDG is discussed in the *Materials* section below. All Pt thicknesses were mounted on a single petri dish lid, similar to Figure 4.1. The FDG was then evaporated using a heat-gun as discussed previously. Once evaporated, each sample was placed onto the centre of its own gel slab and the corresponding thickness sample of metalised mylar was placed on top with the metalised layer adjacent to the evaporated FDG. Finally, another gel slab was used to complete the sandwich. Each sample was placed into its own petri dish. The 5 gel - mylar - platinum - FDG - platinum - mylar - gel samples were then positioned on the scanner bed, as shown in Figure 4.3 and the PET scan was then performed. Post scan, the samples were held in the hospital hot lab until the following day to allow for the activity of the FDG to decay through approximately 10 half-lives, where-upon they were retrieved.

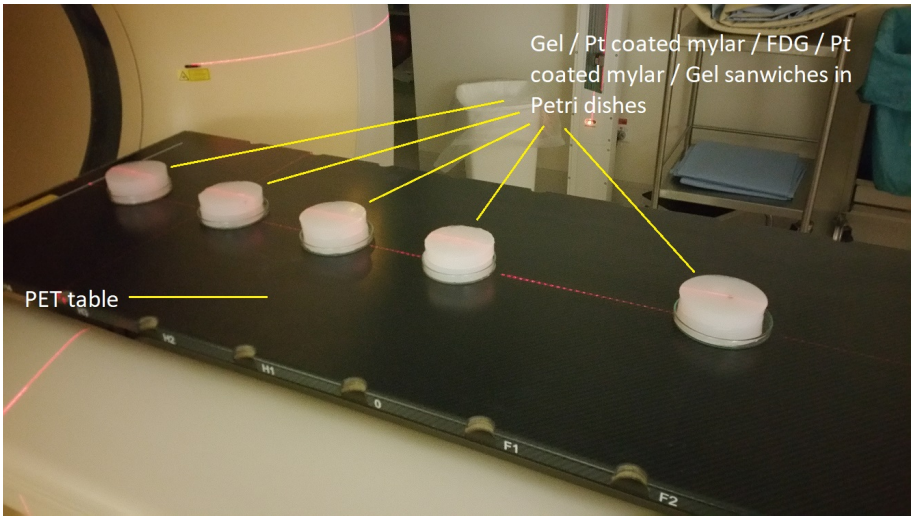

Figure 4.3: Sandwiched platinum coated mylar samples between gel pads immediately prior to the PET scan.

4.4.3 Materials

A large petri dish was used as the mold for the agarose gel pads which had a volume of 79 ml. Approximately 4 g of agarose was required, dissolved into approximately 80 ml of water to result in a density approximating human muscle tissue, which is $1.09 g/cm^{-3}$. Since there were 10 gel pads in total, 40 g of agarose and 800 ml of water were required.

On the day of the PET scan, the hospital was supplied with 1 ml of ^{18}FDG by PETNET Solutions. The ^{18}FDG had a specified activity of 0.66 GBq at 08 : 00 hrs on that day. As advised by the hospital physicist, an activity of at least 1 MBq per sandwich would produce a useable PET image for analysis. The activity of the 1 ml at 15 : 30 hrs, the time of the scan, was expected to be 38.5 MBq, based upon a half-life for ^{18}F of 109 minutes. Hence the volume of ^{18}FDG necessary to produce an activity of 1 MBq at the scan time was 0.026 ml. Based upon earlier volumetric measurements of the drop volume dispensed by the needle, that represented between one and two drops. Each drop was found to be 0.02 ml. To err on the side of caution, it was decided to dispense 0.06 ml onto each of the 5 samples. Thus, each sample had an activity of approximately 2.3 MBq. This was achieved by dispensing 3 drops onto each sample. As mentioned previously, 5 pairs of single-sided platinum coated mylar films, 15 mm x 15 mm in size were prepared.

4.4.4 Machinery

The equipment and tools required included a shielded syringe for dispensing the ^{18}FDG, heat gun for evaporating the samples, retort stand for holding the heat gun, petri dishes to carry the gel sandwiches on the PET scanner bed, a shielded workspace in which to prepare the samples, a Geiger counter to verify radioactivity and a Philips Gemini PET/CT scanner to perform the scan.

4.4.5 Measurements

Activity level of the ^{18}FDG was recorded immediately prior to the scan. The initial activity of the ^{18}FDG in the dispensing syringe prior to dispensing was 20.9 MBq. After dispensing the three drops onto each of the 5 films, the residual activity in the syringe was 7.7 MBq. Thus the activity on each film was expected to be 2.6 MBq. This activity was not directly measured since the Geiger counter in the hospital was designed for accommodating

a syringe rather than loose pieces of mylar film. The PET/CT scanner captured CT and PET images during the scan process.

4.5 Results and discussion - Platinum Sandwiches

As per the standard patient scanning operation of the Philips Gemini PET/CT scanner, four sets of image files were produced in the DICOM format. A Low Dose CT image was generated first to assist with correction for attenuation due to non-uniform tissue densities (bone, lung, muscle, organ). An example of a CT slice through one of the samples is shown in figure 4.4. Note that the petri dish is evident as well as the agarose gel pads and the sample of Pt coated mylar. The next captured image file is typically

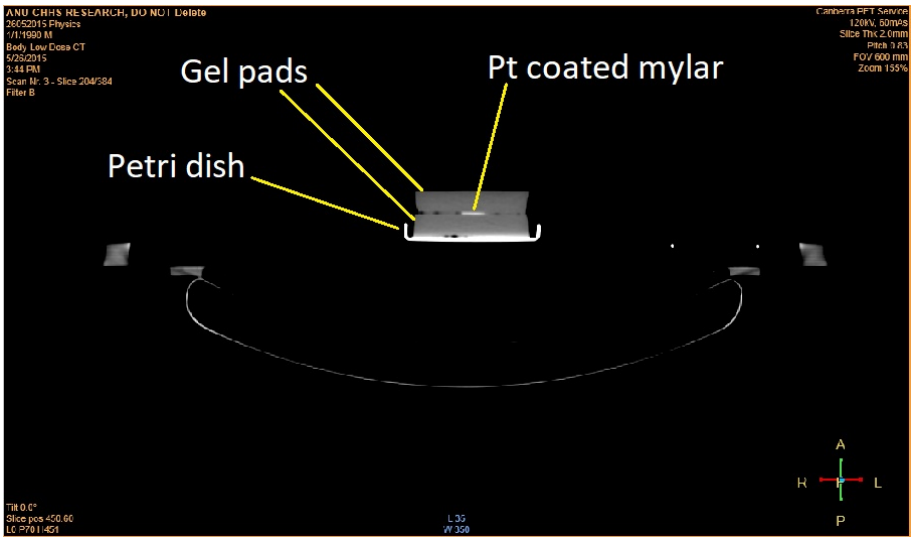

Figure 4.4: CT image of one sample on the PET bed. The change in density is evident where the platinum coated mylar is present. Also the gel pads and petri dish are visible.

called "PREVIEW", the third known as "NAC" or, non-attenuation corrected, and finally "CTAC" or CT attenuation corrected. The "PREVIEW" file is for use by the operator to determine whether any adjustments to the subject or system are required prior to taking the useful images (NAC and CTAC). The NAC image is not corrected for any attenuation due to surrounding tissue/material, in this case, the material surrounding the platinum coated mylar consists of agarose gel pads which were used to simulate muscle tissue. Since all samples are identical in terms of the agarose gel environment, and since the layers of platinum surrounding each sample are not in the plane of the image, the decision was made to use the CTAC image set for analysis and comparison purposes.

Processing and analysis of the captured DICOM files was undertaken using Matlab, a commercially available data management software suite. Matlab includes a number of functions which are useful for extracting image data and metadata from DICOM files. Three dimensional images are constructed from an ordered set of slices through the subject. In the current case, each slice has a thickness of $4mm$ and is comprised of an array of 144 x 144 pixels, each of dimension 4 mm x 4 mm. Hence, each element of each slice can be considered to be a cubic voxel of dimensions 4 mm x 4 mm x 4 mm. The content of each voxel data element is limited in magnitude to between 0 and $32767(2^{15}-1)$ due to the magnitude being stored as a 16 bit signed binary integer, although negative values are not permitted. In order to accommodate a larger range of voxel values, each slice also has associated with it, as part of the metadata, a rescale slope factor. This must be applied to the raw data in order to be able to do a direct comparison of voxel magnitude between slices. So, for example to preserve the relationship between slice A, with a rescale slope of 2 and slice B, with a rescale slope of 1, the raw data from slice A can be used directly, however the raw data from slice B must be halved in order to show the true relationship between voxel magnitudes in slice A and slice B. Hence, for each slice, the true values of voxel magnitude must be divided by the maximum rescale slope for the set and multiplied by the rescale slope of that particular slice. A potential loss in image information arises from the positioning of the source relative to the center of a voxel, remembering that each voxel provides information only about a 4 mm x 4 mm x 4 mm volume and nothing about the peak nor distribution of the source within that voxel volume. Within the realms of the stochastic nature of decay, it is reasonable to assume that positrons will radiate in an isotropic manner and therefore it ought to be appropriate to use the integral of voxels at fixed distances from the center voxel in order to identify the manner in which annihilation displacements (thermalisation path displacements) are affected by electron density in the vicinity of the decaying isotope. During the deposition of the FDG onto the various Pt coated mylar films, attention was not paid to co-location of the 3 drops. This resulted in a larger spread of radioactivity for some of the samples. Consideration was given to restricting the analysis to only the y-axis (vertical) intensity data, however after reviewing the imagery, all three axes were used in the analysis.

The data presented in Figure 4.5 represents the average 511 keV gamma-ray intensity

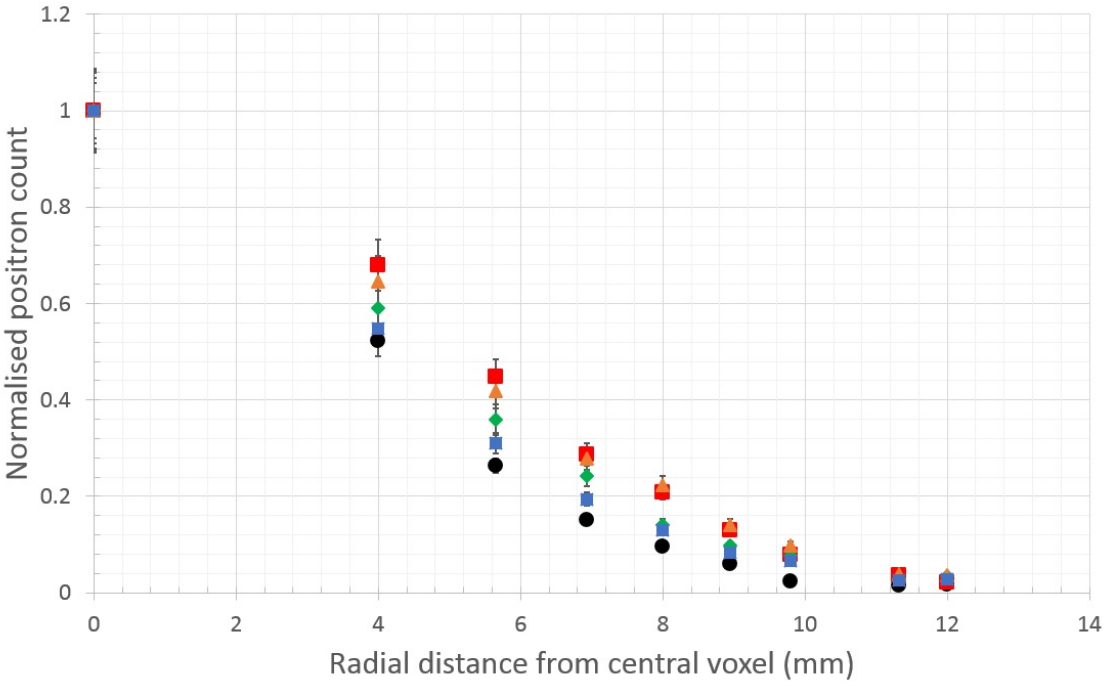

Figure 4.5: Image comparison among different thicknesses of platinum 0 nm (black circles), 100 nm (red squares), 200 nm (green diamonds), 500 nm (orange triangles) and 1000 nm (blue squares).

with distance from the center of each sample of FDG between the various thicknesses of platinum coated mylar. Vertical error bars are statistically defined by the standard error for each data point. The errors are partly the result of variation in the location of the source relative to the center of the maximum voxel which has a volume of 64 mm^3. From the graph, it appears that when a platinum coating is used, the FWHM and FWTM both increase. This is opposite to what was expected, although in hindsight, as indicated in the Theory section, a thickness of 14 μm of platinum is required in order to completely thermalise the highest energy positrons. The relatively thin layers of platinum that were used in the current experiment appear to increase the distance to thermalisation relative to no platinum at all, a phenomenon that warrants further investigation. Although this may be explained by platinum being a positron moderator, with a negative positron work function. From table 4.1, the only trend that may be worth noting is that the FWHM and FWTM distances appear to follow a pattern where they are least for an absence of platinum, increase with relatively thin layers of platinum and decrease again with a thicker layer of platinum. Note that the tabled values are across the entirety of each image, rather than half the image.

Pt Thickness (nm)	FWHM (mm)	FWTM (mm)
0	8.4 ± 1.0	15.6 ± 1.0
100	10.6 ± 1.0	19 ± 1.0
200	9.2 ± 1.0	18.0 ± 1.0
500	10.0 ± 1.0	19.6 ± 1.0
1000	8.6 ± 1.0	17.2 ± 1.0

Table 4.1: FWHM (mm) and FWTM (mm) for different platinum thicknesses.

Thus, there is no clear evidence of a resolution improvement through the introduction of the platinum layers based upon the FWHM and FWTM data, however there is evidence that there is some effect on the resolution through the inclusion of the platinum layers. Hence it was considered worthwhile to take a different approach to investigating the phenomenon.

4.6 Experimental Design - Lead colloid

In recent times, nano-science has gained prominence in many fields of Physics [57]. The use of nano-particles in physics extends to their applications in medicine. Radio-tracers attached to or embedded in nano-particles have been applied to medical imaging techniques [58]. In such cases, the nano-particles have been tagged with not only a radio-tracer, but also a bio-molecule so as to accumulate in or around the structure of interest. Such imaging systems rely upon spontaneous gamma-ray emitters such as $^{99m}Technetium$. PET imaging relies solely upon the 511 keV gamma-ray radiation produced through the annihilation of positrons with electrons. Thus, for the purposes of PET, a positron emitter must be used as the in-vivo positron source. As has been mentioned in section 4.4, ^{18}F is the isotope of choice for PET scans where tumors are involved due to its relatively short half-life, its ease of availability and the simplicity with which it can be incorporated into glucose, the food for cell respiration.

Pursuant to the tests using platinum coated mylar and FDG, the next step in investigating methods by which to limit the positron range in-vivo was to consider the formation of nano-particles comprising a heavy (i.e. electron dense) metal and a positron emitter. Consideration was given to platinum (Pt), gold (Au) and lead (Pb). Factors including cost and availability resulted in the decision to select lead as the element for this investigation. Although lead is not a bio-compatible material, it is useful in this case as a proof of princi-

ple. It was then necessary to develop a technique to manufacture a colloid which bound the lead to a positron emitting isotope. A colloid is any mixture of two phases of matter. The selected candidate for the positron emitter was ^{18}F, since that is the isotope which is used during PET, the reactants (lead nitrate and sodium fluoride) are readily available and the chemistry is reasonably accessible. Lead (II) Fluoride has a very low solubility, and hence easily forms a colloid. It was necessary to be able to make nano-particles of PbF_2 of an appropriate size of consistently less than 500 nm diameter. Note that while calculations from theory suggest sizes of around 37 μm, any nano-particles which ultimately are to travel through the bloodstream need to be less than 1 μm in diameter and as evidenced in the literature, nano-particles are typically in the region from several nanometres to 500 nm in diameter [58–61]. Several methods of PbF_2 crystal growth are described by Stubivcar et al. [62–64]. These guided the procedure developed and subsequently used which is described herein. Once the method of producing the necessary colloid was refined, it was essential to develop the protocol by which to reliably undertake the trial at The Canberra Hospital, since the colloid needed to be produced on-site. The protocol thus developed is also described herein.

4.6.1 Colloid chemistry

As mentioned in section 4.6, the reactants used to produce the Lead Fluoride colloid were Sodium Fluoride (NaF) and Lead Nitrate ($Pb(NO_3)_2$), according to the following chemical equation:

$$2NaF(aq) + Pb(NO_3)_2(aq) => PbF_2(s) + 2NaNO_3(aq)$$

Factors which affect the size and shape of the colloidal (PbF_2) crystals include the following: a) reactant concentration, b) reactant balance (i.e. excess of one over the other), c) temperature, d) reactant mixing strategy and e) time. Several methods were trialled until one was discovered which provided the desired size and uniformity of PbF_2 nano-particles. The electron micrographs below in Figures 4.6 and 4.7 show the outcomes of the two most promising methods, including the method which was ultimately chosen (Figure 4.6) for use in a trial run and the final experiment. A trial run was performed at TCH with inactive

Sodium Fluoride ($Na^{19}F$) to ensure that the facilities at the hospital radiation lab would be adequate for the chemistry that was required.

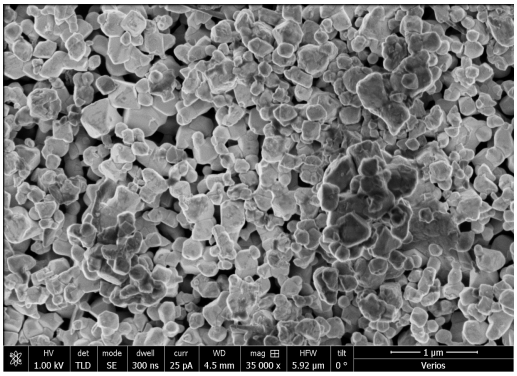

(a) 4 ml NaF poured into 2 ml$Pb(NO_3)_2$ and stirred, producing 50 nm to 500 nm PbF_2 crystals.

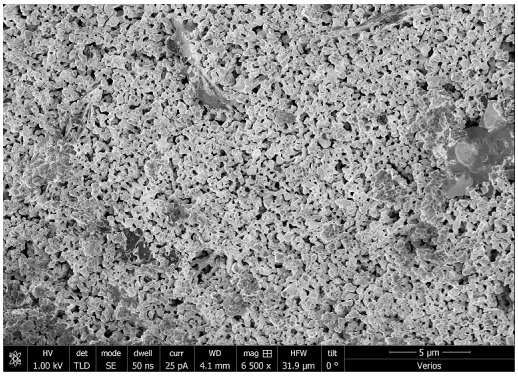

(b) 4 ml NaF poured into 4 ml$Pb(NO_3)_2$ and stirred, producing 50 nm to 500 nm PbF_2 crystals with occasional larger sheets.

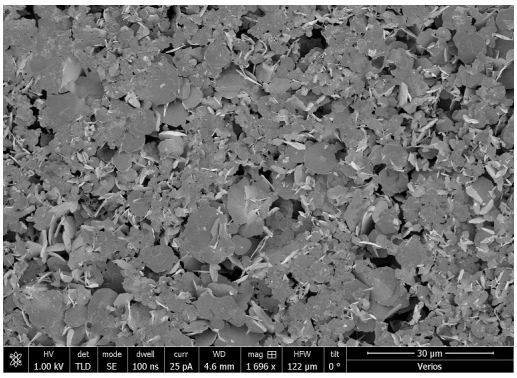

(c) 4 ml NaF poured into 10 ml$Pb(NO_3)_2$ and stirred, producing a mixture of sheets of mainly PbF_2 sheets in the 10 μm range with occasional crystals.

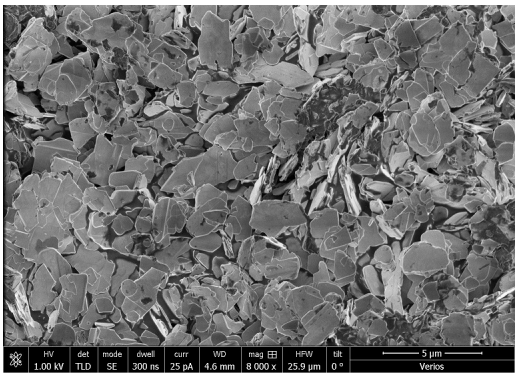

(d) 4 ml NaF poured into 20 ml$Pb(NO_3)_2$ and stirred, producing PbF_2 sheets in the 5 μm range with very few crystals evident.

Figure 4.6: Mixing by pouring 0.2 MNaF into 0.1 M$Pb(NO_3)_2$ and immediately stirring.

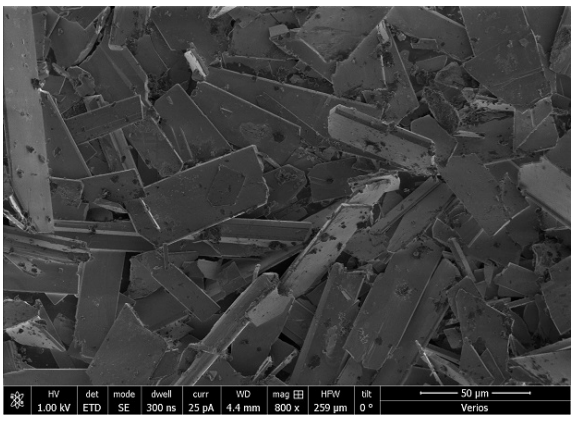

(a) 0.1M NaF added to 0.05 M $Pb(NO_3)_2$ without stirring.

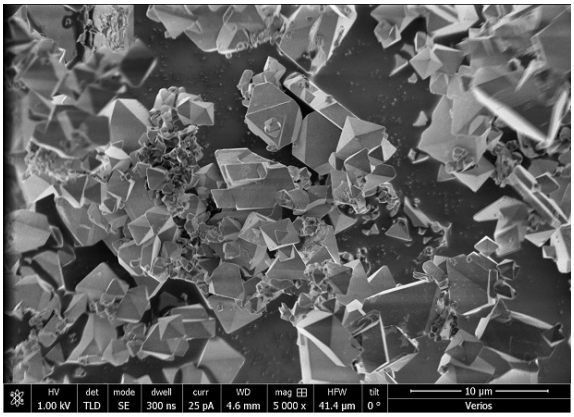

(b) 0.04 M NaF added to 0.02 M $Pb(NO_3)_2$ without stirring.

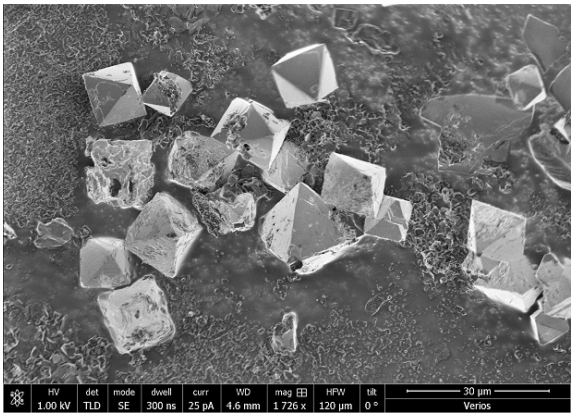

(c) 0.02 M NaF added to 0.01 M $Pb(NO_3)_2$ without stirring.

Figure 4.7: Mixing by slowly adding NaF into $Pb(NO_3)_2$ without stirring.

Colloid production procedures which were tried included fast and slow mixing strategies, mixing the $Pb(NO_3)_2$ into the NaF, mixing the NaF into the $Pb(NO_3)_2$, as well as trying a variety of different initial concentrations of NaF and $Pb(NO_3)_2$. It is evident that the growth of sheets of PbF_2 occurred both when mixing was slow and when there was an excess of $Pb(NO_3)_2$ over NaF. The results of the most successful method are shown in figures 4.6a and 4.6b. Ultimately the method shown in figure 4.6b was implemented as described in figure 4.11. Once the chemistry had been refined, it was then necessary to devise a suitable experimental regime by which a PET scan could provide images which could then be analysed to determine whether there was any basis for the hypothesis that a metallic colloid reduces the positron range and thereby improves the clarity of PET images.

The micrographs in figure 4.8 show the SEM images of the filtered PbF_2 taken from the remainder of the sample which was prepared at the hospital hotlab. This remainder was filtered immediately, so as to inhibit further crystal growth.

From figures 4.8a and 4.8b, it can be seen that the PbF_2 crystals were found to be in the range from approximately 10 nm to 500 nm in diameter, with a quite regular distribution of sizes within this range. This was the target for the present experiment. While uniformity of nano-particle size was not a primary goal, it was important to ensure that nano-particle growth did not exceed around 500 nm so that they did not settle out of the colloid prior to the completion of the scan. A homogeneous distribution of the nano-particles within the sample holder ensured that the scan images were not skewed in any way due to settling of the PbF_2 nano-particles.

The equipment available at The Canberra Hospital included a National Electrical Manufacturers Association (NEMA) Data Spectrum Corporation (DSC) Flanged Jaszczak cylindrical water phantom into which spherical sample holders (see figure 4.10) could be mounted as shown in figure 4.9 The phantom is a 21.6 cm internal diameter by 18.6 cm internal height hollow cylindrical perspex chamber into which can be mounted either solid perspex spheres of various diameters or hollow perspex spheres of various diameters into which positron source material can be loaded.

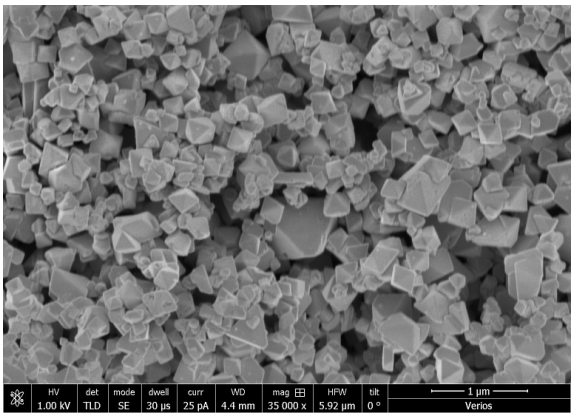

(a) SEM of the first sample taken from remaining filtered crystals.

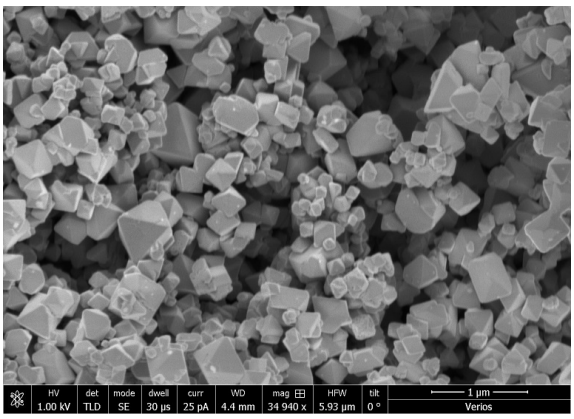

(b) SEM of the second sample, also taken from the remaining filtered crystals.

Figure 4.8: SEM of PbF_2 filtered crystals used in the hospital experiment.

4.6.2 Experimental procedure

Two hollow spheres of the same internal diameter were not available, so the two samples were loaded into different sized spheres, 6 mm internal diameter and 8 mm internal diameter. In order to meet the requirement for a target sample activity in the vicinity of 1 MBq to 5 MBq as advised by the hospital physicist, as well as a PbF_2 concentration sufficient to precipitate into suitable sized crystals, it was necessary to combine the radioactive $Na^{18}F$ with stable $Na^{19}F$. On the day of the experiment, the activity of the $Na^{18}F$ sample was 125 MBq at 3.30pm, and the volume was 1 ml. The concentration of $Na^{18}F$ can be calculated using the following formula:

$$N = \frac{At_{\frac{1}{2}}}{ln2} \tag{4.5}$$

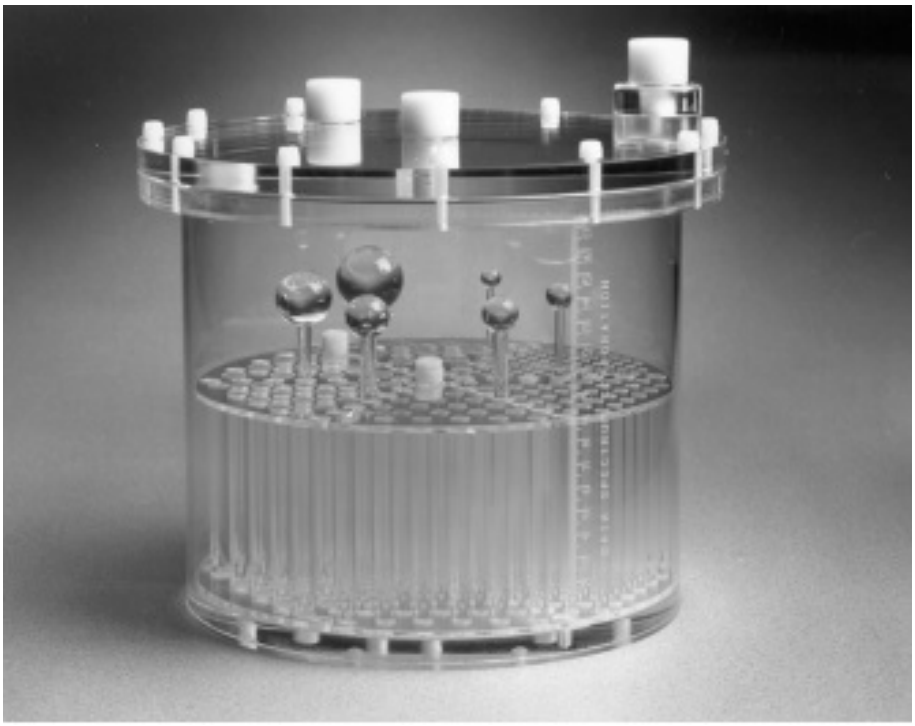

Figure 4.9: DSC NEMA Phantom.

Where:

N is the number of $Na^{18}F$ molecules present in the volume, A is the current activity in Bq and $t_{\frac{1}{2}}$ is the half-life of ^{18}F

Thus the concentration of $Na^{18}F$ was approximately 2x10^{-9} M. Now, from the experiments conducted to determine the suitable concentrations of NaF and $Pb(NO_3)_2$ for colloid production, a $Na^{18}F$ concentration of 0.1 M was found to be necessary and therefore the $Na^{18}F$ concentration needed to be increased by combining the $Na^{18}F$ with its stable variant, $Na^{19}F$. This is further explained below and in figure 4.11.

A target comprised of $Na^{18}F$ solution was used as a standard for comparison with a $Pb^{18}F_2$ colloid. The procedure followed in producing the target $Na^{18}F$ solution and target $Pb^{18}F_2$ colloid for filling the spherical sample holders is outlined in Figure 4.11 and is described below.

Thus the sample of $Na^{18}F$, which was obtained by the hospital for this experiment, had to be divided into one portion which would be used in the sample holder for the pure $Na^{18}F$, and another portion used to generate the $Pb^{18}F_2$ colloid. The concentration of NaF required in order to create the appropriate sized nano-particles of $Pb^{18}F_2$ had previously been found to be 0.1 M. Given that the concentration of the $Na^{18}F$ was so low,

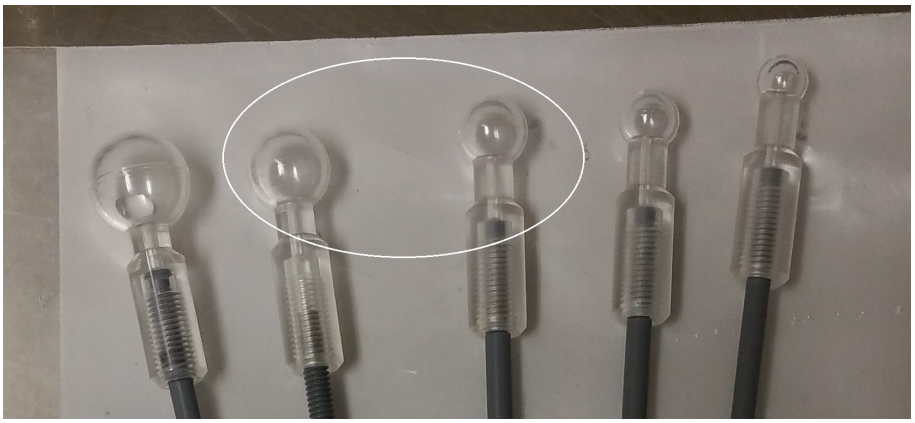

Figure 4.10: Micro-hollow spheres for use with the DSC NEMA Phantom. Circled spheres are those which were used.

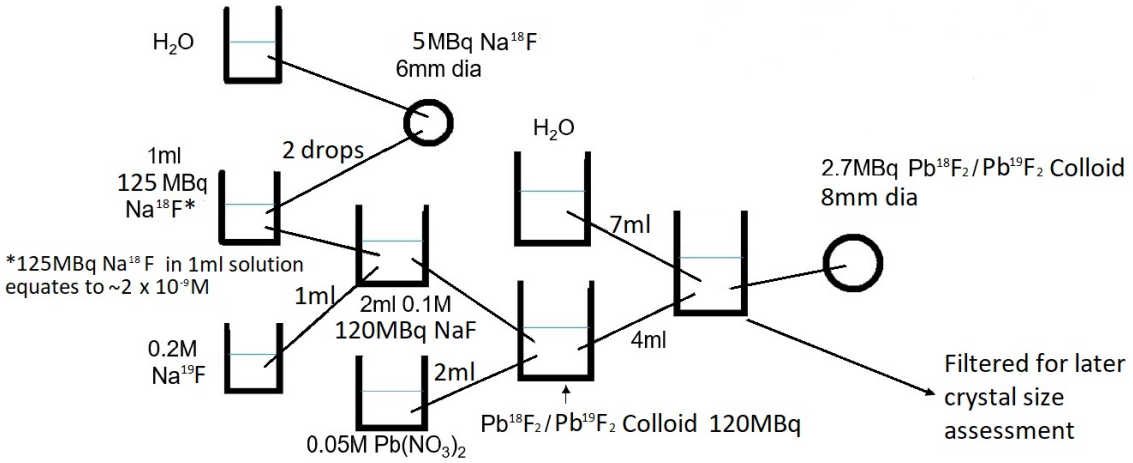

Figure 4.11: Hospital Radiation Lab Chemistry.

it was decided to decant 2 drops (as per the previous Platinum experiment, Section 4.4 sub-section Materials, one drop was determined to be 0.02 ml) of the $Na^{18}F$ for use in the $6mm$ diameter sample holder to which was added sufficient deionised water to fill it. The volume of the 6 mm diameter sphere was 0.11 ml. The remaining $Na^{18}F$ was combined with approximately 1 ml of 0.2 M $Na^{19}F$, to produce 2 ml of 0.1 M $Na^{18/19}F$. This was then mixed and briefly stirred with 2 ml of 0.05 M $Pb(NO_3)_2$to produce 4 ml of solution containing PbF_2 colloid. In order for the sample to have an activity in the vicinity of 1 MBq to 5 MBq, 7 ml of de-ionised water was added to the colloid to form 11 ml of colloid, from which 0.27 ml was used to fill the 8 mm diameter sample holder.

The remainder of the colloid was subsequently filtered so that the particle size could be determined accurately using SEM at a later time. Assay of the PbF_2 crystals produced during the final experiment indicated that a suitable nano-particle size and uniformity had

been achieved (see figure 4.8).

The final activity of the colloid in the 8 mm diameter sample holder was 2.46 MBq and the final activity of the $Na^{18}F$ in the 6 mm diameter sample holder was 4.81 MBq. These activities were measured at 3 : 30pm. The scans were carried out at approximately 4 : 30pm. Such a difference in activity levels is not significant, since the Philips Gemini Gen3 machine is able to accommodate quite large variations in intensity. This has previously been explained in Section 4.5 through the use of the rescale slope factor.

Once the sample holders were filled with the requisite chemical (NaF for the 6 mm dia sphere and PbF_2 for the 8 mm dia sphere), the sample holders were affixed inside the phantom and the phantom was filled with water (see Figure 4.12). The colloid can clearly be seen in the sample holder to the right, and the transparent $Na^{18}F$ can be seen in the sample holder to the left. The adjacent QR code will allow the reader to view a portion of the phantom loading process. The url for the same video is `https://www.youtube.com/watch?v=y0zzyEgfCFA`

Phantom Load

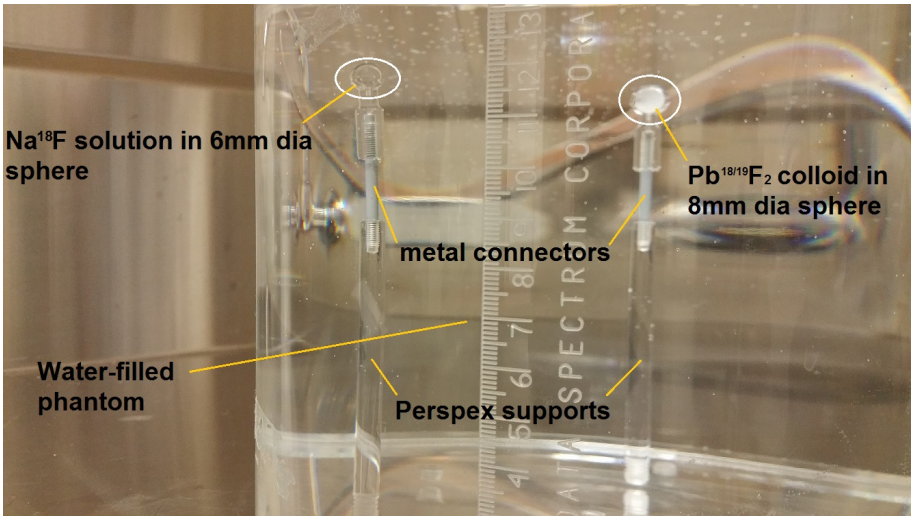

Figure 4.12: NaF and PbF_2 samples inside the Phantom

The phantom was then positioned on the scanner bed and held in position using tape (see Figures 4.13a and 4.13b and 4.14).

(a) Right eye view. (b) Left eye view.

Figure 4.13: Phantom positioned on scanner bed. Note that a three-dimensional view may be achieved by visually merging the right and left image (i.e by the reader crossing their eyes).

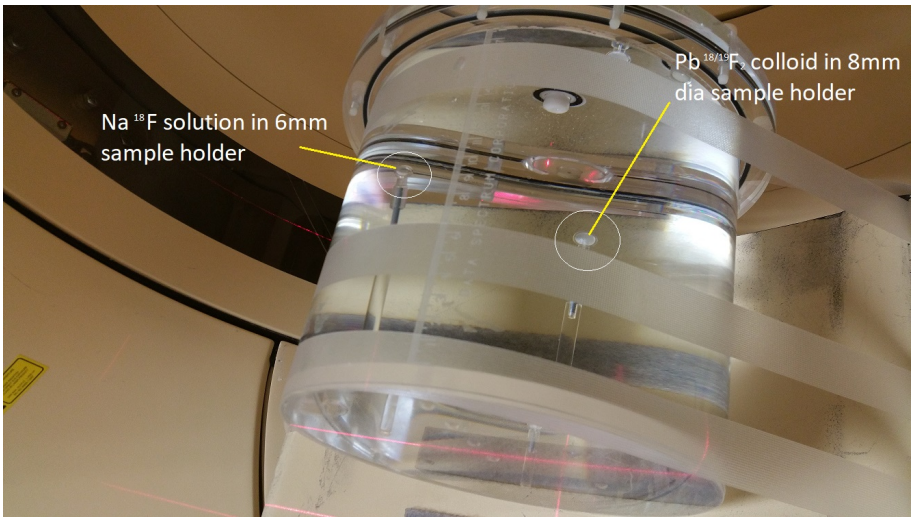

Figure 4.14: Phantom on the PET scanner bed.

4.7 Results and discussion - Lead colloid

Since the Philips Gemini output file format has been discussed in section 4.5, only the analysis will be discussed here. Of interest was the apparent target size in the PET images for the two samples. As mentioned, unfortunately two sample spheres of the same internal diameter were not available for the trial, therefore complicating a direct comparison between the two source PET images.

Figure 4.15 shows the CT scan images for the two samples within the phantom. The CTAC image files were selected for analysis. The rescale slope factor described in the earlier section allows a wide variation in activity levels to be accommodated. Whereas for the case of the platinum sandwiches (see section 4.5) only voxels along the x, y and z axes were used in the analysis (at distances of 0, 4, 8, 12 and 16 mm from the peak voxel), in the case of the colloid experiment, all voxels at a distance of up to and including 12 mm

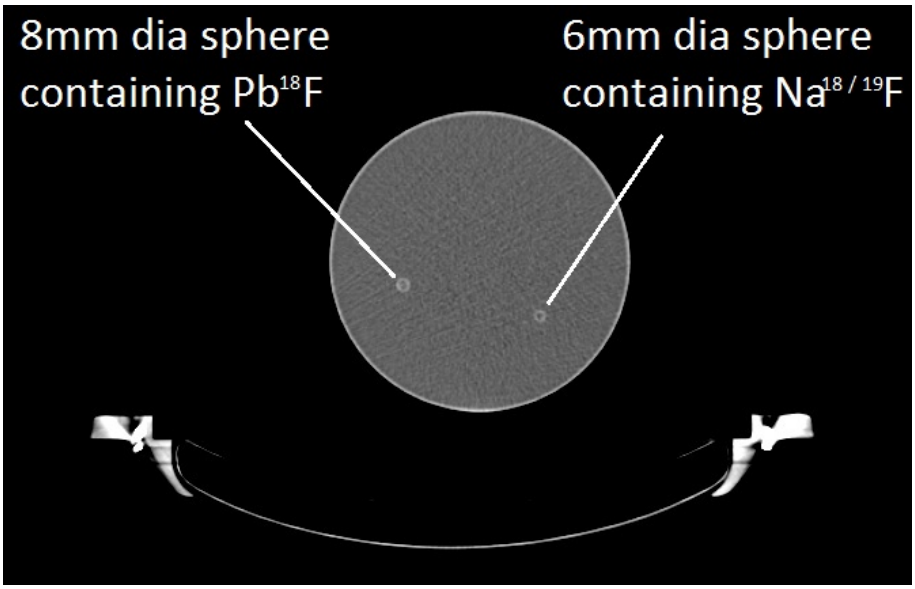

Figure 4.15: CT scan of the phantom showing the two samples.

were used in the analysis. This was achieved by assigning an (X, Y, Z) co-ordinate to each voxel and averaging the intensity of voxels equidistant from the peak voxel and reporting the standard error as the statistical uncertainty. The measurement at each distance was then normalised to the total count (i.e. the integral of intensities out to 12 mm). Figure 4.16 shows the image analysis results, comparing the $8mm$ diameter PbF_2 source and the 6 mm diameter NaF source. The lines are provided as a guide to the eye.

There appears to be very little difference in intensity distribution between the images to a radial distance of 12 mm. It was anticipated that there would have been clear distinguishing features, given that the diameters of the two sources were 6 mm for the NaF and 8 mm for the PbF_2. The indication that an 8 mm PbF_2 target could appear virtually the same as a 6 mm NaF target was encouraging from the perspective of the stated hypothesis. However, since another explanation could relate to the system resolution, it was decided to undertake a subsequent experiment on another day, where both target sizes would contain the same radio-tracer. Due to the availability of FDG, this was used in both the 6 mm and 8 mm sample holders during this subsequent scan . Once again, hospital staff operated the Gemini 3 scanner.

Processing of the data and analysis of the image produced followed the same strategy as mentioned above. Figure 4.17 shows the comparison between the the 6 mm diameter FDG target and the 8 mm diameter FDG target.

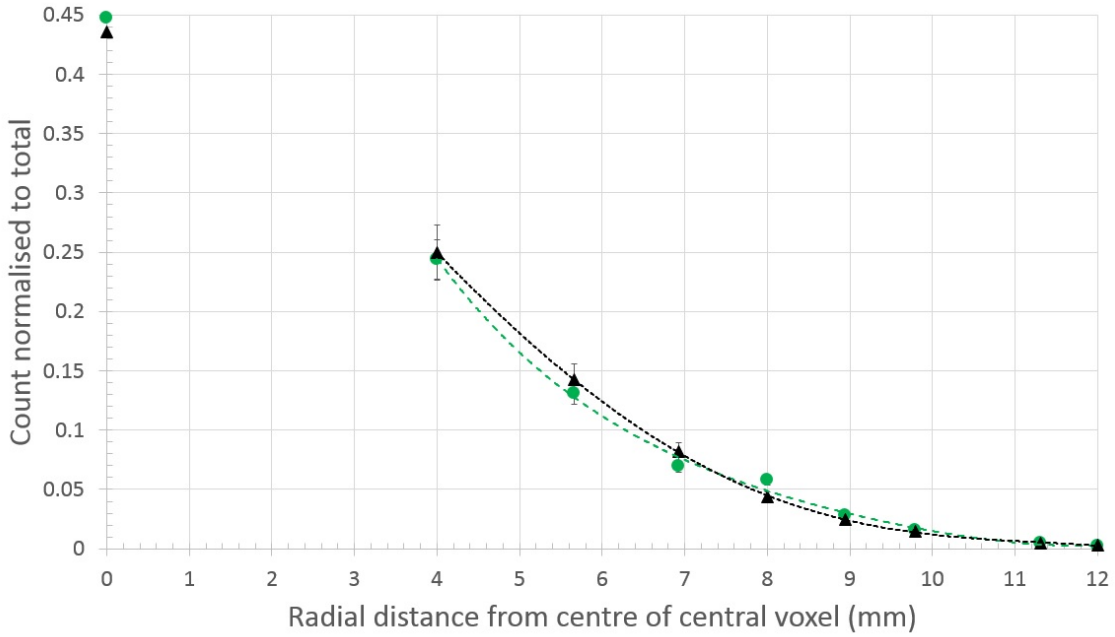

Figure 4.16: Comparison of 8 mm dia PbF_2 (black triangles) and 6 mm dia NaF (green circles).

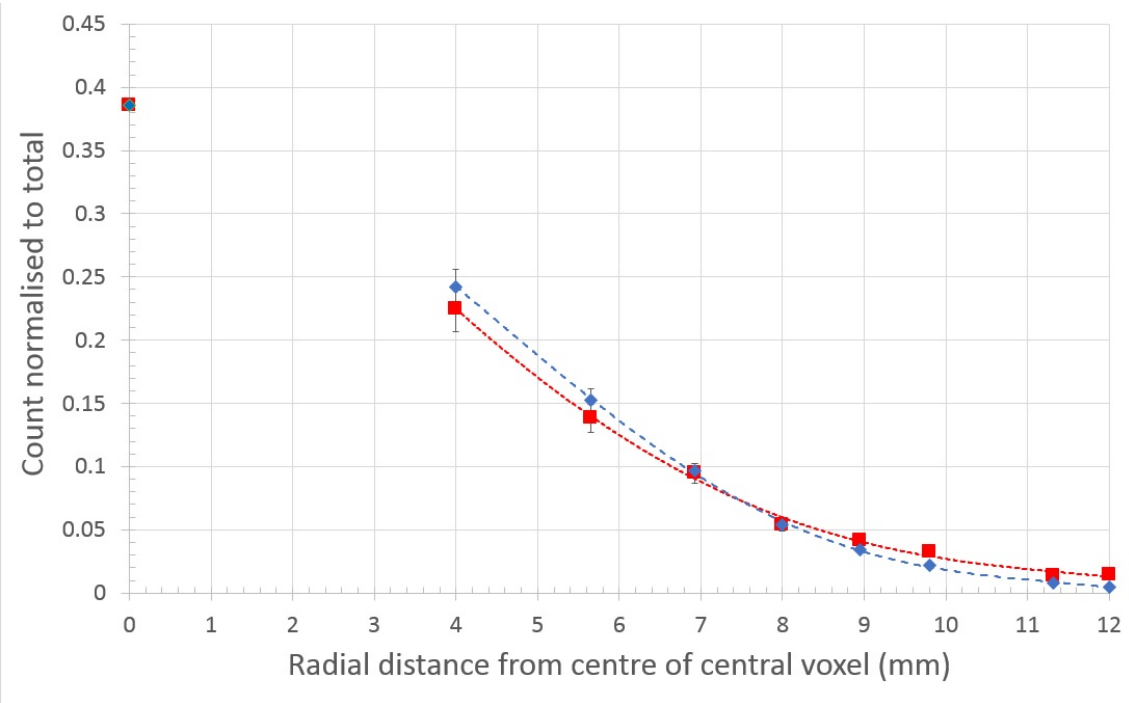

Figure 4.17: Comparison of 8 mm dia FDG (red squares) and 6 mm dia FDG (blue diamonds).

In comparing figures 4.16 and 4.17, a couple of attributes become apparent. While in both experiments, there is a cross-over between the 6 mm and 8 mm sample intensities at a radial distance of around 7.5 mm, in the case of the NaF / PbF_2 experiment, the cross-over is opposite compared to the FDG / FDG experiment. Although the uncertainties involved mean that this is purely a qualitative observation. More importantly, in the comparison between the 6 mm NaF image and the 6 mm FDG image, as seen in figure 4.18, the 8 mm PbF_2 data lies either between the two 6 mm diameter NaF and FDG samples, or below them (beyond about 7.5 mm). However, once again, the uncertainties dictate purely a qualitative assessment.

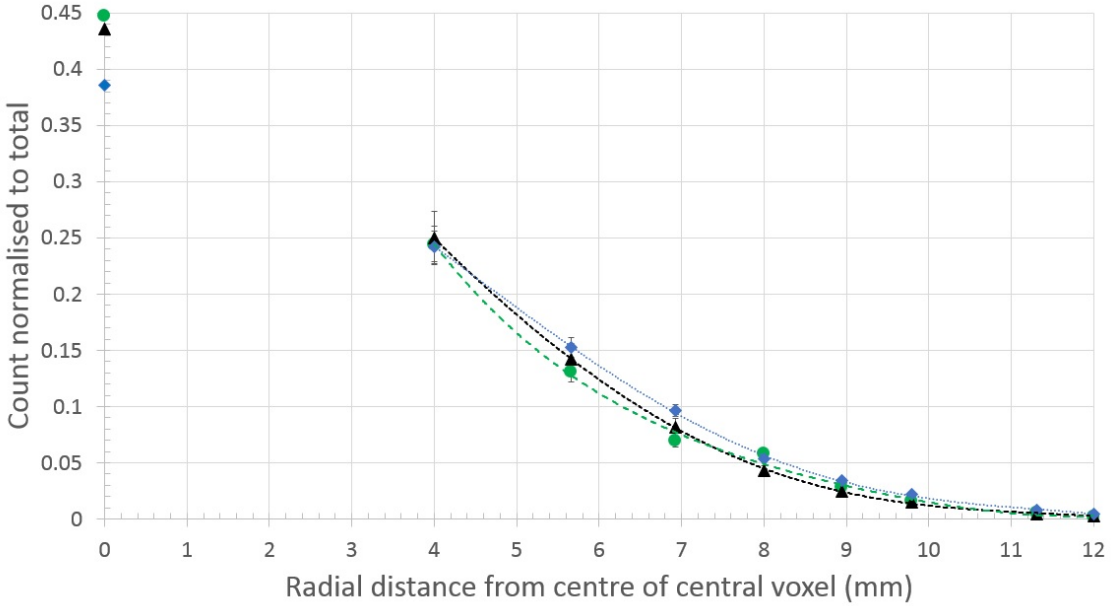

Figure 4.18: Comparison of 6 mm dia NaF (green circles), 6 mm dia FDG (blue diamonds) and 8 mm dia PbF_2 (black triangles).

Most important of all is the comparison between the images of the 8 mm diameter PbF_2 and the 8 mm diameter FDG sources. This comparison is presented in figure 4.19.

The picture now becomes somewhat clearer. The PbF_2 data shows a relatively higher central peak intensity and a considerably smaller FWTM than the FDG data.

As summarised in table 4.2, within the experimental uncertainties, there appears to be very little difference in the FWHM between FDG and the PbF_2 colloid of the same dimensions. However there is good evidence that the FWTM for the PbF_2 colloid (18.0 $\pm$1.0 mm) is considerably better than that for FDG (21.8 $\pm$1.0 mm). This is a very encouraging result and indicates that there has indeed been an increase in annihilation,

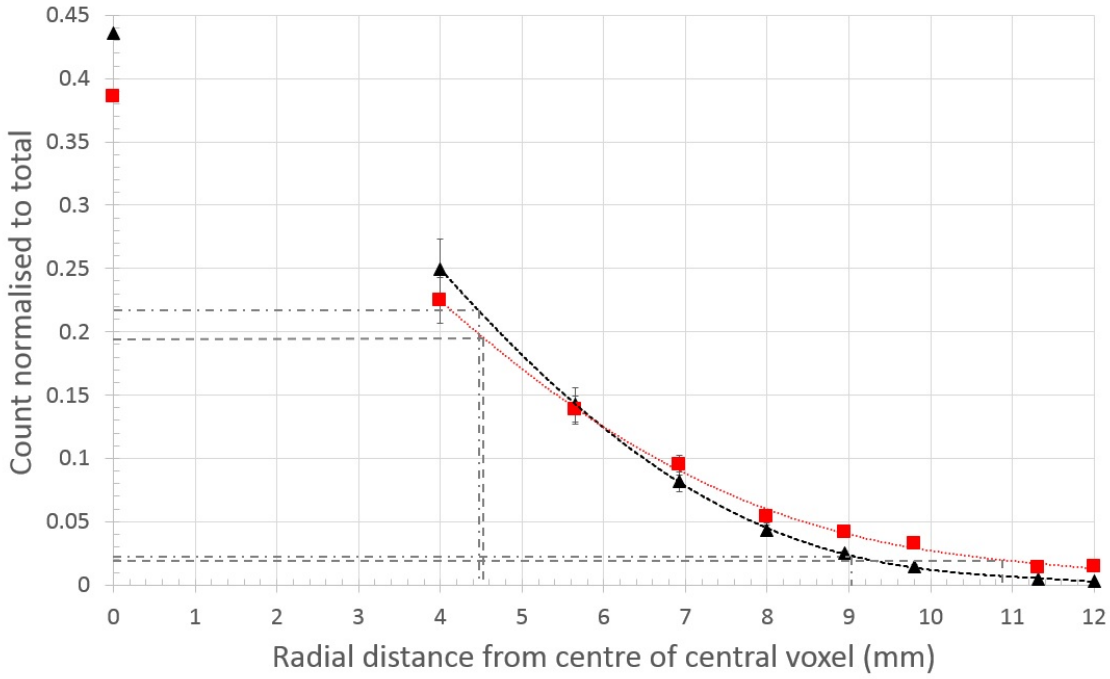

Figure 4.19: Comparison of 8 mm dia FDG (red squares) and 8 mm dia PbF_2 (black triangles). FWHM / FWTM FDG (horizontal dashed lines), FWHM / FWTM PbF_2 (horizontal dot-dash lines).

either direct or via positronium formation, within the central voxel through the use of a lead colloid. It should be noted that while figure 4.19 represents the radial FWHM and FWTM, table 4.2 shows the FWHM and FWTM for each entire image. Valuable information would be obtained by performing the same experiment using a small animal PET machine, where the voxel volume is in the vicinity of 1 mm^3 to 4 mm^3.

Source (8mm dia)	FWHM (mm)	FWTM (mm)
FDG	9.2 ± 1.0	21.8 ± 1.0
PbF_2	8.8 ± 1.0	18.0 ± 1.0

Table 4.2: FWHM (mm) and FWTM (mm) data for PbF_2 colloid and FDG both in 8 mm dia holders.

4.8 Future work

While the above results are encouraging, there is certainly scope for testing the hypothesis using higher resolution PET systems such as small animal PET machines, which have a voxel size of the order of 1 mm^3 due primarily to the smaller detector crystal size and a reduction in gamma-ray path length, thereby reducing the gamma-ray non-collinearity

effects. As mentioned earlier, lead (Pb) was only chosen for the current research for convenience. If it is clearly demonstrated that colloid use is a viable methodology, either a biologically inert compound is required as the electron dense material or total encapsulation in a biologically inert material is necessary. Unless encapsulated, caution is advised when selecting appropriate compounds, since there are few that have little or no biological side-effects as reported by Nel et al. [65]. Potential candidates may include gold and silver, however each of these raises cytotoxicity issues as reported by Nel et al. Platinum is perhaps a better candidate as is bismuth (Bi). Bi has been reported by Keogan et al. as having no adverse biological effects and therefore may be the most suitable candidate. [66] Bismuth (III) Fluoride has a very low solubility in water and therefore should be producible as a colloid. BiF_3 is cytotoxic, so further encapsulation within a bio-structure prior to introduction into a patient would be necessary. Future investigation of this option is highly recommended. In terms of candidates for positron emission, ^{68}Ga, with a half-life of 68.3 min and a maximum positron energy of 1.9 MeV is a candidate. The larger maximum energy for ^{68}Ga would provide a better opportunity to see positron range reduction, even in a Whole Body PET/CT machine. The current research did not consider encapsulation techniques, nor bio-compatibility, both of which would warrant investigation in further research.

Chapter 5

Conclusion

The research described herein has taken three separate approaches towards increasing knowledge of the interaction between antimatter (positrons) and biologically relevant matter.

5.1 Positron and electron scattering from biomolecules

The measurements of various electron and positron scattering cross-sections for thymine and pyridine were presented. The difficulties experienced with thymine resulted in data which had a larger than desired uncertainty. An established technique to normalise the measured data with theory at higher energies resulted in reasonable agreement with the available calculations. Further work can be done to measure thymine differential cross-sections. Pyridine was less troublesome with differential scattering cross-sections being included in the measurement set and the results were in quite close agreement with available calculations. The Pyridine positron and electron data is being added to the library of cross-sections already established by the positron group. Further positron scattering cross-section data for other biologically significant molecules will continue to be measured by the group, and it is anticipated that thymine will be revisited in the future.

5.2 Liquid target holder

Since water is the most prolific molecule in the human body, it has been important to be able to devise a mechanism to test predictions of positron transport in water in its liquid phase as well as to give a basis for refining the accuracy of models before they are extended in a realistic manner to include more and more biologically relevant molecules. The current research has taken a substantial step towards the design and implementation of such a

mechanism. A suitable structure for a target bath of liquid water has been designed and demonstrated. Further refinement is left for later researchers to undertake, with the ultimate goal to be possible incorporation into the AIST ex-vacuo positron beamline and/or the ANU in-vacuo positron beamlines.

5.3 Positron Emission Tomography (PET) image enhancement

Factors affecting the resolution of PET images have been well-known for some time. One such factor is the positron path displacement to annihilation. Until now, the positron path displacement has been determined purely by the initial positron energy, which is a characteristic of the isotope. Apart from the useful biological chemistry that ^{18}F provides, it also decays with a relatively low energy positron emission giving a resultant mean path displacement to annihilation in the millimeter range, which has made it the isotope of choice for PET . The current study adopted a novel approach of binding the positron emitter to a heavy metal in a colloidal solution to determine whether the resultant increase in electron density in the vicinity of the positron emitter can give an even shorter displacement to annihilation, and hence resulting in an enhancement to the signal nearer to the emission site. The findings were influenced by the voxel size which is a characteristic of the PET scanner used. There are strong indications that the positron path length had been affected and reduced. In particular the FWTM displacement shows a significant reduction. Further work needs to be carried out using a PET machine with sub-millimeter voxel size, such as a small animal PET scanner.

Whilst the current research has addressed many of the questions asked of it, there is still much more to be done in such a vital area of health research, including the extension of this idea into a system that will be bio-compatible.

Bibliography

[1] P. Możejko and L. Sanche, "Cross section calculations for electron scattering from dna and rna bases," *Radiation and environmental biophysics*, vol. 42, no. 3, pp. 201–211, 2003.

[2] M. L. McDermott, H. Vanselous, S. A. Corcelli, and P. B. Petersen, "Dnas chiral spine of hydration," *ACS central science*, vol. 3, no. 7, pp. 708–714, 2017.

[3] A. B. de Gonzalez and S. Darby, "Risk of cancer from diagnostic x-rays: estimates for the uk and 14 other countries," *The lancet*, vol. 363, no. 9406, pp. 345–351, 2004.

[4] B. S. Pyenson, C. I. Henschke, D. F. Yankelevitz, R. Yip, and E. Dec, "Offering lung cancer screening to high-risk medicare beneficiaries saves lives and is cost-effective: an actuarial analysis," *American health & drug benefits*, vol. 7, no. 5, p. 272, 2014.

[5] I. U. P. on Breast Cancer Screening *et al.*, "The benefits and harms of breast cancer screening: an independent review," *The Lancet*, vol. 380, no. 9855, pp. 1778–1786, 2012.

[6] D. J. Brenner and E. J. Hall, "Computed tomographyan increasing source of radiation exposure," *N Engl J Med*, vol. 357, pp. 2277–84, 2007.

[7] B. Boudaıffa, P. Cloutier, D. Hunting, M. A. Huels, and L. Sanche, "Resonant formation of dna strand breaks by low-energy (3 to 20 ev) electrons," *Science*, vol. 287, no. 5458, pp. 1658–1660, 2000.

[8] R. M. Moadel, R. H. Weldon, E. B. Katz, P. Lu, J. Mani, M. Stahl, M. D. Blaufox, R. G. Pestell, M. J. Charron, and E. Dadachova, "Positherapy: targeted nuclear therapy of breast cancer with 18f-2-deoxy-2-fluoro-d-glucose," *Cancer research*, vol. 65, no. 3, pp. 698–702, 2005.

[9] E. Anderson, R. Boadle, J. Machacek, L. Chiari, C. Makochekanwa, S. Buckman, M. Brunger, G. García, F. Blanco, O. Ingolfsson, *et al.*, "Low energy positron in-

teractions with uraciltotal scattering, positronium formation, and differential elastic scattering cross sections," *The Journal of chemical physics*, vol. 141, no. 3, p. 034306, 2014.

[10] P. Palihawadana, R. Boadle, L. Chiari, E. Anderson, J. Machacek, M. J. Brunger, S. Buckman, and J. Sullivan, "Positron scattering from pyrimidine," *Physical Review A*, vol. 88, no. 1, p. 012717, 2013.

[11] W. Tattersall, L. Chiari, J. Machacek, E. Anderson, R. D. White, M. Brunger, S. J. Buckman, G. Garcia, F. Blanco, and J. P. Sullivan, "Positron interactions with water–total elastic, total inelastic, and elastic differential cross section measurements," *The Journal of chemical physics*, vol. 140, no. 4, p. 044320, 2014.

[12] L. Chiari, E. Anderson, W. Tattersall, J. R. Machacek, P. Palihawadana, C. Makochekanwa, J. P. Sullivan, G. García, F. Blanco, R. P. McEachran, *et al.*, "Total, elastic, and inelastic cross sections for positron and electron collisions with tetrahydrofuran," *The Journal of Chemical Physics*, vol. 138, no. 7, p. 074301, 2013.

[13] N. Oshima, B. E. O'Rourke, R. Kuroda, R. Suzuki, H. Watanabe, S. Kubota, K. Tenjinbayashi, A. Uedono, and N. Hayashizaki, "Slow positron beam apparatus for surface and subsurface analysis of samples in air," *Applied physics express*, vol. 4, no. 6, p. 066701, 2011.

[14] J. Sullivan, A. Jones, P. Caradonna, C. Makochekanwa, and S. Buckman, "A positron trap and beam apparatus for atomic and molecular scattering experiments," *Review of Scientific Instruments*, vol. 79, no. 11, p. 113105, 2008.

[15] A. P. Mills Jr and E. Gullikson, "Solid neon moderator for producing slow positrons," *Applied Physics Letters*, vol. 49, no. 17, pp. 1121–1123, 1986.

[16] P. J. Schultz and K. G. Lynn, "Interaction of positron beams with surfaces, thin films, and interfaces," *Reviews of Modern Physics*, vol. 60, no. 3, p. 701, 1988.

[17] T. Murphy and C. Surko, "Positron trapping in an electrostatic well by inelastic collisions with nitrogen molecules," *Physical Review A*, vol. 46, no. 9, p. 5696, 1992.

[18] S. Gilbert, J. Sullivan, R. Greaves, and C. Surko, "Low-energy positron scattering from atoms and molecules using positron accumulation techniques," *Nuclear Instruments and Methods in Physics Research Section B: Beam Interactions with Materials and Atoms*, vol. 171, no. 1, pp. 81–95, 2000.

[19] J. P. Sullivan, S. J. Gilbert, J. P. Marler, R. Greaves, S. Buckman, and C. M. Surko, "Positron scattering from atoms and molecules using a magnetized beam," *Physical Review A*, vol. 66, no. 4, p. 042708, 2002.

[20] I. Iga, I. Sanches, E. de Almeida, R. Sugohara, L. Rosani, and M.-T. Lee, "Experimental verification on the applicability of the independent-atom model (iam) for elastic electron-molecule scattering in the intermediate-energy range," *Journal of electron spectroscopy and related phenomena*, vol. 155, no. 1-3, pp. 7–13, 2007.

[21] F. Blanco, L. Ellis-Gibbings, and G. García, "Screening corrections for the interference contributions to the electron and positron scattering cross sections from polyatomic molecules," *Chemical Physics Letters*, vol. 645, pp. 71–75, 2016.

[22] J. Tennyson, "Electron–molecule collision calculations using the r-matrix method," *Physics Reports*, vol. 491, no. 2-3, pp. 29–76, 2010.

[23] J. Tennyson, "Low-energy, elastic positron-molecule collisions using the r-matrix method: e+-he2 and e+-n2," *Journal of Physics B: Atomic and Molecular Physics*, vol. 19, no. 24, p. 4255, 1986.

[24] M. A. Lima, L. M. Brescansin, A. J. da Silva, C. Winstead, and V. McKoy, "Applications of the schwinger multichannel method to electron-molecule collisions," *Physical Review A*, vol. 41, no. 1, p. 327, 1990.

[25] J. S. Germano and M. A. Lima, "Schwinger multichannel method for positron-molecule scattering," *Physical Review A*, vol. 47, no. 5, p. 3976, 1993.

[26] D. Ferro, L. Bencivenni, R. Teghil, and R. Mastromarino, "Vapour pressures and sublimation enthalpies of thymine and cytosine," *Thermochimica Acta*, vol. 42, no. 1, pp. 75–83, 1980.

[27] S.-C. Yam, S. M. Zain, V. S. Lee, and K.-H. Chew, "Correlation between polar surface area and bioferroelectricity in dna and rna nucleobases," *The European Physical Journal E*, vol. 41, no. 7, p. 86, 2018.

[28] J. Machacek, F. Blanco, G. Garcia, S. Buckman, and J. Sullivan, "Regularities in positronium formation for atoms and molecules," *Journal of Physics B: Atomic, Molecular and Optical Physics*, vol. 49, no. 6, p. 064003, 2016.

[29] A. Sieradzka, F. Blanco, M. C. Fuss, Z. Masin, J. Gorfinkiel, and G. García, "Electron scattering from pyridine," *The Journal of Physical Chemistry A*, vol. 118, no. 33, pp. 6657–6663, 2014.

[30] D. Stevens, T. Babij, J. Machacek, S. Buckman, M. Brunger, R. White, G. García, F. Blanco, L. Ellis-Gibbings, and J. Sullivan, "Positron scattering from pyridine," *The Journal of chemical physics*, vol. 148, no. 14, p. 144308, 2018.

[31] C. Makochekanwa, A. Bankovic, W. Tattersall, A. Jones, P. Caradonna, D. S. Slaughter, K. Nixon, M. J. Brunger, Z. Petrovic, J. P. Sullivan, *et al.*, "Total and positronium formation cross sections for positron scattering from h2o and hcooh," *New Journal of Physics*, vol. 11, no. 10, p. 103036, 2009.

[32] M. Brunger, S. Buckman, and K. Ratnavelu, "Positron scattering from molecules: An experimental cross section compilation for positron transport studies and benchmarking theory," *Journal of Physical and Chemical Reference Data*, vol. 46, no. 2, p. 023102, 2017.

[33] J. Usukura, K. Varga, and Y. Suzuki, "Signature of the existence of the positronium molecule," *Physical Review A*, vol. 58, no. 3, p. 1918, 1998.

[34] J. Danielson, J. Gosselin, and C. Surko, "Dipole enhancement of positron binding to molecules," *Physical review letters*, vol. 104, no. 23, p. 233201, 2010.

[35] H. Khesbak, O. Savchuk, S. Tsushima, and K. Fahmy, "The role of water h-bond imbalances in b-dna substate transitions and peptide recognition revealed by time-resolved ftir spectroscopy," *Journal of the American Chemical Society*, vol. 133, no. 15, pp. 5834–5842, 2011.

[36] R. White, W. Tattersall, G. Boyle, R. E. Robson, S. Dujko, Z. L. Petrovic, A. Bankovic, M. J. Brunger, J. Sullivan, S. Buckman, *et al.*, "Low-energy electron and positron transport in gases and soft-condensed systems of biological relevance," *Applied Radiation and Isotopes*, vol. 83, pp. 77–85, 2014.

[37] R. Zhang, A. Faure, and J. Tennyson, "Electron and positron collisions with polar molecules: studies with the benchmark water molecule," *Physica Scripta*, vol. 80, no. 1, p. 015301, 2009.

[38] F. Blanco, A. Roldán, K. Krupa, R. McEachran, R. White, S. Marjanović, Z. L. Petrović, M. J. Brunger, J. Machacek, S. J. Buckman, *et al.*, "Scattering data for modelling positron tracks in gaseous and liquid water," *Journal of Physics B: Atomic, Molecular and Optical Physics*, vol. 49, no. 14, p. 145001, 2016.

[39] K. Kotera, T. Saito, and T. Yamanaka, "Measurement of positron lifetime to probe the mixed molecular states of liquid water," *Physics Letters A*, vol. 345, no. 1-3, pp. 184–190, 2005.

[40] J. D. Gorfinkiel and S. Ptasinska, "Electron scattering from molecules and molecular aggregates of biological relevance," *Journal of Physics B: Atomic, Molecular and Optical Physics*, vol. 50, no. 18, p. 182001, 2017.

[41] R. White. Private Communication, 2016.

[42] R. Finn, "Capillary surface interfaces," *Notices AMS*, vol. 46, no. 7, pp. 770–781, 1999.

[43] G. Barozzi and D. Angeli, "A note on capillary rise in tubes," *Energy Procedia*, vol. 45, pp. 548–557, 2014.

[44] M. Tanaka, G. Girard, R. Davis, A. Peuto, and N. Bignell, "Recommended table for the density of water between 0 c and 40 c based on recent experimental reports," *Metrologia*, vol. 38, no. 4, p. 301, 2001.

[45] A. W. Adamson, A. P. Gast, *et al.*, *Physical chemistry of surfaces*, vol. 15. Interscience New York, 1967.

[46] K. Birdi, D. Vu, and A. Winter, "A study of the evaporation rates of small water drops placed on a solid surface," *The Journal of physical chemistry*, vol. 93, no. 9, pp. 3702–3703, 1989.

[47] W. W. Moses, "Fundamental limits of spatial resolution in pet," *Nuclear Instruments and Methods in Physics Research Section A: Accelerators, Spectrometers, Detectors and Associated Equipment*, vol. 648, pp. S236–S240, 2011.

[48] E. P. Visser, J. A. Disselhorst, M. Brom, P. Laverman, M. Gotthardt, W. J. Oyen, and O. C. Boerman, "Spatial resolution and sensitivity of the inveon small-animal pet scanner," *Journal of Nuclear Medicine*, vol. 50, no. 1, pp. 139–147, 2009.

[49] C. S. Levin and E. J. Hoffman, "Calculation of positron range and its effect on the fundamental limit of positron emission tomography system spatial resolution," *Physics in medicine and biology*, vol. 44, no. 3, p. 781, 1999.

[50] S. R. Cherry, J. A. Sorenson, and M. E. Phelps, *Physics in nuclear medicine*. Elsevier Health Sciences, 2012.

[51] S. Surti, A. Kuhn, M. E. Werner, A. E. Perkins, J. Kolthammer, and J. S. Karp, "Performance of philips gemini tf pet/ct scanner with special consideration for its time-of-flight imaging capabilities," *Journal of Nuclear Medicine*, vol. 48, no. 3, pp. 471–480, 2007.

[52] C. S. Levin and E. J. Hoffman, "Calculation of positron range and its effect on the fundamental limit of positron emission tomography system spatial resolution," *Physics in Medicine and Biology*, vol. 45, no. 2, p. 559, 2000.

[53] A. Wirrwar, H. Vosberg, H. Herzog, H. Halling, S. Weber, and H.-W. Muller-Gartner, "4.5 tesla magnetic field reduces range of high-energy positrons-potential implications for positron emission tomography," *IEEE Transactions on Nuclear Science*, vol. 44, no. 2, pp. 184–189, 1997.

[54] W. Brandt and R. Paulin, "Positron implantation-profile effects in solids," *Physical review B*, vol. 15, no. 5, p. 2511, 1977.

[55] S. E. Derenzo, "Precision measurement of annihilation point spread distributions for medically important positron emitters," tech. rep., California Univ., Berkeley (USA). Lawrence Berkeley Lab., 1979.

[56] P. Hasgall, F. Di Gennaro, C. Baumgartner, E. Neufeld, B. Lloyd, M. Gosselin, D. Payne, A. Klingenbck, and N. Kuster, "Itis database for thermal and electromagnetic parameters of biological tissues," Version 4.0, May 15, 2018.

[57] K. D. Sattler, *Handbook of nanophysics: nanoelectronics and nanophotonics*. CRC Press, 2010.

[58] X. Wang, L. Yang, D. M. Shin, *et al.*, "Application of nanotechnology in cancer therapy and imaging," *CA: a cancer journal for clinicians*, vol. 58, no. 2, pp. 97–110, 2008.

[59] J. Zhou, J. Ralston, R. Sedev, and D. A. Beattie, "Functionalized gold nanoparticles: synthesis, structure and colloid stability," *Journal of Colloid and Interface Science*, vol. 331, no. 2, pp. 251–262, 2009.

[60] M. Colombo, S. Carregal-Romero, M. F. Casula, L. Gutierrez, M. P. Morales, I. B. Boehm, J. T. Heverhagen, D. Prosperi, and W. J. Parak, "Biological applications of magnetic nanoparticles," *Chemical Society Reviews*, vol. 41, no. 11, pp. 4306–4334, 2012.

[61] P. Ghosh, G. Han, M. De, C. K. Kim, and V. M. Rotello, "Gold nanoparticles in delivery applications," *Advanced drug delivery reviews*, vol. 60, no. 11, pp. 1307–1315, 2008.

[62] N. Stubičar, M. Ćavar, and D. Škrtić, "Crystal growth of lead fluoride using constant composition method i. the effect of pb/f activity ratio on the solubility of solid phase," in *Dispersed Systems*, pp. 201–206, Springer, 1988.

[63] N. Stubičar, M. Ščrbak, and M. Stubičar, "Crystal growth of lead fluoride using the constant composition method ii. the effect of pb/f activity ratio on the kinetics of crystal growth," *Journal of crystal growth*, vol. 100, no. 1, pp. 261–267, 1990.

[64] N. Stubičar, B. Marković, A. Tonejc, and M. Stubičar, "Crystal growth of lead fluoride phases using the constant composition method iii. effect of ph and ionic strength," *Journal of crystal growth*, vol. 130, no. 1-2, pp. 300–304, 1993.

[65] A. E. Nel, L. Mädler, D. Velegol, T. Xia, E. M. Hoek, P. Somasundaran, F. Klaessig, V. Castranova, and M. Thompson, "Understanding biophysicochemical interactions at the nano–bio interface," *Nature materials*, vol. 8, no. 7, pp. 543–557, 2009.

[66] D. M. Keogan and D. M. Griffith, "Current and potential applications of bismuth-based drugs," *Molecules*, vol. 19, no. 9, pp. 15258–15297, 2014.